STEMedicine

Vol 1 • Issue 1 • Jan 2020

ISSN 2705-1188

Inaugural Issue

• Bridging Scientists and Physicians

STEMedicine

stemedicine.org

Bridging Scientists and Physicians

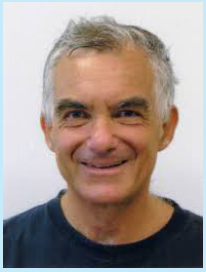

Vincent TORRE

Full Professor in Physiology
Neurobiology and Cognitive Neuroscience Sectors
International School for Advanced Studies (SISSA)
Via Bonomea, Trieste, Italy

We are proud and honoured to launch the inaugural issue of STEMedicine, an international, peer-reviewed, open access journal published on a quarterly basis.

Advances in medicine have always relied on the bi-directional communication system between scientists and physicians. Physicians give scientists their first-hand observations of diseases, and scientists discover the cause of diseases and means for physicians to treat them, then physicians provide scientists with further feedback on patient response to the treatment. Such efficient and constructive communication forges a link that has long served the best interests of patients. With the aim to strengthen this significant link between scientists and physicians, we established STEMedicine as an online platform to share scientific discoveries and technological advances both in biology and medicine.

STEMedicine welcomes both research articles describing original and novel results on basic and clinical investigations, and review articles summarizing most recent developments in science and medicine. With the vision to benefit both the scientific and medical communities, as well as to share knowledge to everyone, all published articles in STEMedicine will be freely accessible and open access online via STEMedicine.org. Under the Creative Commons Attribution License adopted by STEMedicine, authors retain their copyright to articles published in STEMedicine, and all readers are able to download, print, distribute and present the articles at no cost and without any subscription.

It is also my honour to work with an excellent group of scientists of a broad spectrum of biomedical disciplines from Europe, the US, China and Singapore, who will serve as members of the Editorial Team. Under my lead, the Editorial Team is tasked with a high standard of scientific ethics and quality, professional integrity and responsibility, as well as a compassion for patients suffering from diseases, to fulfil the vision of STEMedicine.

Sincerely,

Editor-in-Chief
Vincent Torre

https://doi.org/10.37175/stemedicine.v1i1.29

REVIEW ARTICLE

Spinal cord neural stem cells heterogeneity in postnatal development

Jelena BAN* and Miranda MLADINIC

Laboratory for Molecular Neurobiology, Department of Biotechnology, University of Rijeka, Radmile Matejčić 2, 51000 Rijeka, Croatia

*Correspondence: jelena.ban@biotech.uniri.hr
https://doi.org/10.37175/stemedicine.v1i1.19

ABSTRACT

Neural stem cells are capable of generating new neurons during development as well as in the adulthood and represent one of the most promising tools to replace lost or damaged neurons after injury or neurodegenerative disease. Unlike the brain, neurogenesis in the adult spinal cord is poorly explored and the comprehensive characterization of the cells that constitute stem cell neurogenic niche is still missing. Moreover, the terminology used to specify developmental and/or anatomical central nervous system regions, where neurogenesis in the spinal cord occurs, is not consensual and the analogy with the brain is often unclear. In this review, we will try to describe the heterogeneity of the stem cell types in the spinal cord ependymal zone, based on their origin and stem cell potential. We will also consider specific animal *in vitro* models that could be useful to identify the "right" stem cell candidate for cell replacement therapies.

Keywords: Neural stem cells · Radial glia · Ependymal cells · Development · Spinal cord injury

Introduction

Spinal cord injury (SCI) of traumatic or non-traumatic origin is a devastating neurological condition, with severe motor disfunction and other deficits. Recent advances in SCI research have enabled development of different therapeutic strategies trying to counteract the detrimental consequences of the processes involved in secondary injury, or trying to replace damaged or lost neurons at the place of injury, using cell transplantation therapies as reviewed recently in (1-3). However, the clinical translation of the therapeutic strategies with substantial benefits for patients has thus far been elusive, setting the necessity for better understanding of both molecular and cellular mechanisms involved in the pathophysiology of the SCI and stem cell biology.

Neural stem cells (NSC) are promising source of donor cells that could be used in cell transplantation strategies to overcome the incapacity of the central nervous system (CNS) to repair and regenerate after injury. Because of their limited accessibility and ethical concerns regarding the use of human embryonic stem cells (ESC), induced pluripotent stem cells (iPSCs), from which patient-specific NSC could be produced, offer the exceptional opportunity for development of personalized cell replacement therapies (4-7). Generation of the human iPSCs was first reported in 2007, only one year after the remarkable discovery that murine fibroblasts can be reprogrammed into pluripotent cell state (8,9). Since then, research in the field had enormous growth and iPSCs have also been widely considered for the treatment of the SCI (3,10), with the first-in-human clinical study to launch for subacute SCI (11).

However, several concerns have arisen regarding their clinical use, related to the reprogramming method (alternatives to viral vectors are necessary) and the low efficiency for both reprogramming rate and differentiation yield. Probably, the most important issue is the fact that the reprograming procedure, with high number of passages *in vitro* required to reach pluripotent cell state, carries high risk of generation of new mutations. This can lead to tumorigenesis in addition to retainment of patient-specific mutations (6,12). Chemical reprogramming with small molecules, mostly epigenetic modulators, succeeded to produce iPSCs in mice (13), as well as chemically induced NSC (14) and neurons (15,16). Transdifferentiation, i.e. direct conversion of somatic cells into another differentiated CNS cell lineage occurs without induction of pluripotency by gene delivery and is therefore considered safer for clinical application than

human iPSCs.

Valid alternative to the cell transplantation strategies is the use of endogenous spinal cord stem cells to replace the lost or damaged neurons *in loco* (without need of transplantation). The endogenous spinal cord stem cells are tissue-specific stem cells, already committed to neural phenotype. Therefore, there would be no need for them to reach the pluripotent state. The ideal solution would be to instruct those cells to produce new neurons that will integrate into existing networks, by controlling their differentiation mechanisms.

The premise for the use of endogenous stem cells is their complete characterization and deep knowledge of the reprogramming mechanisms. The characterization of spinal cord stem cell niche(s) is still incomplete in terms of cell types, for most of which the exclusive markers are missing, and in terms of their differentiation potential and their localization. Moreover, to favor neuroregeneration after SCI or neurodegenerative diseases, it is necessary to unblock the inhibitory components in the extracellular space and possibly, to also "reprogram" glial cells to favor the regeneration-permissive anti-inflammatory phenotype (17-20).

Here we will describe what is known about the cellular composition of the spinal region around the central canal, which is considered stem cell niche that persists in adulthood. This region is composed of heterogeneous cell populations, some of which are still not fully identified (21). This heterogeneity arises very early in the development and therefore it is crucial to track and unveil the developmental origin of each of those different cell subtypes, in order to exploit them for therapeutic purposes.

Overlapping stem cell terminology

There are many terms used to describe a variety of cells that appear during highly dynamic developmental processes of cell proliferation and differentiation. Specific terms are assigned to particular developmental stage of a particular CNS region and in a particular animal species. Neurogenesis during development and adulthood is best characterized in the cortex. Although this knowledge could be applicable to other CNS regions (22), including spinal cord, the differences and the analogy are not completely clear and there are still ongoing debates.

NSC is the generic and most frequent term to describe multipotent stem cells that can generate all four CNS lineages with ectodermal origin: neurons, astrocytes, oligodendrocytes and ependymal cells (22-24). The term "neural" denotes the loss of pluripotency, characteristic of ESC or iPSCs only. NSC are found in both developing and adult nervous system. By definition, NSC are precursors of neurons and glia and therefore should be identical to neural progenitor (or precursor) cells (NPCs) (22). However, some researchers distinguish NPCs as cells with limited self-renewing capacity, contrary to NSC, considered to have prolonged self-renewal and broader differentiation potential (21,25). The combined term stem/progenitor cell (SPC) has also been used (26-28).

Moreover, very often there is a "transitory" stem cell state: for example, NSC or NPC can give rise to distinct subpopulation of neuron and glial precursor cells, respectively. These transit amplifying cells (22) or intermediate progenitor cells (IPC) are considered to be multipotent stem cells, able to generate neurons (nIPC), astrocytes (aIPC) and oligodendrocytes (oIPC) (22) or bipotent (29) as well as unipotent stem cells, expressing transcription factor Tbr2, capable of generating neurons only (30-32). IPC in developing cortex are also called basal progenitors (25) indicating their anatomical position. In addition to these two currently interchangeable terms, several other adjectives such as subependymal or extraventricular, abventricular, non-surface, subventricular, etc. (33) were used to describe these mitotic NPCs.

The term "basal progenitor" unavoidably leads to radial glia (RG), "universal" precursors of all CNS cell types of the neuroectodermal lineage. RG are therefore both NSC and NPC (22,33). They develop from neuroepithelial cells (NEC) or neuroepithelial progenitors (25) early in embryonic development, at the onset of neurogenesis (E9/E10 in mouse) (22,25) and generate mitotic NPC or IPC by asymmetric division. RG morphology is typically bipolar: one long process that projects radially and reaches pial (outer) surface while the shorter one faces the lumen of the ventricle; cell body is confined to the apical region that will become the ventricular zone (VZ) (25). For a long time they were seen solely as scaffolds, i.e. structural support for neuronal migration, while now their neuro- and gliogenic potential is widely accepted (34-36).

Some researchers consider them to be present only during embryonic development and absent in the mature brain (37), while others identify them as adult NSC (23,35,38) or similarly, consider that the adult NSC are "RG-like" (33,38). Although RG are historically described as fetal glia (33), indicating their glial nature, and because of the presence of the glial fibrillary acidic protein (GFAP), astrocyte-specific glutamate transporter (GLAST), glutamine synthetase, S100β or vimentin expression (21,34,39), they are sometimes classified as astrocytes' subtype (37). RG are heterogeneous cell population consisting of bipolar apical progenitors, confined to the VZ, and basal RG that migrate away from VZ, also named translocating, transitional, transforming or intermediate RG (33). Late neurogenesis is followed by gliogenesis around E17.5 in mouse (25) which continues postnatally. During gliogenesis, bipolar RG progressively become uni- and multipolar, assuming astrocytes' morphology (22).

In summary, the present NSC terminology reflects the intrinsic complexity and heterogeneity of developing CNS cells. There is however a need for consensus and clear, unified terminology (33).

Recently, single cell biology, with single cell transcriptomics in particular, is emerging as a revolutionary field that questions our traditional views on distinguishing between cell type and cell state (29). In the proposed model, called 'periodic table of cell types', where cell types are defined according to their transcription factors' expression profile, the sequence of events, i.e. cells that appear during CNS

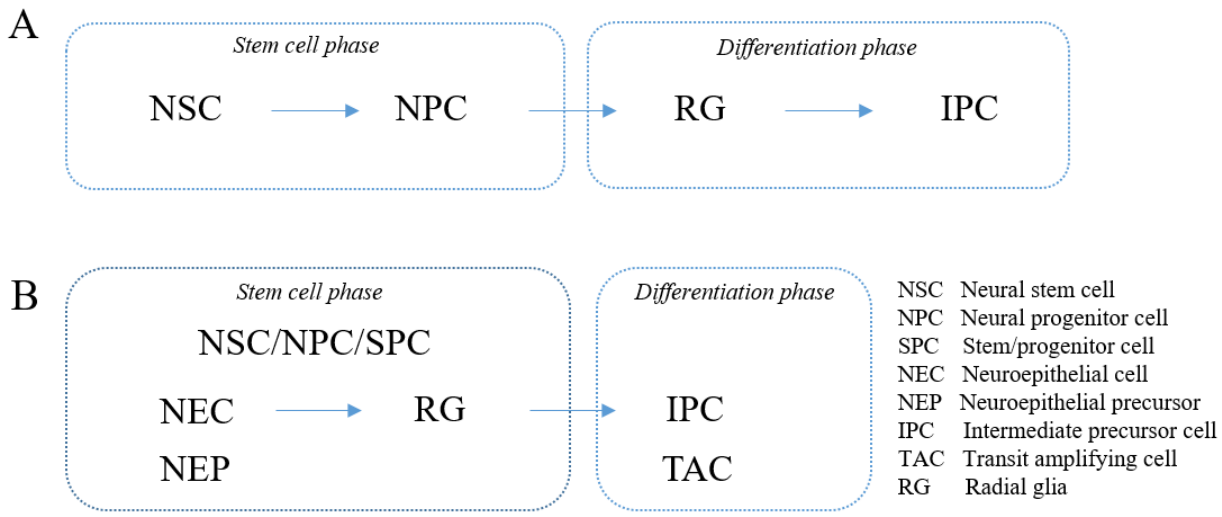

Figure 1. Terminology used to describe cells that appear during CNS development. (A) Recently proposed method in which a periodic table of cell types is proposed with stem cell and differentiation phase (29). (B) Additional terms collected from the literature. NSC, Neural stem cell; NPC, Neural progenitor cell; SPC, stem/progenitor cell; NEC, Neuroepithelial cell; NEP, Neuroepithelial precursor; RG, Radial glia; IPC, Intermediate precursor cell; TAC, Transit amplifying cell.

development, is: NSC, NPC, RG, IPC, ending with differentiated cells (neurons, astrocytes, oligodendrocytes and EC) (29), as summarized in **Figure 1A**. NSC and NPC both belong to "stem cell phase" while RG and IPC are considered to be in "differentiation phase", according to this model. In **Figure 1B**, the most frequently used (and overlapping) terms are shown and a more inclusive version is proposed.

Most of our knowledge about developing and adult NSC niches comes from studies in the cerebral cortex, and in the next section we will try to apply this knowledge to the spinal cord.

Spinal cord central canal stem cell niche

In the spinal cord, unlike the cortex, NSC are less well understood. The pool of stem cells is considered to be mainly confined to the region surrounding the central canal, with EC representing a main cell type. Stem cells are also found dispersed in the spinal cord tissue outside the ependymal region, with more restricted proliferative potential (21).

The ependymal region is composed of different cells facing the lumen as well as cells in subependymal position, reminiscent of pseudostratified epithelium. The important difference, when compared to the brain, is the absence in the spinal cord of the distinct subependymal layer such as subventricular zone (SVZ) (21,26). Moreover, *in vivo* neurogenesis in the adult spinal cord has not been reported yet. For a long time, the region surrounding the spinal central canal was thought to be composed of a single layer of densely packed ciliated and cuboidal, epithelial-like secretory cells (21,23,40), while today it becomes clear that these cells are not homogeneous at all: in addition to EC, still uncharacterized cells with unknown function exist (21).

EC, together with astrocytes, oligodendrocytes and microglia, are one of the four main types of (neuro) glia (41), although sometimes are included into astroglia (37). EC are cells of neuroectodermal origin, deriving from proliferating NEC around the central lumen of the caudal neural tube, from which the central canal and spinal cord develops. At the onset of neurogenesis, NEC will give rise to RG (22,40), and at that stage NEC are already heterogeneous cell population in terms of stemness and differentiation potential (21). In the brain, RG give rise to EC between E14-E16 in mouse, while in the spinal cord they seem to appear later, earliest at E15.5 (and around E18 in rats) (40,42,43). Even though EC are generated during embryonic age, their differentiation and maturation, characterized for example by the formation of cilia, occur only after birth, in the first postnatal week (32). Proliferation of ependymocytes continues for several weeks after birth, necessary for the extension of the growing spinal cord. At 9 weeks after birth in mouse and 12-13 weeks in rats, the spinal cord stops elongating, cell proliferation stops and EC enters a quiescent state (21,28,40). Adult ependymocytes in the spinal cord face the lumen of central canal and, as those of the brain ventricles, produce cerebrospinal fluid (CSF) and regulate its composition and movement.

The adult ependymal region is composed of lateral and polar domains. In addition to the cuboidal ependymocytes, distributed laterally, another cell type is present: tanycytes, also referred to as radial ependymocytes or radial ependymal cells (21). Their cell body is situated in ependymal or subependymal region, the apical process is in contact with CSF and the long basal process with blood vessels. Their main functions are uptake and transport of substances (regulation of CSF composition) as well as regulation of vasodilatation of spinal cord vessels, as indicated by the expression of vasoactive intestinal

polypeptide (VIP) (21).

Tanycytes are also found in polar domains of the central canal where high number of cells present radial morphology and express GFAP. This third cell type is known as radial dorsal cells or dorsal tanycytes or ependymoglial cells (21,44). In common with all EC of the central canal, they express nestin and VIP, while with ependymocytes share SOX2 and vimentin expression. Subpopulation of these cells show additional expression of NSC markers such as BLBP and CD15 (21). Moreover, expression of transcription factor ZEB1, a mesenchymal cell marker, was reported (28).

GFAP+ cells, with shorter basal process and in smaller number, are also found in the ventral part of the central canal and occasionally in lateral part, with cell bodies placed in subependymal region (21). In addition to different EC, there are also sporadically distributed neurons that send projection in the central canal having their soma situated in ependymal or subependymal region, called CSF contacting neurons and finally, some still unidentified cells are observed (21,40).

As can be noted, ependymal region of the spinal cord is composed of a variety of cells with distinct morphologies and with significant overlap in expression profiles between different cell types, which represent a challenge in proper classification. For instance, tanycytes are considered to be a subtype of ependymal cells in the mouse spinal cord (21,44), but evidences showing differences in the expression profile of the better-characterized brain counterparts have emerged (40,44,45). Moreover, their similarity with RG (both share radial morphology and express common markers that persist in the adult spinal cord) makes the distinction between different ependymal cell types less clear.

Are EC/ependymocytes stem cells?

The presence of NSC markers such as SOX2, CD15, CD133, nestin, vimentin, BLBP, GFAP and others (21,40,45) in the adult ependymal region opens another controversial issue: are EC adult NSC of the spinal cord? Do RG (or RG-like cells) persist in the adult spinal cord? Why adult neurogenesis in the spinal cord is more limited than brain neurogenesis?

The central canal is considered spinal cord stem cell niche but the degree of "stemness" of ependymocytes is still discussed. In the brain, the most accepted view is that the only *in vivo* proliferating NSC/NPC capable of neurogenesis are B1 cells, RG-like subpopulation of astrocytes in the SVZ (25,32,33,43,46). Therefore, EC of the brain are not considered to be NSC but rather unipotent cells (46).

After injury, ependymal cells become activated, proliferate, migrate and differentiate into astrocytes and oligodendrocytes, contributing to scar formation (21,26-28,44,47).

In the spinal cord, both ependymal (47) and GFAP-positive RG-like dorsal cells (21,48) were investigated as putative stem cells despite the reports in which adult rodent spinal cord EC were defined as postmitotic cells (42).

In addition to the expression of NSC markers observed *in vivo*, *in vitro* experiments indicated different differentiation as well as proliferative potential of EC. *In vitro* stemness is evaluated with a "neurosphere assay": NSC of particular brain or spinal cord region are dissected, dissociated and cultured usually in suspension, in the presence of basic fibroblast growth factor and epidermal growth factor. After several days in culture, free-floating (neuro)spheres are formed and can be further dissociated and replated in either proliferative condition (generating secondary neurospheres) or induced to differentiate, offering the way to asses their *in vitro* differentiation potential. This assay was first developed in early 1990s (49) and also became one of the most frequently used. Despite its notable utility, it should be kept in mind that the *in vitro* differentiation potential could differ from the *in vivo* one, since the extracellular environment strongly influences cell behavior. Moreover, not all NSC are efficiently amplified *in vitro* (quiescent NSC or the specific NSC/NPC subpopulations present in very low number could not generate neurospheres) and not all neurospheres are derived from NSC [for a review see (50)].

This assay has also provided one of the first evidences that cells in adult spinal cord generate multipotent neurospheres (47,51) with both neurogenic and gliogenic potential, and this NSC property was explicitly assigned to EC (47). However, at that time, the ependymal layer was thought to be composed of homogeneous cell population, and in the same year (1999) another study showed that neurosphere-forming cells in SVZ were not EC, but astrocytes (also known as B1 cells), and that EC did not divide *in vivo* (52). Moreover, brain ciliated EC were defined as unipotent cells capable of forming neurospheres, but with gliogenic instead of neurogenic potential (46).

The critical role of extracellular environment was further demonstrated when spinal cord-derived dissociated neurospheres transplanted in the hippocampus generated neurons, while those transplanted in the spinal cord became only glial cells (53).

The explanation of the contrasting results obtained in the last two decades is still missing and further investigations are necessary to understand the stem cell potential of the ependymal region of the spinal cord.

Opossum model to study ependymal spinal cord SPC

In contrast to invertebrates and lower vertebrates, mammals have extremely reduced ability to regenerate spinal cord after injury. One of the exceptions are marsupials, such as opossums, that are born very immature, in an embryonic-like state (PO correspond roughly to E14-15 mouse or rat embryos), and they retain the ability to completely regenerate spinal cord after injury in the first two postnatal weeks (54,55). It would be important to understand how the activation, proliferation and migration of EC after injury correlate with their neurogenic potential and postnatal spinal cord regeneration,possible in opossums and impossible in placental mammals. Recently,

the transcription factor ATF3 was detected as a potential candidate to regulate SPC quiescence/activation in the spinal EC of rats as well as of the opossum *Monodelphis domestica* (27).

Together with currently available knowledge on placental mammals, comparative studies on regenerative species could provide important indications about the exact cell types responsible for the functional regeneration of the CNS tissue, and those results could contribute to provide a missing solution for the effective therapeutic strategy for CNS injuries and neuroregeneration.

Conclusion

Unlike in the brain, adult neurogenesis in the spinal cord is still under investigation, with unclear characterization of spinal SPC. Further efforts should be made to identify the "best" source of endogenous stem cells that could hopefully allow us to develop effective neuroregenerative strategies for SCI and neurodegenerative diseases.

Acknowledgements

The experimental work has been conducted on equipment financed by the European Regional Development Fund (ERDF) within the project "Research Infrastructure for Campus-based Laboratories at University of Rijeka" (RC.2.2.06-0001), the Croatian Science Foundation (CSF) grant IP-2016-06-7060 and the financial support from the University of Rijeka (18.12.2.1.01, 18-258-6427 and 18-290-1463).

Conflict of interest

The authors declare no conflict of interest.

Funding body

The experimental work has been conducted on equipment financed by the European Regional Development Fund (ERDF) within the project "Research Infrastructure for Campus-based Laboratories at University of Rijeka" (RC.2.2.06-0001), the Croatian Science Foundation (CSF) grant IP-2016-06-7060 and the financial support from the University of Rijeka (18.12.2.1.01, 18-258-6427 and 18-290-1463).

References

1. Badhiwala JH, Ahuja CS, Fehlings MG. Time is spine: a review of translational advances in spinal cord injury. J Neurosurg Spine. 2018 20;30(1):1–18.
2. Courtine G, Sofroniew MV. Spinal cord repair: advances in biology and technology. Nat Med. 2019;25(6):898–908.
3. Trawczynski M, Liu G, David BT, Fessler RG. Restoring motor neurons in spinal cord injury with induced pluripotent stem cells. Front Cell Neurosci. 2019;13:369.
4. Ban J, Mladinić Pejatović M. Nanotechnology approaches for autologous stem cell manipulation in personalized regenerative medicine. In: Bodiroga-Vukobrat N, Rukavina D, Pavelić K, Sander GG, editors. Personalized Medicine in Healthcare Systems. Europeanization and Globalization, vol 5. Springer, Cham.
5. Casarosa S, Bozzi Y, Conti L. Neural stem cells: ready for therapeutic applications? Mol Cell Ther. 2014 Oct 15;2.
6. Stadtfeld M, Hochedlinger K. Induced pluripotency: history, mechanisms, and applications. Genes Dev. 2010 Oct 15;24(20):2239–63.
7. Hanna JH, Saha K, Jaenisch R. Somatic cell reprogramming and transitions between pluripotent states: facts, hypotheses, unresolved issues. Cell. 2010 Nov 12;143(4):508–25.
8. Takahashi K, Yamanaka S. Induction of pluripotent stem cells from mouse embryonic and adult fibroblast cultures by defined factors. Cell. 2006 Aug 25;126(4):663–76.
9. Takahashi K, Tanabe K, Ohnuki M, Narita M, Ichisaka T, Tomoda K, et al. Induction of pluripotent stem cells from adult human fibroblasts by defined factors. Cell. 2007 Nov 30;131(5):861–72.
10. Nagoshi N, Tsuji O, Nakamura M, Okano H. Cell therapy for spinal cord injury using induced pluripotent stem cells. Regen Ther. 2019 Dec;11:75–80.
11. Tsuji O, Sugai K, Yamaguchi R, Tashiro S, Nagoshi N, Kohyama J, et al. Concise Review: laying the groundwork for a first-in-human study of an induced pluripotent stem cell-based intervention for spinal cord injury. Stem Cells. 2019;37(1):6–13.
12. Yoshihara M, Hayashizaki Y, Murakawa Y. Genomic instability of iPSCs: challenges towards their clinical applications. Stem Cell Rev Rep. 2017 Feb;13(1):7–16.
13. Hou P, Li Y, Zhang X, Liu C, Guan J, Li H, et al. Pluripotent stem cells induced from mouse somatic cells by small-molecule compounds. Science. 2013 Aug 9;341(6146):651–4.
14. Zheng J, Choi K-A, Kang PJ, Hyeon S, Kwon S, Moon J-H, et al. A combination of small molecules directly reprograms mouse fibroblasts into neural stem cells. Biochem Biophys Res Commun. 2016 15;476(1):42–8.
15. Biswas D, Jiang P. Chemically Induced Reprogramming of somatic cells to pluripotent stem cells and neural cells. Int J Mol Sci. 2016 Feb 6;17(2):226.
16. Qin H, Zhao A, Fu X. Small molecules for reprogramming and transdifferentiation. Cell Mol Life Sci. 2017 Oct 1;74(19):3553–75.
17. Gaudet AD, Fonken LK. Glial cells shape pathology and repair after spinal cord injury. Neurotherapeutics. 2018;15(3):554–77.
18. Orr MB, Gensel JC. Spinal cord injury scarring and inflammation: therapies targeting glial and inflammatory responses. Neurotherapeutics. 2018;15(3):541–53.
19. Liddelow SA, Barres BA. Reactive astrocytes: production, function, and therapeutic potential. Immunity. 2017 Jun 20; 46(6):957–67.
20. Ban J, Sámano C, Mladinic M, Munitic I. Glia in amyotrophic lateral sclerosis and spinal cord injury: common therapeutic targets. Croat Med J. 2019 Apr;60(2):109–20.
21. Hugnot JP, Franzen R. The spinal cord ependymal region: a stem cell niche in the caudal central nervous system. Front Biosci (Landmark Ed). 2011 Jan 1;16:1044–59.
22. Kriegstein A, Alvarez-Buylla A. The glial nature of embryonic and adult neural stem cells. Annu Rev Neurosci. 2009;32(1):149–84.
23. Schwartz JH, Siegelbaum SA, Hudspeth AJ. Principles of neural science, Fifth Edition. McGraw Hill Professional; 2013. 1761 p.
24. Morest DK, Silver J. Precursors of neurons, neuroglia, and ependymal cells in the CNS: What are they? Where are they from? How do they get where they are going? Glia. 2003;43(1):6–18.
25. Malatesta P, Appolloni I, Calzolari F. Radial glia and neural stem cells. Cell Tissue Res. 2008 Jan;331(1):165–78.
26. McDonough A, Martínez-Cerdeño V. Endogenous proliferation after spinal cord injury in animal models. Stem Cells Int. 2012;2012:387513.
27. Mladinic M, Bianchetti E, Dekanic A, Mazzone GL, Nistri A. ATF3 is a novel nuclear marker for migrating ependymal stem cells in the rat spinal cord. Stem Cell Res. 2014 May;12(3):815–27.
28. Sabourin J-C, Ackema KB, Ohayon D, Guichet P-O, Perrin FE,Garces A, et al. A mesenchymal-like ZEB1(+) nicheharbors dorsal radial glial fibrillary acidic protein-positive stem cells in the spinal cord. Stem Cells. 2009 Nov;27(11):2722–33.

29. Xia B, Yanai I. A periodic table of cell types. Development. 2019 Jun 27;146(12).
30. Paridaen JTML, Huttner WB. Neurogenesis during development of the vertebrate central nervous system. EMBO Rep. 2014 Apr;15(4):351–64.
31. Englund C, Fink A, Lau C, Pham D, Daza RAM, Bulfone A, et al. Pax6, Tbr2, and Tbr1 are expressed sequentially by radial glia, intermediate progenitor cells, and postmitotic neurons in developing neocortex. J Neurosci. 2005 Jan 5;25(1):247–51.
32. Rushing G, Ihrie RA. Neural stem cell heterogeneity through time and space in the ventricular-subventricular zone. Front Biol. 2016 Aug 1;11(4):261–84.
33. Martínez-Cerdeño V, Noctor SC. Neural progenitor cell terminology. Front Neuroanat. 2018 Dec 6;12.
34. Malatesta P, Götz M. Radial glia - from boring cables to stem cell stars. Development. 2013 Feb 1;140(3):483–6.
35. Merkle FT, Tramontin AD, García-Verdugo JM, Alvarez-Buylla A. Radial glia give rise to adult neural stem cells in the subventricular zone. Proc Natl Acad Sci USA. 2004 Dec 14;101(50):17528–32.
36. Noctor SC, Flint AC, Weissman TA, Dammerman RS, Kriegstein AR. Neurons derived from radial glial cells establish radial units in neocortex. Nature. 2001 Feb 8;409(6821):714–20.
37. Verkhratsky A, Parpura V. Introduction to neuroglia. Colloquium Series on Neuroglia in Biology and Medicine: From Physiology to Disease. 2014 Feb 24;1(1):1–74.
38. Gubert F, Zaverucha-do-Valle C, Pimentel-Coelho PM, Mendez-Otero R, Santiago MF. Radial glia-like cells persist in the adult rat brain. Brain Res. 2009 Mar 3;1258:43–52.
39. Levitt P, Rakic P. Immunoperoxidase localization of glial fibrillary acidic protein in radial glial cells and astrocytes of the developing rhesus monkey brain. J Comp Neurol. 1980 Oct 1;193(3):815–40.
40. Marichal N, Reali C, Trujillo-Cenóz O, Russo RE. Spinal cord stem cells in their microenvironment: the ependyma as a stem cell niche. Adv Exp Med Biol. 2017;1041:55–79.
41. Verkhratsky A, Butt A. Introduction to glia. In: Glial Neurobiology. John Wiley & Sons, Ltd; 2007. p. 1–12.
42. Spassky N, Merkle FT, Flames N, Tramontin AD, García-Verdugo JM, Alvarez-Buylla A. Adult ependymal cells are postmitotic and are derived from radial glial cells during embryogenesis. J Neurosci. 2005 Jan 5;25(1):10–8.
43. Sevc J, Daxnerová Z, Haňová V, Koval' J. Novel observations on the origin of ependymal cells in the ventricular zone of the rat spinal cord. Acta Histochem. 2011 Feb;113(2):156–62.
44. Meletis K, Barnabé-Heider F, Carlén M, Evergren E, Tomilin N, Shupliakov O, et al. Spinal cord injury reveals multilineage differentiation of ependymal cells. PLoS Biol. 2008 Jul 22;6(7):e182.
45. Goodman T, Hajihosseini MK. Hypothalamic tanycytes-masters and servants of metabolic, neuroendocrine, and neurogenic functions. Front Neurosci. 2015;9:387.
46. Laywell ED, Rakic P, Kukekov VG, Holland EC, Steindler DA. Identification of a multipotent astrocytic stem cell in the immature and adult mouse brain. Proc Natl Acad Sci USA. 2000 Dec 5;97(25):13883–8.
47. Johansson CB, Momma S, Clarke DL, Risling M, Lendahl U, Frisén J. Identification of a neural stem cell in the adult mammalian central nervous system. Cell. 1999 Jan 8; 96(1):25–34.
48. Fiorelli R, Cebrian-Silla A, Garcia-Verdugo J-M, Raineteau O. The adult spinal cord harbors a population of GFAP-positive progenitors with limited self-renewal potential. Glia. 2013;61(12):2100–13.
49. Reynolds BA, Weiss S. Generation of neurons and astrocytes from isolated cells of the adult mammalian central nervous system. Science. 1992 Mar 27;255(5052):1707–10.
50. Pastrana E, Silva-Vargas V, Doetsch F. Eyes wide open: a critical review of sphere-formation as an assay for stem cells. Cell Stem Cell. 2011 May 6;8(5):486–98.
51. Weiss S, Dunne C, Hewson J, Wohl C, Wheatley M, Peterson AC, et al. Multipotent CNS stem cells are present in the adult mammalian spinal cord and ventricular neuroaxis. J Neurosci. 1996 Dec 1;16(23):7599–609.
52. Doetsch F, Caillé I, Lim DA, García-Verdugo JM, Alvarez-Buylla A. Subventricular zone astrocytes are neural stem cells in the adult mammalian brain. Cell. 1999 Jun 11; 97(6):703–16.
53. Shihabuddin LS, Horner PJ, Ray J, Gage FH. Adult spinal cord stem cells generate neurons after transplantation in the adult dentate gyrus. J Neurosci. 2000 Dec 1;20(23):8727–35.
54. Mladinic M, Muller KJ, Nicholls JG. Central nervous system regeneration: from leech to opossum. J Physiol (Lond). 2009 Jun 15;587(Pt 12):2775–82.
55. Nicholls J, Saunders N. Regeneration of immature mammalian spinal cord after injury. Trends Neurosci. 1996 Jun;19(6):229–34.

REVIEW ARTICLE

Application of gene therapy in auditory system diseases

Chunjiang WEI[b], Weijia KONG[b*], Zuhong HE[a,b*]

[a] Department of Pathology and Laboratory Medicine, Medical University of South Carolina, Charleston, SC 29425, USA.
[b] Department of Otorhinolaryngology, Union Hospital, Tongji Medical College, Huazhong University of Science and Technology, Wuhan, China.

*Correspondence: entwjkong@hust.edu.cn; hezuhong@163.com
https://doi.org/10.37175/stemedicine.v1i1.17

ABSTRACT

Prevention and treatment of auditory related diseases through genetic intervention is a hotspot in the field of hearing research in recent years. With the development of molecular technology, gene regulation has made a major breakthrough in the research of inner ear hair cell regeneration in recent years, which may provide us with a novel and efficient way to treat auditory related diseases. This review touches on the latest research on gene therapy in hereditary deafness, drug deafness, aging-related hearing loss, and noise-related hearing loss.

Keywords: Gene therapy · Hearing · Transfection vector · Auditory diseases · Inner ear

Introduction

Hearing loss is the most common sensory deficit in humans. Approximately 466 million people worldwide suffer from deafness, and the number is expected to increase to nearly 1 billion by 2050 (http://www.who.int/mediacentre/factsheets/fs300/en/). In recent years, with the in-depth development of research on the pathogenesis of deafness, many researchers hope to improve or rescue hearing through gene therapy. We will introduce the research progress and new findings of gene therapy in hearing in this manuscript.

Construction of animal models

In order to better assess the efficiency, safety and therapeutic effects of gene transfection, it is necessary to construct a suitable animal model with a specific disease.

Mammalian model

Mice are one of the most commonly used models in mammals. At present, we have established a variety of mouse models of hearing loss induced by genes mutations to mimic some genetic mutations in human patients. However, the evolutionary relationship between mice and humans is relatively distant, and the biological differences are large. The ears of primate animals are more anatomically similar to humans, and they are more advantageous as animal models for gene therapy (1-3). Therefore, research on primate models has become a hotspot. Dai et al. evaluated whether the rhesus monkeys injected with sufficient amounts of fluid would suffer inner ear damage during the gene therapy process. The transfection conditions were optimized by comparing the transfection effects of the oval window stapedotomy pathway and the round window pathway (4). In addition, György et al. introduced the adeno-associated virus (AAV)-9 variant (aav9-php.b) into cynomolgus monkeys through round window membrane (RWM) and found that almost all of the inner and outer hair cells (HCs) were transfected. This is the first time that an AAV vector transfection assay has been performed on the inner ear of a primate (5).

Non-mammal model

Because non-mammals are genetically different from humans, they are rarely used in gene therapy research. However, the similarity between the zebrafish gene and the human gene is as high as 87%. Previous studies have found that *prps1a* and *prps1b* in the zebrafish genome are very similar to the *PRPS1* in the human genome, which provides support for zebrafish as a model for studying human hearing loss (6). In addition, the emergence of the CRISPR/CAS9 technology has made it possible to establish a model of hereditary hearing loss in zebrafish. In the latest report by Bing Zou et al., a zebrafish mariner mutant model was constructed using CRISPR/CAS9 (7).

Application of gene transfection vectors

Choosing the ideal gene transfection vector is a prerequisite for gene therapy. The ideal vector not only

has high transfection efficiency *in vivo*, but also can accurately deliver DNA into target cells or tissues. In addition, whether the transfection intensity and time of the vector are controllable, whether it is safe and convenient for large-scale preparation are also factors for evaluation. At present, vectors are mainly divided into two major categories: viral vectors and non-viral vectors.

Viral vectors

Viral vectors include adenovirus, adeno-associated virus, helper-dependent adenovirus, herpes simplex virus, vaccinia virus, etc. Viral vectors are the most widely used vectors due to their high transfection efficiency. However, the traditional viral vector still has certain toxicity, and the gene carrying capacity is small. In recent years, more ideal viral vectors have been discovered through the mutation of AAV virus, which has improved the effectiveness and safety in specific applications, such as AAV2/ANC80L65 (8, 9), AAV-ie (10), and AAV9-PHP.B (11), etc (**Figure 1**).

Non-viral vectors

Non-viral gene vectors mainly include cationic liposomes, nanomaterials, etc. Compared with viral vectors, non-viral vectors are simple to prepare, low toxicity and do not induce host immune responses. Non-viral vectors have no restriction on the capacity of carrying genes, and can be modificated to obtain a variety of biological properties. However, the transfection efficiency of non-viral vectors is relatively low.

Gene delivery pathway

At present, the gene delivery pathways commonly used in animal experiments are as follows: **(1)** perforation in the cochlea; **(2)** perforation in semicircular canals; **(3)** injection of RWM; **(4)** infiltration of RWM. The choice of path depends mainly on factors such as the subject, the type of viral vector used, the transfection efficiency of the target cell and the degree of damage to the inner ear. In addition, the electroporation technology has been used as an alternative method for gene delivery in the inner ear in recent years, but it is still limited to in vitro tissue culture and gene therapy research in the uterus (12, 13).

Gene therapy strategy

Gene therapy mainly treats diseases through gene replacement, gene silencing, gene editing and HC regeneration. Gene replacement is the most direct way of gene therapy and is mainly used in the treatment of recessive hereditary diseases with mutation-induced phenotypic loss. For hereditary diseases associated with dominant inherited mutations, gene silencing via antisense oligonucleotide and RNA interference (RNAi) are mainly used for treatment. Currently, gene editing is mainly implemented using the CRISPR/CAS9 technology. It is the most advanced programmable nuclease for genome engineering and repair of targeted gene mutations.

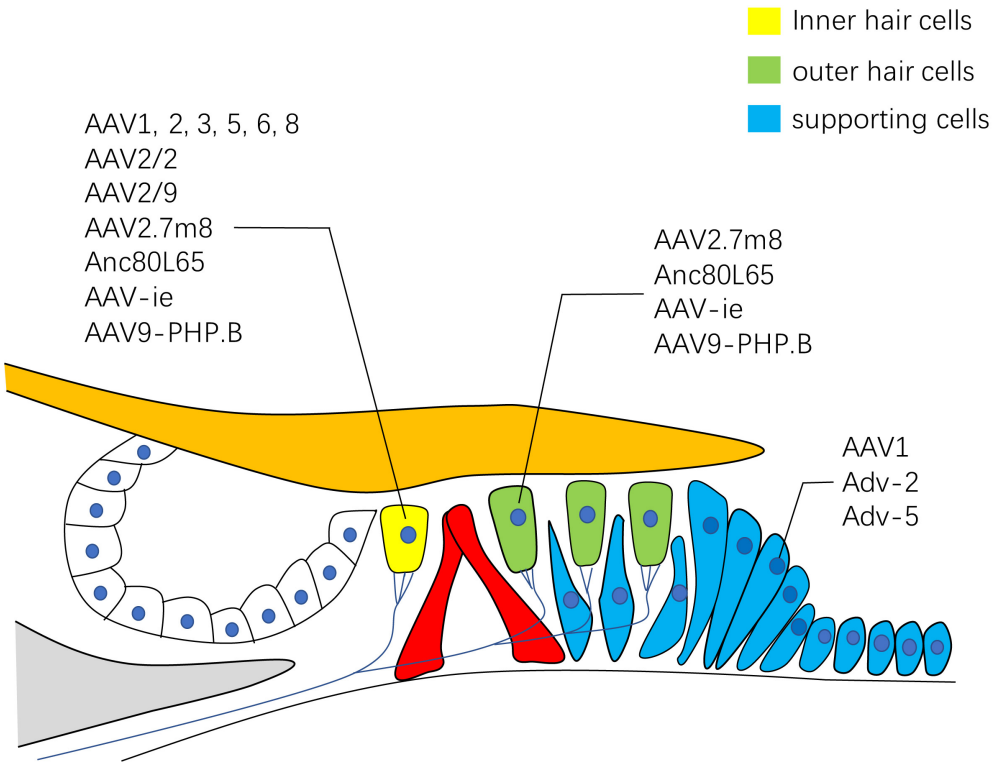

Figure 1. Viral vectors with specific transfection efficiency for different target cells. Studies have shown that AAV2.7m8, Anc80L65, AAV-ie, AAV9-PHP.B have high transfection efficiency in both inner hair cells and outer hair cells; AAV1 , 2, 3, 5, 6, 8 , AAV2/2, AAV2/9 also have higher transfection efficiency in inner hair cells, AAV1, Adv-2, Adv-5 have higher transfection efficiency in supporting cells; Adv: Adenovirus; AAV: adeno-associated virus.

Finally, studies have shown that HC can be regenerated by modulating specific genes. Due to the damage of HC cells in most hearing-related diseases, it is suggested that HC regeneration methods will be widely used in hearing therapy in the future.

Gene therapy in auditory diseases

The sound perception and information transmission organs in the auditory system mainly include inner ear HCs, spiral ganglia neurons, and auditory central organs. The lesions of these cells or tissues can affect the perception and transmission of sound, and ultimately lead to hearing loss. Drug-induced deafness, sudden deafness, hereditary deafness, senile deafness, and noise deafness are clinically common types of sensorineural hearing loss. At present, the treatment of sensorineural hearing loss is mainly by wearing hearing aids and cochlear implants. Gene therapy is a biology-based intervention that does not require any device to reconstruct hearing. It is more convenient and economical for patients with sensorineural hearing loss. Therefore, gene therapy is very important for the treatment of sensorineural hearing loss.

Gene therapy for hereditary deafness

Hereditary deafness refers to hearing organ developmental disorders and hearing impairment due to abnormalities in genetic factors such as genes or chromosomes. Currently, more than one hundred non-syndromic hearing loss genes have been identified, including 71 autosomal recessive genes, 45 autosomal dominant genes, and 5 X-linked genes (https://www. hereditaryhearingloss.org). About 30% of hereditary hearing loss is associated with syndrome (14). There are currently 11 syndromes related to hearing loss, and there are 47 related genes, of which 27 are autosomal recessive, 13 are autosomal dominant, and 4 are autosomal dominant or recessive, 2 are X-linked recessive inheritance (15). Human disease is modeled by establishing animal models of multiple hereditary deafness, followed by gene therapy and intervention. Gene therapy for hereditary deafness has made some progress. Current research results have shown that gene therapy was effective in animal models of multiple hereditary deafness and is expected to be clinically transformed in the future. The popular genes currently studied include *Gjb2* (16), *Vglut3* (17), *Pou4f3* (18), *Tmc1* (19), *Kcnq4* (20), *Ush1c* (21) and *MsrB3* (22). In addition, some potential genes have recently been found to be associated with hearing loss, which may be the new direction of our research in the future, such as *Clarin-2* (22, 23), *Pls1* (24), *Cldn9* (25), etc. However, there are some limitations in the current research involving neonatal mouse models. Mice mature after a few weeks of birth, whereas humans are well-developed at birth, so intervention on newborn mice is similar to intervention at the human fetal stage. To better mimic postnatal genetic deafness, we need to expand the time span of intervention. Recently, Yoshimura et al. reported on the study of the adult mice deafness model of *Tmc1* mutation. They injected microRNA into the cochlea via the AAV vector and showed that RNAi-mediated gene silencing inhibited hearing loss and increased survival of inner hair cells (IHC) (26). This result illustrates the feasibility of gene therapy in adult mouse models.

Gene therapy for drug-induced deafness

Drug-induced deafness is a sensorineural hearing loss caused by the application of antibiotics, antineoplastic drugs, etc. Common ototoxic drugs include aminoglycoside antibiotics and chemotherapeutic drugs such as cisplatin. For drug-induced deafness, there is still no optimized treatment yet. The best way to deal with drug-induced deafness is to reduce chances of its occurrence through early prevention. In recent years, drug deafness has been found to be associated with genetic variation, which may provide a reference for new treatments. Aminoglycoside antibiotics are commonly used antibiotics that often cause ototoxicity, leading to permanent HC loss and hearing damage. The ototoxic effects of aminoglycosides are related to oxidative stress. Studies have confirmed that antioxidant gene therapy has an inhibitory effect on aminoglycoside-induced oxidative stress in the inner ear, thereby promoting HC survival (27). Ototoxicity caused by cisplatin is a serious side effect in patients undergoing cisplatin therapy. However, ototoxicity caused by cisplatin shows significant differences among individuals, which may be due to different genetic backgrounds. Genome-wide association studies (GWAS) have found that ACYP2 (28) and WFS1 (29) variants are closely related to cisplatin-induced ototoxicity, and some studies have reported SOD2 mutations associated with ototoxicity in cisplatin-treated children with medulloblastoma (30). Britt I. Drögemöller et al. have demonstrated that a variant of *Slc16a5* is a novel genetic risk factor for testicular cancer patients. Silencing of *Slc16a5 in vitro* can alter cisplatin-induced cellular responses, suggesting that *Slc16a5* plays a role in cisplatin-induced ototoxicity (31). Other studies have shown that overexpression of X-linked inhibitor of apoptosis protein in a mouse model also has an inhibitory effect on cisplatin-induced hearing loss (32-34).

Gene therapy for senile deafness

Senile deafness, also known as age-related hearing loss (ARHL), is a cumulative pathological and physiological change in the age-related auditory system. Senile deafness is a progressive and irreversible hearing loss, especially at high frequencies. According to the World Health Organization, senile deafness is the second most common disease among the elderly and the third most prevalent disease in the world. It is estimated that by 2025, more than 500 million people will suffer from senile deafness. At present, the etiology of senile deafness is not very clear, and it is generally considered to be caused by interaction of various factors. A large number of studies have shown that mutations in some genes may increase the susceptibility to senile deafness. GWAS have been conducted to identify genes that may be associated with ARHL and found significant mutations in *Prkce* (35), *Tgfb1* (35), *Nrf2* (35), *Grm7* (36), and *Cdh23* (37) in ARHL. In addition, mtDNA4977 (38), *Nkcc1* (39),

mucolipin 1 and 3 (40), *Wfs1* (41), *Slc7a8* (42), *Cox3*, *Gjb2* (43), *Idh2* (44), neuropilin-1 (45), *Igf1* (46, 47), *Essrg* (48), *P2rx2* (49), *Kcnq5* (49), *Erbb3* (49), *Socs3* (49), *Slc26a4* (50), *Spatc1l* (51), *Bak1* (52), *Ccr3* (53) and *Gilz* (53) are also associated with ARHL, which may be potential target genes for the treatment of senile deafness by gene therapy in the future. In addition, in the research of animal models, it is found that activation of *Sirt1* expression activates autophagy pathway, reduces HC death and hearing loss, and prevents the development of senile deafness (54). Senile deafness is closely related to the irreversible death of HCs. The treatment of senile deafness by the protection and regeneration of HCs has attracted the interest of many researchers. With the extensive development of HC regeneration research, a number of potential gene therapy targets have been discovered, the most representative of which is the *Atoh1* gene. The *Atohl* gene is a transcriptional regulator required for HC differentiation. A number of animal studies have demonstrated that the overexpression of the *Atoh1* gene in the inner ear can induce the trans-differentiation of the supporting cells (SCs) in the Corti to the HCs to achieve the purpose of HC regeneration in the cochlear and vestibular (55). At present, the intervention methods for senile deafness are still mainly to improve hearing, such as wearing hearing aids, but in the future, gene therapy is expected to be an effective method for treating ARHL.

Gene therapy for noise deafness

Noise-induced hearing loss (NIHL) is a slow progressive sensorineural deafness caused by prolonged exposure to noise stimuli. It is generally believed that the impairment of noise on hearing is related to the acoustic properties of the noise, the noise environment and individual conditions. Studies have shown that individuals' sensitivity to noise-induced hearing loss is related to genetic factors. CAT, GSTM1, PON2, and SOD2 are significantly associated with activation of the oxidative stress pathway, while HSP70-1 and HSP70-2 mediated heat shock responses provide hearing protection in noise damage (56). It has also been highlighted that P2RX2 is an important protein that attenuates sound transmission in the context of high-intensity noise (57). Noise can cause HC morphology change or even death, accompanied by degeneration of pillar cells, SCs, vascular streaks, peripheral nerve, and ganglion cells. Therefore, the protection and regeneration of hearing-related cells (such as HCs, SCs, etc.) is a key factor in the treatment of NIHL. In addition to the above-mentioned treatments using ATOH1 to induce HC regeneration, brain-derived neurotrophic factor (18) and neurotrophin-3 (NT3) (58) have been shown to promote the growth and maintenance of ribbon synapses and vestibular epithelium. Studies have found that up-regulation of NT3 expression in postnatal mice can regenerate the ribbon synapses, thereby promoting the recovery of cochlear function after hearing injury (59). Although the current application of gene therapy to NIHL is still in the exploratory stage, it has detected significant hearing protection effects after inhibiting hearing loss susceptibility-related genes, up-regulating HC protection-related genes and HC regeneration-related genes.

Conclusion

Gene therapy in the field of hearing is a research hotspot in recent years. Although some progress has been made, most studies are still limited to cellular level or animal models. There are still many mechanisms for clinical transformation to explore. The current limitation of gene therapy is that animal models, gene vectors and delivery pathways need to be further optimized. In addition, current research on gene therapy mainly focuses on sensorineural deafness, but less on other diseases of the auditory system. Gene therapy has potential clinical application prospects, in addition to correcting gene mutations, protecting HCs, SCs and spiral ganglion neurons from various damages, gene therapy may also induce HC regeneration. Currently, there are more than 2,500 clinical trials on gene therapy, including approved, ongoing, and completed, of which 2 are related to hearing treatment (https://clinicaltrials.gov/). With more and more hearing-related genes being identified and the development of gene therapy technology, more hearing-related clinical trials are expected to be conducted. Although gene therapy still faces various problems in the treatment of hearing disorders, in the future, this treatment will become a highly effective and safe treatment for hearing-impaired patients.

Conflict of interest

The authors declare no competing financial interests.

References

1. Guo W, Yi H, Ren L, Chen L, Zhao L, Sun W, et al. The morphology and electrophysiology of the cochlea of the miniature pig. Anat Rec (Hoboken). 2015;298(3):494-500.
2. Guo W, Yi H, Yan Z, Ren L, Chen L, Zhao LD, et al. The morphological and functional development of the stria vascularis in miniature pigs. Reprod Fertil Dev. 2017;29(3):585-93.
3. Ekdale EG. Comparative Anatomy of the Bony Labyrinth (Inner Ear) of Placental Mammals. PLoS ONE. 2013;8(6):e66624.
4. Dai C, Lehar M, Sun DQ, Rvt LS, Carey JP, MacLachlan T, et al. Rhesus cochlear and vestibular functions are preserved after inner ear injection of saline volume sufficient for gene therapy delivery. J Assoc. Res Otolaryngol. 2017;18(4):601-17.
5. György B, Meijer EJ, Ivanchenko MV, Tenneson K, Emond F, Hanlon KS, et al. Gene Transfer with AAV9-PHP.B rescues hearing in a mouse model of usher syndrome 3A and transduces hair cells in a non-human primate. Mol Ther Methods Clin Dev. 2019;13:1-13.
6. DeSmidt AA, Zou B, Grati M, Yan D, Mittal R, Yao Q, et al. Zebrafish model for nonsyndromic X-linked sensorineural deafness, DFNX1. Anat Rec (Hoboken). 2019.
7. Zou B, Desmidt AA, Mittal R, Yan D, Richmond M, Tekin M, et al. The generation of zebrafish mariner model using the CRISPR/Cas9 system. Anat Rec (Hoboken). 2019.
8. Suzuki J, Hashimoto K, Xiao R, Vandenberghe LH, Liberman MC. Cochlear gene therapy with ancestral AAV in adult mice: complete transduction of inner hair cells without cochlear dysfunction. Sci Rep. 2017;7:45524.
9. Gu X, Chai R, Guo L, Dong B, Li W, Shu Y, et al. Transduction of adeno-associated virus vectors targeting hair cells and

supporting cells in the neonatal mouse cochlea. Front Cell Neurosci. 2019;13:8.
10. Tan F, Chu C, Qi J, Li W, You D, Li K, et al. AAV-ie enables safe and efficient gene transfer to inner ear cells. Nat Commun. 2019;10(1):3733.
11. Giannelli SG, Luoni M, Castoldi V, Massimino L, Cabassi T, Angeloni D, et al. Cas9/sgRNA selective targeting of the P23H Rhodopsin mutant allele for treating retinitis pigmentosa by intravitreal AAV9.PHP.B-based delivery. Hum Mol Genet. 2018;27(5):761-79.
12. Driver EC, Kelley MW. Transfection of mouse cochlear explants by electroporation. Curr Protoc Neurosci. 2010;Chapter 4:Unit 4.34.1-10.
13. Wang L, Jiang H, Brigande JV. Gene transfer to the developing mouse inner ear by in vivo electroporation. J Vis Exp. 2012(64).
14. Hilgert N, Smith RJ, Van Camp G. Function and expression pattern of nonsyndromic deafness genes. Curr Mol Med. 2009;9(5):546-64.
15. Carpena NT, Lee MY. Genetic Hearing Loss and Gene Therapy. Genomics Inform. 2018;16(4):e20.
16. Iizuka T, Kamiya K, Gotoh S, Sugitani Y, Suzuki M, Noda T, et al. Perinatal Gjb2 gene transfer rescues hearing in a mouse model of hereditary deafness. Hum Mol Genet. 2015;24(13):3651-61.
17. Akil O, Seal RP, Burke K, Wang C, Alemi A, During M, et al. Restoration of hearing in the VGLUT3 knockout mouse using virally mediated gene therapy. Neuron. 2012;75(2):283-93.
18. Fukui H, Wong HT, Beyer LA, Case BG, Swiderski DL, Di Polo A, et al. BDNF gene therapy induces auditory nerve survival and fiber sprouting in deaf Pou4f3 mutant mice. Sci Rep. 2012;2:838.
19. Nist-Lund CA, Pan B, Patterson A, Asai Y, Chen T, Zhou W, et al. Improved TMC1 gene therapy restores hearing and balance in mice with genetic inner ear disorders. Nat Commun. 2019;10(1):236.
20. Kesser BW, Hashisaki GT, Holt JR. Gene transfer in human vestibular epithelia and the prospects for inner ear gene therapy. Laryngoscope. 2008;118(5):821-31.
21. Pan B, Askew C, Galvin A, Heman-Ackah S, Asai Y, Indzhykulian AA, et al. Gene therapy restores auditory and vestibular function in a mouse model of Usher syndrome type 1c. Nat Biotechnol. 2017;35(3):264-72.
22. Kim MA, Cho HJ, Bae SH, Lee B, Oh SK, Kwon TJ, et al. Methionine sulfoxide reductase B3-targeted in utero gene therapy rescues hearing function in a mouse model of congenital sensorineural hearing loss. Antioxid Redox Signal. 2016;24(11):590-602.
23. Dunbar LA, Patni P, Aguilar C, Mburu P, Corns L, Wells HR, et al. Clarin-2 is essential for hearing by maintaining stereocilia integrity and function. EMBO Mol Med. 2019;11(9):e10288.
24. Morgan A, Koboldt DC, Barrie ES, Crist ER, García García G, Mezzavilla M, et al. Mutations in PLS1, encoding fimbrin, cause autosomal dominant nonsyndromic hearing loss. Human mutation. 2019.
25. Sineni CJ, Yildirim-Baylan M, Guo S, Camarena V, Wang G, Tokgoz-Yilmaz S, et al. A truncating CLDN9 variant is associated with autosomal recessive nonsyndromic hearing loss. Hum Mutat. 2019;138(10):1071-5.
26. Yoshimura H, Shibata SB, Ranum PT, Moteki H, Smith RJH. Targeted allele suppression prevents progressive hearing loss in the mature murine model of human TMC1 deafness. Molecular therapy : the journal of the American Society of Gene Therapy. 2019;27(3):681-90.
27. Kawamoto K, Sha SH, Minoda R, Izumikawa M, Kuriyama H, Schacht J, et al. Antioxidant gene therapy can protect hearing and hair cells from ototoxicity. Mol Ther. 2004;9(2):173-81.
28. Xu H, Robinson GW, Huang J, Lim JY, Zhang H, Bass JK, et al. Common variants in ACYP2 influence susceptibility to cisplatin-induced hearing loss. Nat Genet. 2015;47(3):263-6.
29. Wheeler HE, Gamazon ER, Frisina RD, Perez-Cervantes C, El Charif O, Mapes B, et al. Variants in and other mendelian deafness genes are associated with cisplatin-associated ototoxicity. Clin Cancer Res. 2017;23(13):3325-33.
30. Brown AL, Lupo PJ, Okcu MF, Lau CC, Rednam S, Scheurer ME. SOD2 genetic variant associated with treatment-related ototoxicity in cisplatin-treated pediatric medulloblastoma. Cancer Med. 2015;4(11):1679-86.
31. Drögemöller BI, Monzon JG, Bhavsar AP, Borrie AE, Brooks B, Wright GEB, et al. Association between SLC16A5 genetic variation and cisplatin-induced ototoxic effects in adult patients with testicular cancer. JAMA Oncol. 2017;3(11):1558-62.
32. Cooper LB, Chan DK, Roediger FC, Shaffer BR, Fraser JF, Musatov S, et al. AAV-mediated delivery of the caspase inhibitor XIAP protects against cisplatin ototoxicity. Otol Neurotol. 2006;27(4):484-90.
33. Jie H, Tao S, Liu L, Xia L, Charko A, Yu Z, et al. Cochlear protection against cisplatin by viral transfection of X-linked inhibitor of apoptosis protein across round window membrane. Gene Ther. 2015;22(7):546-52.
34. Chan DK, Lieberman DM, Musatov S, Goldfein JA, Selesnick SH, Kaplitt MG. Protection against cisplatin-induced ototoxicity by adeno-associated virus-mediated delivery of the X-linked inhibitor of apoptosis protein is not dependent on caspase inhibition. Otol Neurotol. 2007;28(3):417-25.
35. Fetoni AR, Zorzi V, Paciello F, Ziraldo G, Peres C, Raspa M, et al. Cx26 partial loss causes accelerated presbycusis by redox imbalance and dysregulation of Nfr2 pathway. Redox Biol. 2018;19:301-17.
36. Newman DL, Fisher LM, Ohmen J, Parody R, Fong CT, Frisina ST, et al. GRM7 variants associated with age-related hearing loss based on auditory perception. Hear Res. 2012;294(1-2):125-32.
37. Wang T, Yang J, Ji X, Chu M, Zhang R, Dai J, et al. Pathway analysis for a genome-wide association study of pneumoconiosis. Toxicol Lett. 2015;232(1):284-92.
38. Ueda N, Oshima T, Ikeda K, Abe K, Aoki M, Takasaka T. Mitochondrial DNA deletion is a predisposing cause for sensorineural hearing loss. Laryngoscope. 1998;108(4 Pt 1):580-4.
39. Liu Y, Chu H, Chen J, Zhou L, Chen Q, Yu Y, et al. Age-related change in the expression of NKCC1 in the cochlear lateral wall of C57BL/6J mice. Acta Otolaryngol. 2014;134(10):1047-51.
40. Wiwatpanit T, Remis NN, Ahmad A, Zhou Y, Clancy JC, Cheatham MA, et al. Codeficiency of lysosomal mucolipins 3 and 1 in cochlear hair cells diminishes outer hair cell longevity and accelerates age-related hearing loss. J Neurosci. 2018;38(13):3177-89.
41. Kytövuori L, Hannula S, Mäki-Torkko E, Sorri M, Majamaa K. A nonsynonymous mutation in the WFS1 gene in a Finnish family with age-related hearing impairment. Hear Res. 2017;355:97-101.
42. Espino Guarch M, Font-Llitjós M, Murillo-Cuesta S, Errasti-Murugarren E, Celaya AM, Girotto G, et al. Mutations inL-type amino acid transporter-2 support as a novel gene involved in age-related hearing loss. ELife. 2018;7.
43. Lin X, Li G, Zhang Y, Zhao J, Lu J, Gao Y, et al. Hearing consequences in Gjb2 knock-in mice: implications for human p.V37I mutation. Aging. 2019;11(18):7416-41.
44. White K, Kim MJ, Han C, Park HJ, Ding D, Boyd K, et al. Loss of IDH2 accelerates age-related hearing loss in male mice. Sci Rep. 2018;8(1):5039.
45. Salehi P, Ge MX, Gundimeda U, Michelle Baum L, Lael Cantu H, Lavinsky J, et al. Role of neuropilin-1/semaphorin-3A signaling in the functional and morphological integrity of the cochlea. PLoS Genet. 2017;13(10):e1007048.
46. Paulsen AJ, Cruickshanks KJ, Pinto A, Schubert CR, Dalton DS, Fischer ME, et al. Neuroprotective factors and incident hearing impairment in the epidemiology of hearing loss study.

Laryngoscope. 2019;129(9):2178-83.
47. Riquelme R, Cediel R, Contreras J, la Rosa Lourdes RD, Murillo-Cuesta S, Hernandez-Sanchez C, et al. A comparative study of age-related hearing loss in wild type and insulin-like growth factor I deficient mice. Front Neuroanat. 2010;4:27.
48. Nolan LS, Maier H, Hermans-Borgmeyer I, Girotto G, Ecob R, Pirastu N, et al. Estrogen-related receptor gamma and hearing function: evidence of a role in humans and mice. Neurobiol Aging. 2013;34(8):2077.e1-9.
49. Bouzid A, Smeti I, Dhouib L, Roche M, Achour I, Khalfallah A, et al. Down-expression of P2RX2, KCNQ5, ERBB3 and SOCS3 through DNA hypermethylation in elderly women with presbycusis. Biomarkers. 23(4):347-56.
50. Xu J, Zheng J, Shen W, Ma L, Zhao M, Wang X, et al. Elevated SLC26A4 gene promoter methylation is associated with the risk of presbycusis in men. Mol Med Rep. 2017;16(1):347-52.
51. Morgan A, Vuckovic D, Krishnamoorthy N, Rubinato E, Ambrosetti U, Castorina P, et al. Next-generation sequencing identified SPATC1L as a possible candidate gene for both early-onset and age-related hearing loss. Eur J Hum Genet. 2019;27(1):70-9.
52. Falah M, Najafi M, Houshmand M, Farhadi M. Expression levels of the BAK1 and BCL2 genes highlight the role of apoptosis in age-related hearing impairment. Clin Interv Aging. 2016;11:1003-8.
53. Dong Y, Li M, Liu P, Song H, Zhao Y, Shi J. Genes involved in immunity and apoptosis are associated with human presbycusis based on microarray analysis. Acta Otolaryngol. 2014;134(6):601-8.
54. Pang J, Xiong H, Ou Y, Yang H, Xu Y, Chen S, et al. SIRT1 protects cochlear hair cell and delays age-related hearing loss via autophagy. Neurobiol Aging. 2019;80:127-37.
55. Izumikawa M, Minoda R, Kawamoto K, Abrashkin KA, Swiderski DL, Dolan DF, et al. Auditory hair cell replacement and hearing improvement by Atoh1 gene therapy in deaf mammals. Nat Med. 2005;11(3):271-6.
56. Clifford RE, Hoffer M, Rogers R. The genomic basis of noise-induced hearing loss: a literature review organized by cellular pathways. Otol Neurotol. 2016;37(8):e309-16.
57. Housley GD, Morton-Jones R, Vlajkovic SM, Telang RS, Paramananthasivam V, Tadros SF, et al. ATP-gated ion channels mediate adaptation to elevated sound levels. Proc Natl Acad Sci USA. 2013;110(18):7494-9.
58. Chen H, Xing Y, Xia L, Chen Z, Yin S, Wang J. AAV-mediated NT-3 overexpression protects cochleae against noise-induced synaptopathy. Gene Ther. 2018;25(4):251-9.
59. Wan G, Gómez-Casati ME, Gigliello AR, Liberman MC, Corfas G. Neurotrophin-3 regulates ribbon synapse density in the cochlea and induces synapse regeneration after acoustic trauma. ELife. 2014;3.

REVIEW ARTICLE

Mutation detection and molecular targeted tumor therapies

Yamin WANG, Zhong CHEN*

Natural Sciences and Science Education, National Institute of Education, Nanyang Technological University, Singapore 637616, Singapore.

*Correspondence: zhong.chen@nie.edu.sg
https://doi.org/10.37175/stemedicine.v1i1.11

ABSTRACT

Rapid advancement in genomic technologies has greatly enhanced the potential of clinical recognition and application of molecular targets. Specifically, gene mutation detection technologies are of great significance in the early diagnosis, customized drug delivery guidance, treatment progression, and monitoring of tumor's drug resistance. Gene mutation detection or genetic typing of patients is a prerequisite for molecular targeted therapies. Most kinds of targeted therapies treat cancers by interfering with specific proteins that are involved in tumorigenesis. Compared with traditional chemotherapies, molecular targeted therapies have many advantages, despite that they still have risks of resistance, side effects and leak of genetic information.

Keywords: Gene mutation detection · Molecular targeted therapy · Tumor

Introduction

In 2018, there are an estimated 18.1 million new cancer cases and 9.6 million cancer deaths worldwide (estimated data on the proportion of all cancers in all ages and genders including non-melanoma skin cancer) (1). Cancer is a disease with extremely high mortality and is difficult to prevent. The cure rate for advanced cancer is low globally. Fortunately, the death rate could be decreased through early diagnosis (2). At present, the methods for screening cancer mainly include the detection of serum tumor markers, B-ultrasound, CT, and radiology (3, 4). Because of lacking pre-diagnosis characters, it is often an advanced cancer when abnormalities are found by traditional methods. Therefore, early prevention, diagnosis and treatment are crucial to fight against cancer.

A gene is a DNA or RNA fragment that carries specific genetic information. A gene mutation is a change in the composition or arrangement of base pairs occurring in its molecular structure, including point mutations, frameshift mutations, deletion mutations, and insertion mutations. Research studies have found that the occurrence of tumors is essentially the result of the interaction of environmental factors and genetic factors, and the pathological process involves mutations of various genes (5). Tumor-associated genes are often susceptible to activation of oncogenes, inactivation or loss of tumor suppressor genes, causing malignant transformation of cells and thereby forming tumors that threaten human life (6). In addition, there are cases of abnormal expression of genes involved in the development of cancer drug resistance, causing negative effects on clinic treatment (7). Genetic testing is a technique for detecting DNA in human blood, body fluids, or cells that can be used for disease diagnosis or disease risk prediction. Detection of these types of mutations present in tumor tissue not only helps doctors understand the mechanism of tumorigenesis, but also serves as a molecular marker for tumor susceptibility assessment and diagnosis. It is of great practical significance to systematically search for genetic variation of multiple susceptible genes involved in the pathogenesis of tumors, to elucidate the mechanism of early tumor development, and to reveal molecular targets for early warning, early diagnosis and early treatment of tumors.

Approaches to detect mutation of cancer and molecular targeted therapies in clinical applications are significant. First, tumor gene testing can screen early cancers and discover familial susceptibility genes. It is expected to achieve zero-level prevention so as not to occur or delay the appearance of preclinical symptoms. For example, breast cancer is one of the most common and malignant tumors in women. Human breast cancer susceptibility genes (*BRCA1* and *BRCA2*) are currently known as high phenotypic susceptibility genes for breast cancer. Studies have found that women who develop *BRCA1* gene-causing mutations at the age of 70 have a 72% risk of developing breast cancer. Those who carry the *BRCA2* gene pathogenic mutation have a 69% risk of developing

breast cancer (8). Second, tumor gene mutation detection can predict the efficacy of tumor-targeted drugs (9, 10). The indications and doses of clinical drugs are set according to the results or the average of the population in clinical trials. Hence it is difficult to judge the effectiveness of the drugs in patients. With the research development and clinical application of tumor-targeted drugs, gene mutation detection coupled with diagnostic program in drug applications ensure safe and effective administration of drugs.

Tumor molecular targeted therapy utilizes the molecular difference between tumor cells and healthy cells. Tumor proto-oncogene products or their signaling pathways are used as therapeutic targets to select drugs. Furthermore, they effectively interfere with signal transduction pathways regulated by the molecules which are closely related to tumorigenesis, thereby achieving the effects of inhibiting tumor growth, progression and metastasis. Molecular targeted therapeutics include monoclonal antibodies directed against specific cellular markers, signaling inhibitors, anti-angiogenic drugs, and drugs against certain cytogenetic markers or oncogene products (11, 12). Compared with traditional chemotherapeutic drugs, these drugs have the characteristics of targeting without cytotoxicity, and mainly act to regulate and stabilize tumor cells.

Techniques for mutation detection

Sequencing

At present, sequencing techniques mainly applied in gene mutation detection include Sanger sequencing, pyrosequencing, next generation sequencing (NGS), etc (13-15).

Sanger sequencing

Sanger sequencing is widely utilized in the research field of human genes. The human genome project is one of the greatest milestone set for this technique. The method uses DNA single strand as a template, and with the presence of template specific primers, DNA polymerase adds four types of either dNTPs or dideoxyribonucleoside triphosphates (ddNTPs) labeled with different color dyes according to the principle of base complementary pairing. The 3'-hydroxyl terminus of the primer, and the primer strand is extended or the extension process is terminated when a ddNTP is added to obtain various serial lengths of DNA fragments. Following electrophoresis separation, the base of each fragment can be detected by laser induced fluorescence method. The advantage of this method is that as current gold standard sequencing methods, almost all genetic mutations can be detected (16). However, this method is limited by its poor quantitative performance. When detecting individual gene mutations, the sensitivity is poor, time-consuming, and laborious. In addition, the signal intensity of the Sanger sequencing is directly related to the amount of template. The lowest detection limit when applied to gene mutation detection is about 10%. When the mutation is less than 10%, the detection error is extremely large (17).

Pyrosequencing

Pyrosequencing is a high-throughput, low-cost, highly automated sequencing technology with a minimum detection sensitivity of 5% when detecting gene mutations. This technology does not require gel electrophoresis assistance, nor special marking, nor dye treatment of samples. It has the advantages of saving time and labor, user friendly, intuitive and easy-to-understand results with short detection process (13). At present, pyrosequencing technology has become an important means for the analysis of gene mutations, and is widely used in the diagnosis and treatment of a variety of tumors.

Next generation sequencing (NGS)

In general, the broader the range of genomes being sequenced, the more comprehensive the analysis of disease-causing genomic mutation. Whole-genome sequencing provides comprehensive analysis of genomic-level variation, especially large structural variation (copy number variation, inversion, translocation), and unpredictable types of unknown mutation. Based on data from the National Human Genome Research Institute (NHGRI), the cost of sequencing the whole genome has fallen dramatically, it is about $0.014 per Mb, but the absolute cost is still high. However, the technology is widely used in clinics and large-scale studies based on its efficiency (18). Whole exon sequencing includes 30 million base pairs, which can explain more than 85% of tumour mutations, yet currently limited in scope due to cost constraints (19). For the detection of tumour-related genes, the detection of tens to hundreds of genes is the most extensive in the clinic.

Next-generation sequencing is an effective method used clinically for mutation detection. **Table 1** shows common next-generation sequencing platforms (20). The basic parameters are: sensitivity and specificity of the experiment, accuracy, upper and lower limits (dynamic range) of the detection capability. The most important specification of all is the sensitivity of the analysis. The analytical sensitivity of next-generation sequencing usually means that when the ratio of a mutation to a normal gene is below a certain value, it cannot be detected. Mutations include single nucleotide polymorphisms (SNPs), multiple copy variants (CNVs), consecutive homopolymers (21). The analytical sensitivity of each mutation is examined separately. Researchers often refer to a gold standard method to detect NGS technology. For example, mutations in the same patient tissue are used as the gold standard for circulating tumour DNA (ctDNA) detection (22). It is also possible to construct specific analytes, such as plasmids for constructing mutated genes and plasmids containing wild-type genes, and mixing them in a certain ratio after dilution to test the variation of NGS technology as well as the dynamic range of its capabilities. In addition, other detection methods (Sanger sequencing, chips) and "positive controls" can be used to verify the inspection performance of NGS experiments

(23). The gold standard refers to the more reliable methodologies, however it does not indicate in any waythat the result of each gold standard is more reliable than the next-generation sequencing.

Table 1. Next generation sequencing platform and its characteristics.

Method	Advantages	Disadvantages
Roche 454 sequencing	Long-read	High error rate at multiple consecutive sequences
Illumina Genome Analyzer	Relatively cheap, popular	Short-read, affected by PCR amplification errors
Illumina Hiseq 2000	High-throughput, below 1ug samples	Short-read, high false positives
ABI SOLiD system	Lower error rate than Illumina	Time-consuming, high-cost
Ion Torrent Sequencer	Small, cheap	High error rate at multiple consecutive sequences
Gene Reader	Similar to Illumina	Short-read, affected by PCR amplification errors
PaciBio RS	No need to amplify DNA, the reading length is 800-1000bp	The instrument is expensive, high error rate, low flux
Heliscope Sequencer	DNA sequencing without bias	NTP incorporation, high error rate
Oxford Nanopore	Currently the fastest, complete genome sequencing in 15 minutes	High cost, less research data

The broader the scope of genomic detection, the more unknown mutations can be detected. Therefore, some problems are also highlighted. The first problem is sampling. The best way to detect this is to use a paraffin section containing a tissue sample. However, any single section of a tumor sample might not represent the entire heterogeneity of the whole tumor. However, circulating tumour cells (CTC) can be used for detection, to promote better theoretical effect as the genome is more complete to represent the heterogeneity of tumour cells. However, the separation efficiency of CTC is relatively low (24). Liquid biopsy of tumors is also an uprising direction in clinical research. The second problem is that unknown mutations are difficult to identify due to its many forms such as new SNP, nonsense, sense of antisense mutations. This is a common problem encountered in high throughput sequencing. In addition to varied literature, family analysis is also needed, which requires additional in-depth research and is often clinically challenging. The third issue is the ethics of patient privacy. When performing high-throughput analysis of tumors, other diseases not in current focus might be found as well and patients might not be mentally prepared.

AS-PCR

Allele-specific polymerase-chain-reaction amplification (AS-PCR) as a tool for mutation detection is based on the design of primers to detect single nucleotide polymorphism (SNP) sites (25). For instance, the method has the characteristics of simple operation, low cost, shorter time, and reliable results. It has been used in *EGFR* mutation detection in non-small-cell lung cancer (26), *KIT D816V* and *D816F* mutation in acute myelogenous leukemia and mastocytosis (27). The sensitivity of AS-PCR can be as low as 1% (28).

Amplification refractory mutation system ARMS-PCR

Amplification refractory mutation system (ARMS) is also known as allele specific amplification (ASA). Allele-specific PCR amplification primers were designed using the principle that the 3'-end base of the PCR primer must be complementary to its template DNA for efficient amplification. The technique consists of designing two 5' primers, one complementary to normal DNA and another complementary to the mutated DNA. For homozygous mutations, the two primers and the 3' primer are added separately for two parallel PCRs. Under stringent conditions, a PCR amplification band can only occur when the primer 3' base is paired with a template. If the mismatch is located at the 3' end of the primer, PCR would not work. Therefore, it can be used to detect mutations. ARMS technology uses a specific primer to perform high-accuracy PCR amplification of DNA mutation target sequences on a real-time PCR platform, and a fluorescently labeled probe to detect mutations in the amplified product. Compared with direct sequencing, the ARMS method is straightforward, rapid, specific, and sensitive. Moreover, it can detect mutant allele level as low as 0.5% (29).

High resolution melting curve analysis (HRM)

High resolution melting curve (HRM) analysis is a relatively new post-PCR analysis method that can be used to identify differences in nucleic acid sequences. Because each dsDNA fragment has its specific melting signature, determined by GC content, length, and sequence composition, sequence changes can result in changes in the melting characteristics of the dsDNA fragment. High-resolution melting curve (HRM) analysis is an extension of melting curve analysis that maximizes the amount of information that can be extracted. The core of this approach is to detect small differences in the PCR melting (dissociation) curve (30). This is achieved with a high-brightness dsDNA-binding dye and real-time PCR instrument that precisely controls temperature changes and consists of advanced data acquisition capability. The data is analyzed and manipulated using software designed for HRM.

Since the DNA-saturated fluorescent dye binds to DNA during DNA unwinding, rearrangement does not occur, so the melting curve has a higher resolution. Commonly used HRM dyes are from LC Green family (LC Green I and LC Green Plus), Eva Green, SYTO9 and Reso Light, and the like. This method has the following advantages. **(1)** Low reagent consumption, low waste rate: HRM requires only (20 μL) of PCR reaction volume to analyze a single sample without the use of HPLC solvents or DGGE gels. **(2)** Simple and fast workflow: no additional equipment is required after PCR amplification. A high-resolution melting curve can be added at the end of amplification and analyzed immediately after completion. **(3)** Rapid optimization: unlike DHPLC technology, it does not require thermal optimization. **(4)** Low sample consumption: in the subsequent analysis of HRM, the PCR amplification product can be directly used for the

Sanger sequencing reaction (31).

Mutation detection and molecular targeted therapies-recent advances on the diagnosis and treatment of tumor

In recent years, cancer researchers have discovered specific genes associated with cancer growth. By targeting specific gene mutations that lead to cancer growth, targeted therapies can accurately identify and attack cancer cells, which have a very promising future in the treatment of cancer (32). Molecular targeted therapies can reduce damage to normal cells, thus they are more optimal options. There are many potential genetic mutations that can lead to tumor growth, and these mutations can be detected by genetic testing. Molecular testing for mutation improves diagnosis and treatment of tumors by detecting cancer in early stage, determining prognosis, and monitoring disease progression or therapeutic responses (33). Based on the specific characteristics of individual patient's tumor gene, such information can help doctors better select targeted therapy for patients.

Molecular targeted therapies

Molecular targeted therapy (MTT) is a research hotspot in the field of cancer therapy in recent years. It has been characterized by high efficiency and low toxicity in the treatment of gastrointestinal stromal tumors, lymphoma, breast cancer, colorectal cancer, and non-small cell lung cancer (34-38). It targets some of the iconic molecules overexpressed in tumor cells, and selects targeted blocking agents to effectively interfere with the signaling pathways closely related to tumorigenesis, thereby inhibiting tumor growth, progression and metastasis (39). Compared with traditional chemotherapeutic drugs, these drugs have the characteristics of non-cytotoxicity, mainly regulating and stabilizing tumor cells with high specificity.

Monoclonal antibodies

Trastuzumab

Trastuzumab, also known as Herceptin, is a humanized inlay and monoclonal antibody whose target is the HER-2 protein, an expression product of the oncogene on the cell membrane. *HER-2* expression status is an independent prognostic factor for breast cancer, with approximately one-third of breast cancer patients overexpressed (36). Clinical use of trastuzumab can improve the efficacy and prolong survival of advanced relapsing and metastatic breast cancer.

Rituximab

Rituximab, also known as Rituximab (Rituxan, Mabthera), a monoclonal antibody against the B cell CD20 antigen, consists of a high-purity part of the murine variable region and a human-derived stable region. The chimera recognizes malignant B cells and normal B cells with CD20 cell markers but has no effect on other normal cells. It is the first FDA-approved monoclonal antibody for the treatment of tumors (40). In general, CD20 is expressed in more than 90% of B lymphocyte lymphomas (NHL). The mechanism of the action of rituximab is multifaceted: **(1)** it can induce antibody-dependent cytotoxicity (ADCC); **(2)** complement-mediated cytolytic action (CDC); and **(3)** programmed cell death, apoptosis; **(4)** it can make chemo resistant tolerant lymphoma cells re-sensitized (41).

Cetuximab

Cetuximab, also known as Ibizo (IMC-C225, Erbitux), is the first approved monoclonal antibody to be marketed and is an IgG1 monoclonal antibody against EGFR. The inhibition of tyrosine kinase (TK) binding to EGFR blocks the intracellular signaling pathway, thereby inhibiting the proliferation of cancer cells, inducing apoptosis of cancer cells, and reducing the production of matrix metalloproteinases and vascular endothelial growth factors (42).

Small-molecule drugs

The epidermal growth factor receptor (EGFR) is a transmembrane receptor composed of glycoproteins and is a member of the tyrosine kinase growth factor receptor family, also known as HER1. The family has a total of four members, namely HER1, HER2, HER3, and HER4. These receptors play an important role in regulating cell growth, differentiation and survival. EGFR is expressed in varying degrees in a significant proportion of tumors, such as knot (straight) intestinal cancer, head and neck squamous cell carcinoma, pancreatic cancer, lung cancer, breast cancer, kidney cancer and glioblastoma. It is now known that EGFR plays an important role in the growth, repair and survival of swollen cancer cells. Its overexpression is often associated with poor prognosis, rapid metastasis, and short survival. EGFR inhibitors may possess anti-cancerous properties through pro-apoptosis, anti-angiogenesis, anti-differentiation and proliferation, and anti-cell migration (43). They often work synergistically with chemotherapy and radiotherapy. Preclinical studies have shown that blocking EGFR can inhibit tumor growth.

Gefitinib

Gefitinib, also known as Iressa, is an aniline quinazoline compound that is a potent human EGFR tyrosine kinase inhibitor. It blocks the signal transduction pathways involve cancer cell proliferation, growth and survival. In July 13, 2015, the US FDA approved gefitinib monotherapy for locally advanced or metastatic non-small cell lung cancer (NSCLC) with failed platinum and docetaxel treatment (44). The drug has more than 100,000 reports worldwide and is a mature method in tumor bio-targeted therapy.

Erlotinib

Erlotinib, also known as Tarceva, is another quinazoline compound. It selectively inhibits EGFR tyrosine kinase

and reduces autophosphorylation of EGFR, leading to cell growth arrest and apoptosis. Erlotinib has an advantage over survival compared to placebo (45). On November 18, 2004, the US FDA officially approved the erlotinib market for the treatment of locally advanced or metastatic NSCLC (46). In vitro experiments have confirmed that it is effective against breast cancer, NSCLC and ovarian cancer.

Bevacizumab

Bevacizumab (Avastin, Avastin) is the first anti-angiogenic drug approved by the FDA for use in malignant tumors. It is a humanized IgG monoclonal antibody artificially synthesized against vascular endothelial growth factor (VEGF). After binding to VEGF, Avastin can block the binding of VEGF to endothelial cell surface receptors F1t-1 and KDR, so that VEGF cannot promote the proliferation of vascular endothelial cells and tumor angiogenesis. This blocks the supply of blood, oxygen, and other essential nutrients essential for tumor growth, making tumor cells impossible to grow, spread, and metastasize in the body (47).

Endostar

Endostar (YH-16), the recombinant human endostatin, is the world's first anti-tumor drug for endostatin. By inhibiting the migration of vascular endothelial cells to inhibit the formation of tumor angiogenesis, the nutrient supply to tumor cells is blocked, thereby achieving the purpose of inhibiting tumor cell proliferation or metastasis (48).

Conclusion and perspectives

The molecular mechanisms underlying the course of cancer are extremely complex. With the in-depth study of molecular genetics research, more and more tumor cell gene structures and related signal transduction pathways have been discovered, hence gene detection technologies will be continuously improved and innovated. Tumor genetic testing will be more widely used in the diagnosis, prevention and treatment of clinical tumors in conjunction with the patient's clinical relevance, cost and clinical care, so as to predict the risk of tumors, improve the efficiency of treatment, reduce the side effects of drugs, resulting in better quality of lives in patients. Mutation detection technologies mentioned in the review are illustrated in Figure 1. Although there are disadvantages concerning each technology, such as limitation in sensitivity of technologies for mutation detection (Table 2), we believe that advances in technologies will increase the sensitivity and accuracy of mutation detection of tumors and studies will be conducted to explain more unknown genes' functions screened by sequencing.

Table 2. Comparation of sensitivity of technologies for mutation detection.

Type	Sensitivity
Sanger sequencing	10-20%
Pyrosequencing	5%
NGS	10%
AS-PCR	1%
ARMS-PCR	0.5%
HRM	1%

Molecular targeted therapy has made great progress in the treatment of cancer, opening up new avenues for the treatment of malignant tumors with poor efficacy of cytotoxic drugs. However, there are also many challenges, such as specific adverse reactions caused by targeted drugs. Skin reactions, interstitial lung disease and cardiovascular adverse reactions are some examples of those. In addition, rational design of treatment regimens, evaluation criteria for therapeutic effects, combined use with traditional anti-tumor methods, and possible drug resistance issues are worthy of further research and exploration.

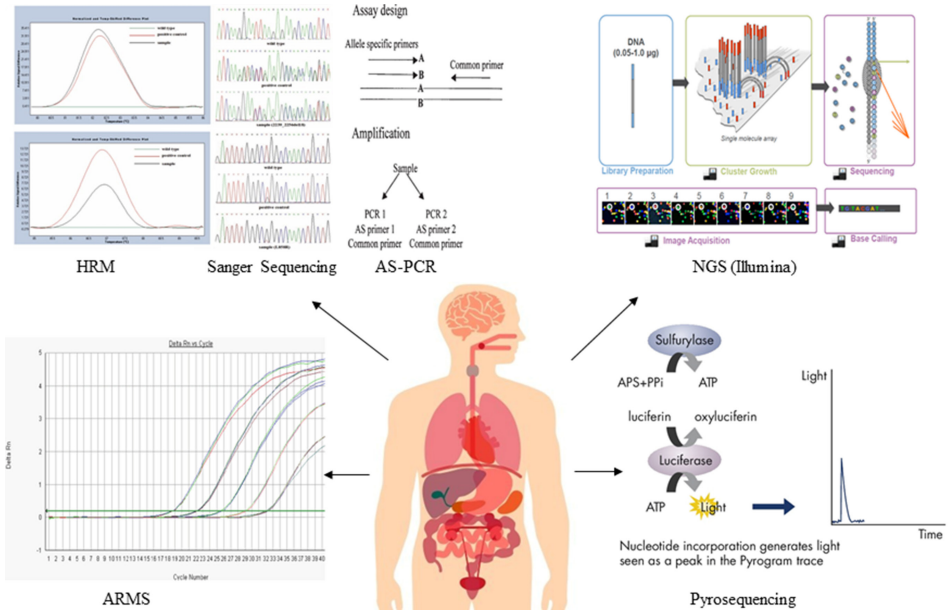

Figure 1. Mutation detection technologies. Images of HRM, Sanger sequencing, ARMS, and AS-PCR were adapted from (23, 24, 27) .

Acknowledgements
Authors thank the core funding from National Institute of Education, Nanyang Technological University Singapore.

Conflict of interest
Authors declare no conflict of interest.

Funding body
National Institute of Education, Nanyang Technological University Singapore.

References

1. Bray F, Ferlay J, Soerjomataram I, Siegel RL, Torre LA, Jemal A. Global cancer statistics 2018: GLOBOCAN estimates of incidence and mortality worldwide for 36 cancers in 185 countries. CA Cancer J Clin. 2018;68(6):394-424.
2. Wang L. Early diagnosis of breast cancer. Sensors (Basel, Switzerland). 2017;17(7).
3. Wu ZM. [Comparative study of nuclear imaging with 99mTc-PMT, B ultrasound and CT in the diagnosis of hepatic tumors]. Zhonghua Fang She Xue Za Zhi. 1988;22(6):329-33.
4. Jiang XT, Tao HQ, Zou SC. Detection of serum tumor markers in the diagnosis and treatment of patients with pancreatic cancer. Hepatobiliary Pancreat Dis Int. 2004;3(3):464-8.
5. Vogelstein B, Kinzler KW. Cancer genes and the pathways they control. Nat Med. 2004;10(8):789-99.
6. Maiuri MC, Tasdemir E, Criollo A, Morselli E, Vicencio JM, Carnuccio R, et al. Control of autophagy by oncogenes and tumor suppressor genes. Cell Death Differ. 2008;16:87.
7. Wang Y, Liu L, Chen Z. Transcriptome profiling of cervical cancer cells acquired resistance to cisplatin by deep sequencing. Artif Cells Nanomed Biotechnol. 2019;47(1):2820-9.
8. Kuchenbaecker KB, Hopper JL, Barnes DR, Phillips KA, Mooij TM, Roos-Blom MJ, et al. Risks of breast, ovarian, and contralateral breast cancer for BRCA1 and BRCA2 mutation carriers. JAMA. 2017;317(23):2402-16.
9. Okamoto I. Epidermal growth factor receptor in relation to tumor development: EGFR-targeted anticancer therapy. FEBS J. 2010;277(2):309-15.
10. Sapiezynski J, Taratula O, Rodriguez-Rodriguez L, Minko T. Precision targeted therapy of ovarian cancer. J Control Release. 2016;243:250-68.
11. Sharkey RM, Goldenberg DM. Targeted therapy of cancer: new prospects for antibodies and immunoconjugates. CA Cancer J Clin. 2006;56(4):226-43.
12. Kelly CM, Power DG, Lichtman SM. Targeted therapy in older patients with solid tumors. J Clin Oncol. 2014;32(24):2635-46.
13. Harrington CT, Lin EI, Olson MT, Eshleman JR. Fundamentals of pyrosequencing. Arch Pathol Lab Med. 2013;137(9):1296-303.
14. Stratton MR, Campbell PJ, Futreal PA. The cancer genome. Nature. 2009;458:719.
15. Di Fiore F. Clinical relevance of KRAS mutation detection in metastatic colorectal cancer treated by Cetuximab plus chemotherapy. Br J Cancer. 2007;96(8):1166-9.
16. Warth A, Penzel R, Brandt R, Sers C, Fischer JR, Thomas M, et al. Optimized algorithm for Sanger sequencing-based EGFR mutation analyses in NSCLC biopsies. Virchows Arch. 2012;460(4):407-14.
17. McGinn S, Gut IG. DNA sequencing - spanning the generations. N Biotechnol. 2013;30(4):366-72.
18. Di Resta C, Ferrari M. Next generation sequencing: from research area to clinical practice. EJIFCC. 2018;29(3):215-20.
19. Meyerson M, Gabriel S, Getz G. Advances in understanding cancer genomes through second-generation sequencing. Nat Rev Genet. 2010;11(10):685-96.
20. Mardis ER. Next-generation sequencing platforms. Annu Rev Anal Chem (Palo Alto Calif). 2013;6:287-303.
21. Grada A. Next-generation sequencing: methodology and application. J Invest Dermatol. 2013;133(8):1-4.
22. Bernabe R, Hickson N, Wallace A, Blackhall FH. What do we need to make circulating tumour DNA (ctDNA) a routine diagnostic test in lung cancer? Eur J Cancer. 2017;81:66-73.
23. Beck TF, Mullikin JC, Biesecker LG. Systematic evaluation of sanger validation of next-generation sequencing variants. Clin Chem. 2016;62(4):647-54.
24. Werner SL, Graf RP, Landers M, Valenta DT, Schroeder M, Greene SB, et al. Analytical validation and capabilities of the epic CTC platform: enrichment-free circulating tumour cell detection and characterization. J Circ Biomark. 2015;4:3.
25. Germer S, Higuchi R. Homogeneous allele-specific PCR in SNP genotyping. Methods Mol Biol. 2003;212:197-214.
26. Maheswaran S, Sequist LV, Nagrath S, Ulkus L, Brannigan B, Collura CV, et al. Detection of mutations in EGFR in circulating lung-cancer cells. N Engl J Med. 2008;359(4):366-77.
27. Corless CL, Harrell P, Lacouture M, Bainbridge T, Le C, Gatter K, et al. Allele-specific polymerase chain reaction for the imatinib-resistant KIT D816V and D816F mutations in mastocytosis and acute myelogenous leukemia. J Mol Diagn. 2006;8(5):604-12.
28. Jarry A, Masson D, Cassagnau E, Parois S, Laboisse C, Denis MG. Real-time allele-specific amplification for sensitive detection of the BRAF mutation V600E. Mol Cell Probes. 2004;18(5):349-52.
29. Huang T, Zhuge J, Zhang WW. Sensitive detection of BRAF V600E mutation by Amplification Refractory Mutation System (ARMS)-PCR. Biomark Res. 2013;1(1):3.
30. Tamburro M, Ripabelli G. High Resolution Melting as a rapid, reliable, accurate and cost-effective emerging tool for genotyping pathogenic bacteria and enhancing molecular epidemiological surveillance: a comprehensive review of the literature. Ann Ig. 2017;29(4):293-316.
31. Wittwer CT. High-resolution DNA melting analysis: advancements and limitations. Hum Mutat. 2009;30(6):857-9.
32. Herbst RS. Role of novel targeted therapies in the clinic. Br J Cancer. 2005;92(1):S21-S7.
33. Sidransky D. Emerging molecular markers of cancer. Nat Rev Cancer. 2002;2(3):210-9.
34. Lim KT, Tan KY. Current research and treatment for gastrointestinal stromal tumors. World J Gastroenterol. 2017;23(27):4856-66.
35. Di Rocco A, De Angelis F, Ansuinelli M, Foa R, Martelli M. Is now the time for molecular driven therapy for diffuse large B-cell lymphoma? Expert Rev Hematol. 2017;10(9):761-74.
36. Nagini S. Breast cancer: current molecular therapeutic targets and new players. Anticancer Agents Med Chem. 2017;17(2):152-63.
37. Dienstmann R, Vermeulen L, Guinney J, Kopetz S, Tejpar S, Tabernero J. Consensus molecular subtypes and the evolution of precision medicine in colorectal cancer. Nat Rev Cancer. 2017;17(2):79-92.
38. Mazzarella L, Guida A, Curigliano G. Cetuximab for treating non-small cell lung cancer. Expert Opin Biol Ther. 2018;18(4):483-93.
39. Lee YT, Tan YJ, Oon CE. Molecular targeted therapy: Treating cancer with specificity. Eur J Pharmacol. 2018;834:188-96.
40. Salles G, Barrett M, Foa R, Maurer J, O'Brien S, Valente N, et al. Rituximab in B-Cell hematologic malignancies: a review of 20 years of clinical experience. Adv Ther. 2017;34(10):2232-73.
41. Mok CC. Current role of rituximab in systemic lupus erythematosus. Int J Rheum Dis. 2015;18(2):154-63.
42. Huxley N, Crathorne L, Varley-Campbell J, Tikhonova I, Snowsill T, Briscoe S, et al. The clinical effectiveness and cost-effectiveness of cetuximab (review of technology appraisal no. 176) and panitumumab (partial review of technology appraisal no. 240) for previously untreated metastatic colorectal cancer: a systematic review and

economic evaluation. Health Technol Assess. 2017;21(38):1-294.
43. Singh D, Attri BK, Gill RK, Bariwal J. Review on EGFR inhibitors: critical updates. Mini Rev Med Chem. 2016;16(14):1134-66.
44. Kazandjian D, Blumenthal GM, Yuan W, He K, Keegan P, Pazdur R. FDA approval of gefitinib for the treatment of patients with metastatic EGFR mutation-positive non-small cell lung cancer. Clin Cancer Res. 2016;22(6):1307-12.
45. Steins M, Thomas M, Geissler M. Erlotinib. Recent Results Cancer Res. 2018;211:1-17.
46. Cohen MH, Johnson JR, Chen YF, Sridhara R, Pazdur R. FDA drug approval summary: erlotinib (Tarceva) tablets. Oncologist. 2005;10(7):461-6.
47. Keating GM. Bevacizumab: a review of its use in advanced cancer. Drugs. 2014;74(16):1891-925.
48. Rong B, Yang S, Li W, Zhang W, Ming Z. Systematic review and meta-analysis of Endostar (rh-endostatin) combined with chemotherapy versus chemotherapy alone for treating advanced non-small cell lung cancer. World J Surg Oncol. 2012;10:170.

REVIEW ARTICLE

Unfolding the Pathogenesis of Systemic Sclerosis through Epigenomics

Xiuzhi JIA[1], Hao CHENG[2 *], Ying XIAO[1 *]

[1] Central Lab of Biomedical Research Center, Sir Run Run Shaw Hospital, School of Medicine, Zhejiang University. Hangzhou, Zhejiang Province, China.
[2] Department of Dermatology, Sir Run Run Shaw Hospital, School of Medicine, Zhejiang University, Hangzhou, Zhejiang Province, China.

*Correspondence: chenghao1@zju.edu.cn; xiaoying.srr@zju.edu.cn
https://doi.org/10.37175/stemedicine.v1i1.5

ABSTRACT

As a group of autoimmune diseases, systemic sclerosis (scleroderma, SSc) is prominent in the imbalance of immune homeostasis, micro-vessels dominant obliteration, and the skin and/or internal organs fibrosis. Although the precise mechanisms are still unknown, increasing data have shown that epigenetic dysregulation, which can link genetics and environmental stress, represents a promising field in SSc investigation. The objective of this review is to sum up the current information on the epigenetic alteration in SSc, including DNA methylation, histone modification, and microRNA.

Keywords: Epigenetics · Methylation · Histone modification · microRNA · Systemic sclerosis

Introduction

Systemic sclerosis (scleroderma, SSc) was first reported by Carlo Curzio in 1753 (1), with the disease becoming well-documented by 1842 (2). As a rare connective tissue disease (ranging from 7 to 700 cases per million), SSc is characterized by vascular anomaly, chronic inflammation, and fibrosis process. Significant female bias (> 80%) (3), racial discrepancy (4), and geographic clustering (5) are observed in SSc, which suggests that environmental, genetic, and hormonal factors may contribute to the initiation and development of this disease.

The precise mechanism of how these external environmental factors, such as silica, ketones, ultraviolet light, trichloroethylene, aromatic and chlorinated solvents, white spirits, and welding fumes, can induce an autoimmune attack is still unknown. The complexity of the issue is further enhanced by the possibility that environmental factors may not only induce cellular and tissue damages associated with both innate and adaptive immunity, but also alter fibroblasts and microvascular endothelial cell phenotype or function.

Without causing alterations in the DNA sequence, epigenetics can cause heritable phenotypic changes (6, 7), which is vital in the regulation of gene expression and development. Major mechanisms of epigenetic gene regulation, such as chromatin remodeling, histone modification, DNA methylation, transcriptional regulation by non-coding RNA, and gene imprinting, can provide plausible links between environmental factors and disease predisposition and perpetuation. It is possible that epigenetics plays a vital role in the pathogenesis of SSc. It is worth noting that with the development of high throughput omics, it is testified that epigenetic mechanisms can lead to downstream effects on modulation of chromatin architecture and regulate gene transcription. As only a few epigenetic studies have been performed in SSc, the recent progress in DNA methylation, histone modification, and microRNAs are reviewed in this paper (Figure 1).

DNA methylation

Most DNA methylation occurs at the 5-position of cytosine residues in a short canonical sequence 5′-CG-3′ (CpG) enriched in promoter regions, which arises from *de novo* DNA methyltransferases (DNMTs), such as DNMT3A and DNMT3B during development. This methylation pattern could be inherited and maintained by epigenetic maintenance mediator, DNMT1, in proliferating cells (8). Hence, DNA methylation can be considered as a stable epigenetic mark that usually represses gene expression (9). Increasing investigations have indicated that DNA methylation dysregulation is involved in pathogenesis of SSc in fibroblasts, microvascular endothelial cells, and lymphocytes.

DNA methylation in fibroblasts

At a global level, BeadChip array analysis has identified 2710 differentially regulated CpG sites in SSc

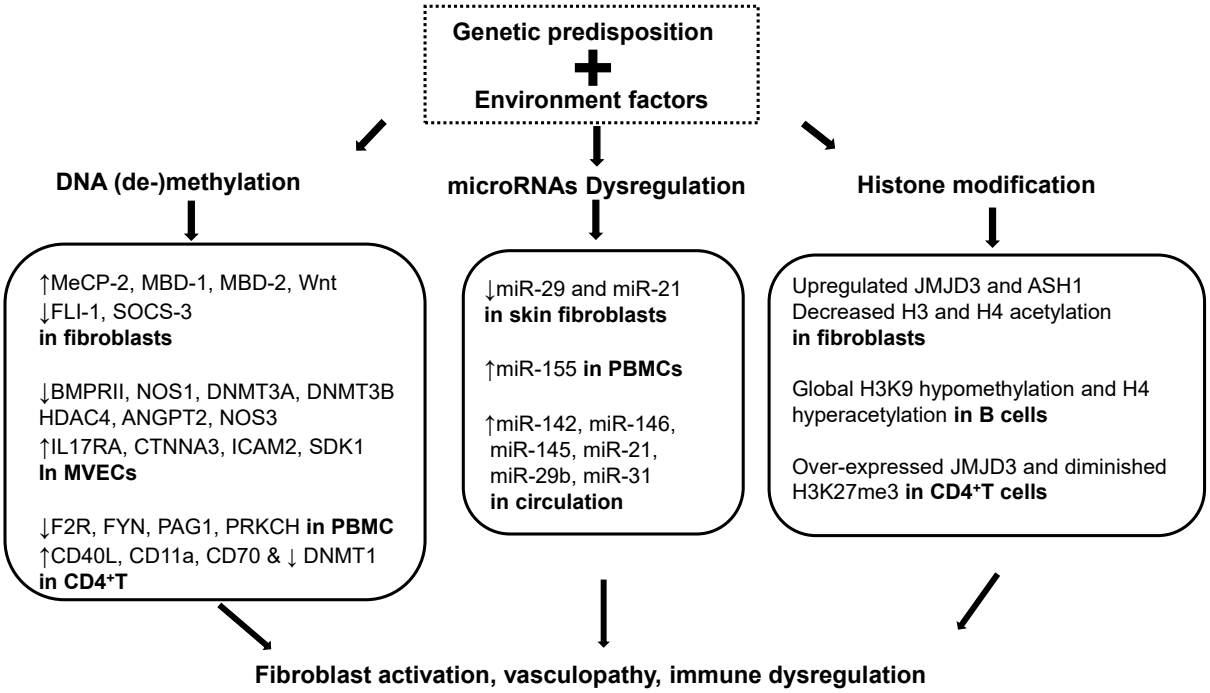

Figure 1. Possible roles of epigenetic mechanisms involved in systemic sclerosis pathogenesis. Genetic disposition and environmental factors can alter DNA (de-)methylation, histone modifications and microRNAs regulation, which can contribute to systemic sclerosis associated fibroblasts activation, vasculopathy, and immune dysregulation. Abbreviation: Methyl-CpG binding protein 2, MeCP-2; methyl-CpG DNA binding protein,MBD-1; Friend leukemia integration factor 1, FLI-1; bone morphogenic protein receptor II, BMPRII; nitric oxide synthase 1, NOS1; histone deacetylases 4, HDAC4; angiopoietin 2, ANGPT2; interleukin 17 receptor, IL-17RA; catenin alpha 3, CTNNA3; intercellular adhesion molecule 2, ICAM2; sidekick cell adhesion molecule 1, SDK1; coagulation factor II thrombin receptor, F2R; FYN proto-oncogene, Src family tyrosine kinase, FYN; phosphoprotein membrane anchor with glycosphingolipid microdomains 1, PAG1; protein kinase C eta, PRKCH; DNA (cytosine-5)-methyltransferase 1, DNMT1; 3-Deazaneplanocin A, DZNep; JMJ domain-containing protein 3 , JMJD3.

fibroblasts when compared with healthy controls. It is further demonstrated that most of the affected CpG sites (61%) are hypomethylated and associated with extracellular matrix metabolism (10). Methyl-CpG binding protein 2 (MeCP-2), methyl-CpG DNA binding protein (MBD)-1, and MBD-2 show increased expression, which can function as epigenetic maintenance mediators. All of these indicate that epigenetic inheritance is also involved in the development of SSc.

In addition to reduced acetylation of H3 and H4, several CpG islands within Friend leukemia integration factor 1 (FLI-1), a pro-fibrotic signaling cascade relevant transcription factor, are hypermethylated in both cultured primary SSc fibroblasts and skin biopsies compared with healthy control (11). Inhibition of DNMTs by 2-deoxy-5-azacytidine (5-Aza) can remove methyl groups from CpG islands of FLI-1 promoter region and reactivate the expression of FLI-1 and down-stream type I collagen production in SSc fibroblasts. In addition to the aberrant activation of fibroblasts, epigenetic silencing of FLI-1 can cause SSc relevant vascular pathogenesis.

Suppressor of cytokine signaling 3 (SOCS-3), as an anti-fibrotic mediator and endogenous inhibitor of Janus kinase 2 (JAK2), can down-regulate transforming growth factor (TGF)-β induced collagen secretion, fibroblast activation, myofibroblast differentiation, and fibrosis formation (12). SOCS-3 knockdown can activate JAK2/STAT3 signaling and induce the differentiation of fibroblasts into myofibroblasts. SOCS-3 is down-regulated in SSc fibroblasts through promotor hypermethylation, which may lead to persistent activation of fibroblasts and further fibrosis. The canonical Wnt signaling plays a central role in SSc fibrosis (13, 14). The balance lying between Wnt ligands and endogenous Wnt antagonists can regulate canonical Wnt signaling activation. In SSc, owing to overexpressed Wnt ligands and epigenetic silencing of Wnt antagonists, such as Dick-kopf1 (DKK1) and secreted frizzled-related protein-1 (SFRP1), such balance is shifted toward activation (15, 16). At the same time, 5-Aza treatment can increase DKK1 and SFRP1 expression, inhibit canonical Wnt signaling, and exert anti-fibrotic effects.

DNA methylation in microvascular endothelial cells (MVECs)

Bone morphogenic protein (BMP) can interact with bone morphogenic protein receptor II (BMPRII) to coordinate the survival, proliferation, and differentiation of SSc MVECs. A significantly decreased expression of BMPRII is observed in MVECs due to heavily methylated CpG sites in the promoter region of BMPRII after bisulfite conversion sequencing (17). The administration of 5-Aza to SSc MVECs can restore the decreased BMPRII expression and the impaired apoptotic response to oxidation injury and serum starvation. All of these indicate

that the epigenetic modulation of BMPRII signaling might have a fundamental role in the sensitivity of MVECs to apoptosis and vasculopathy.

A genome-wide MVECs (isolated from seven diffuse cutaneous SSc patients) DNA methylation assay has identified 1,625 hypermethylated CpG sites (910 genes) and 830 hypomethylated CpG sites (485 genes), which show a significant negative correlation between gene expression and DNA methylation status. Among them, nitric oxide synthase 1 (NOS1), DNMT3A, DNMT3B, histone deacetylase 4 (HDAC4), and angiopoietin 2 (ANGPT2) are the common hypermethylated genes, while interleukin (IL)-17RA, catenin alpha 3 (CTNNA3), intercellular adhesion molecule 2 (ICAM2), and sidekick cell adhesion molecule 1 (SDK1) are the common hypomethylated genes. Of note, high methylation in the NOS3 promoter region can lead to reduced NOS3 expression in SSc MVECs, which can be reversed by the administration of 5-Aza (18).

DNA methylation in peripheral blood mononuclear cells (PBMCs)

Genome-wide DNA methylation and transcriptome integration analysis with a machine learning algorithm have identified six methylation-regulated differentially expressed genes in PBMCs of SSc, which can distinguish SSc from healthy control with 100% accuracy. Among these six genes, Coagulation Factor II Thrombin Receptor (F2R), FYN Proto-Oncogene, Src Family Tyrosine Kinase (FYN), Phosphoprotein Membrane Anchor With Glycosphingolipid Microdomains 1 (PAG1), and Protein Kinase C Eta (PRKCH) are differentially expressed in SSc with interstitial lung disease compared to SSc without interstitial lung disease (19). The whole blood DNA methylation integrated analysis in discordant twins reveals that diffused cutaneous SSc-associated CpGs are enriched at the encyclopedia of DNA elements, roadmap, and blueprint-derived regulatory regions, which indicates a potential role in the initiation of this disease. Notably, the dominant enriched regions in macrophages and monocytes can act on fibrosis, indicating that the dysregulated cellular function can be related to altered epigenetic mechanisms in diffuse cutaneous SSc (20).

In SSc $CD4^+$T cells, global hypomethylation can be attributed to the significantly decreased DNMT1 expression, which may alter the reactivation of endoparasitic sequences and lead to autoimmunity. It is intriguing to find the methylation divergence between fibroblasts and MVECs (increased methylation) and $CD4^+$T cells (decreased methylation). Although further investigation is required to understand the detailed mechanisms, it is reported that extracellular signal-regulated kinase (ERK) defect may regulate T cell DNA methylation in arthritis and lupus (21). Such a mechanism may also function in SSc $CD4^+$T cells.

Demethylation can be observed in the promoter of CD40L on the inactive X chromosome derived from female SSc $CD4^+$T cells, which indicates impaired DNA methylation maintenance and reactivation of the normally silenced X chromosome (22). Of note, CD40L expression is up-regulated in SSc fibroblasts obtained from affected $CD4^+$T cells and skin, especially in female SSc patients (23, 24). CD40L is testified to take part in fibrosis, adhesion of endothelial cells, and B cell activation. Such gender-biased epigenetic alteration can explain the female tendency in SSc.

Co-stimulation is fundamental to develop an optimized immune response. Demethylation of CD11a and CD70 promoter regions contributed to CD11a and CD70 overexpression in $CD4^+$T cells, which may also be involved in the development of SSc (25, 26). Furthermore, knockdown of SOCS-3 in T cells in the donor graft exacerbates sclerodermatous graft versus host disease (27, 28). All of these indicate that DNA methylation alteration can induce the development of SSc.

Histone modifications

As the essential component of the nucleosome, histones can be classified into four types (H2A, H2B, H3, and H4), which are known to be modified by acetylation and methylation to regulate chromatin architecture. Histone acetylation usually leads to transcriptional activation, while the inhibition or activation effect of histone methylation mainly depends on the position of lysine methylation. For example, H3K27 tri-methylation (H3K27me3) could decrease the relevant gene expression, while histone H3 lysine 4 (H3K4) methylation can increase the associated gene expression (29). It is interesting to find that DNA methylation can lead to methyl binding domain (MBD) and further HDAC recruitment, which indicates the mechanical linkage of DNA methylation and histone modifications.

Treatment with trichostatin (TSA), an HDAC inhibitor available for the myelodysplastic disease, can attenuate the expression and accumulation of collagen I, extracellular matrix, and fibronectin in SSc fibroblast-induced skin fibrosis (11, 30, 31). Similarly, TSA administration can increase H3 and H4 acetylation on the NOS3 promoter region accompanied by up-regulated NOS expression in SSc MVECs (32).

The pro-fibrotic transcription effects of 3-Deazaneplanocin A (DZNep, C-c3Ado), an inhibitor of histone methyltransferase enhancer of Zeste homolog 2 (EZH2), might result from its stimulation on Fos-related Antigen 2 (Fra2) to foster the release of tissue inhibitor of metalloproteinases (TIMP) and the promotion of fibroblast-to-myofibroblast differentiation (33). Fra2 transgenic mice would spontaneously develop skin and lung fibrosis, vascular smooth muscle proliferation, and pulmonary arteries obliteration. In line with these results, increased expression of Fra2 can be detected in skin-infiltrating macrophages and perivascular regions of SSc patients (34).

Significantly decreased H3 and H4 acetylation and increased H3K27me3 are detected on the Fli-1 promoter region of SSc fibroblasts, which could result in the inhibition of Fli-1. It is also demonstrated that H3K27me3 inhibition could stimulate collagen release in

SSc fibroblasts (27, 35). Although H3K27me3 is considered stable, ubiquitously transcribed tetratricopeptide repeat on chromosome X (UTX) and JMJ domain-containing protein 3 (JMJD3) have recently been testified to have potent H3K27 demethylase activity (36, 37). A TGF-β dependent JMJD3 upregulation and associated H3K27me3 de-methylation might exert pro-fibrotic functions in SSc. As a histone methyltransferase, absent, small or homeotic disc 1 (ASH1) can mediate H3K4 methylation and regulate COL1A1 (pro-fibrotic gene) and TGF-β associated gene expression in hepatic fibrosis. Up-regulated ASH1 is observed in SSc fibroblasts, which indicates ASH1 may mediate the pathogenesis of SSc (29).

Global histone H3K9 hypomethylation and global histone H4 hyperacetylation are observed in SSc B cells compared with healthy control, which correlates with skin thickness and disease activity (38). Relatively low levels of H3K27me3 can be observed in the $CD4^+$T cells of SSc patients when compared with healthy control. JMJD3 is over-expressed in $CD4^+$T cells of SSc patients, accompanied by lower levels of H3K27me3. All of these indicate that JMJD3 may be vital to decipher the mechanism related to histone modifications (39). Altered chromatin marks in SSc monocytes can be enriched with antiviral pathways, interferon, and immune system, and present with recurrent binding sites for interferon regulatory factor (IRF)-1 and signal transducer and activator of transcription (STAT)-1, which is correlated with their interferon signature.

microRNA (miRNA, miR)

As a small (about 22 nucleotides) non-coding RNA molecule, tissue-specific or cell intrinsic miRNA can function in RNA silencing and gene post-transcriptional regulation (40-42).

miR-29 is the first miRNA detected in the skin fibroblasts derived from SSc patients, whose down-regulation contributes to the pathogenesis of SSc. Irritation of fibroblasts derived from normal skin with pro-fibrotic molecules, such as platelet-derived growth factor (PDGF) and TGF-β, can decrease miR-29 secretion; while the restoration of miR-29 can reduce collagen release (43). TGF-β can up-regulate miR-21 expression in SSc fibroblasts (44). The over-expression of miR-21 can decrease SMAD Family Member 7 (Smad-7) expression, while miR-21 knockdown can increase Smad-7 expression (45), which indicates that miR-21 can exert a pro-fibrogenic effect by negatively regulating Smad-7.

Nine pro-fibrotic miRNAs are upregulated, while 14 anti-fibrotic miRNAs are down-regulated within exosomes isolated from the serum of diffuse cutaneous SSc patients (Table 1). The dose-dependent paracrine pro-fibrotic effects of such miRNAs are also confirmed when cultured with normal human dermal fibroblasts to alter the pro-fibrotic gene expression and increase type I collagen production (46). It is worth noting that miR-92a level in serum is higher in SSc patients when compared with healthy control, and correlates with telangiectasia severity, but not with SSc activity (47). On the other hand, circulating miR-142, miR-146, miR-145, miR-21, miR-29b, and miR-31 do correlate with the severity of SSc (48-51). Moreover, miR-29a can directly down-regulate mRNA and protein expression of type I and type III collagen. miR-155 expression in PBMC strongly correlates with lung function tests in SSc-associated interstitial lung disorder, and miR-155 knock-out mice develop milder lung fibrosis and survive longer (52). All of these indicate that some miRNAs, especially exosome derived, can be expected to serve as prognostic and diagnostic markers for precision medicine (53).

It is noteworthy that histone deacetylation and methylation also take part in the regulation of miRNA transcription (54). Such interactions should be regarded in the treatment of SSc with epigenetic modulators, whose effects are considered as the diffuse and unknown off-site effect. Exosomes can be utilized as cargos to transduce the inter-cellular information associated with epigenetic alteration, such as DNA methylation, histone modification, miRNA, and long intergenic non-coding RNA (LincRNA) (55-58), to reflect the status of donor cells and imprint recipient cells (53, 59). Although further refinements to exosome-based drug delivery systems are needed to meet the clinical scale, elaborate design can ensure direct and specific target, which will contribute to limit the diffuse effect of epigenetic modulators.

Conclusions

Epigenetics can imprint short-term signals or stress into longer-lasting, more stable, and inherited phenotypic

Table 1. Exosomes derived microRNA for SSc.

Detected microRNAs	Function implication
9 upregulated exosomes-derived miRNAs (miR-21-5p, miR-503-5p, miR-155-5p, miR-29a-3p, miR-17-5p, miR-let-7g-5p, miR-23b-5p, miR-150-5p, and miR-215-5p)	Profibrotic function
14 downregulated exosomes-derived miRNAs (miR-200a-3p, miR-140-5p, miR-92a-3p, miR-29b-3p, miR-223-3p, miR-26b-5p, miR-196a-5p, miR-145-5p, miR-200b-3p, miR-let-7a-5p, miR-125b-5p, miR-133a-3p, miR-146a-5p, and miR-129-5p)	Anti-fibrotic function

Note: The dysregulation of microRNAs derived from exosomes isolated from the serum of diffuse cutaneous systemic sclerosis (scleroderma, SSc) patients, which has been reported by Wermuth PJ. et al (46).

changes. Thus, epigenetic treatment strategies may be able to treat or even reverse tissue fibrosis through rescuing the imprinted genes. Exosome-based epigenetic modulator delivery maybe a new direction in SSc clinical practice.

Acknowledgements
Thank Chen Rui and Hao Zhang for their kindly help in the manuscript preparation process.

Conflict of interest
The authors declare that there are no conflicts of interest.

Funding body
This project is supported by the scientific research start-up funds for specially engaged employees of Sir Run Run Shaw Hospital (Ytp1902) and fund of the National Nature Science Foundation of China (81660708, 31900620).

References

1. Rose NR, Mackay IR. CHAPTER 1 - The immune response in autoimmunity and autoimmune disease. In: Rose NR, Mackay IR, editors. The Autoimmune Diseases II. Boston: Academic Press; 1992. p. 1-26.
2. Firestein GS, Kelley WN. Kelley's textbook of rheumatology. Philadelphia, PA: Elsevier/Saunders; 2013.
3. Gourier G, Therene C, Mazeas M, Abasq-Thomas C, Brenaut E, Huet F, et al. Clinical characteristics of pruritus in systemic sclerosis vary according to the autoimmune subtype. Acta Derm Venereol. 2018;98(8):735-41.
4. Mayes MD. Scleroderma epidemiology. Rheum Dis Clin North Am. 2003;29(2):239-54.
5. Valesini G, Litta A, Bonavita MS, Luan FL, Purpura M, Mariani M, Balsano F. Geographical clustering of scleroderma in a rural area in the province of Rome. Clin Exp Rheumatol. 1993;11(1):41-7.
6. Sen D, Keung AJ. Designing epigenome editors: considerations of biochemical and locus specificities. In: Jeltsch A, Rots MG, editors. Epigenome Editing: Methods and Protocols. New York, NY: Springer New York; 2018. p. 65-87.
7. Dupont C, Armant DR, Brenner CA. Epigenetics: definition, mechanisms and clinical perspective. Semin Reprod Med. 2009;27(5):351-7.
8. Richardson B. Primer: epigenetics of autoimmunity. Nat Clin Pract Rheumatol. 2007;3(9):521-7.
9. Du J, Johnson LM, Jacobsen SE, Patel DJ. DNA methylation pathways and their crosstalk with histone methylation. Nat Rev Mol Cell Biol. 2015;16(9):519-32.
10. Altorok N, Tsou P-S, Coit P, Khanna D, Sawalha AH. Genome-wide DNA methylation analysis in dermal fibroblasts from patients with diffuse and limited systemic sclerosis reveals common and subset-specific DNA methylation aberrancies. Ann Rheum Dis. 2015;74(8):1612-20.
11. Wang Y, Fan P-S, Kahaleh B. Association between enhanced type I collagen expression and epigenetic repression of the FLI1 gene in scleroderma fibroblasts. Arthritis Rheum. 2006;54(7):2271-9.
12. Dees C, Tomcik M, Palumbo-Zerr K, Distler A, Beyer C, Lang V, et al. JAK-2 as a novel mediator of the profibrotic effects of transforming growth factor beta in systemic sclerosis. Arthritis Rheum. 2012;64(9):3006-15.
13. Bergmann C, Distler JHW. Canonical Wnt signaling in systemic sclerosis. Lab Invest. 2016;96(2):151-5.
14. Henderson WR, Jr., Chi EY, Ye X, Nguyen C, Tien Y-t, Zhou B, et al. Inhibition of Wnt/beta-catenin/CREB binding protein (CBP) signaling reverses pulmonary fibrosis. Proc Natl Acad Sci USA. 2010;107(32):14309-14.
15. Svegliati S, Marrone G, Pezone A, Spadoni T, Grieco A, Moroncini G, et al. Oxidative DNA damage induces the ATM-mediated transcriptional suppression of the Wnt inhibitor WIF-1 in systemic sclerosis and fibrosis. Sci Signal. 2014;7:ra84-ra.
16. Dees C, Schlottmann I, Funke R, Distler A, Palumbo-Zerr K, Zerr P, et al. The Wnt antagonists DKK1 and SFRP1 are downregulated by promoter hypermethylation in systemic sclerosis. Ann Rheum Dis. 2014;73:1232-9.
17. Wang Y, Kahaleh B. Epigenetic repression of bone morphogenetic protein receptor II expression in scleroderma. J Cell Mol Med. 2013;17(10):1291-9.
18. Romero L, Zhang D, Cooke J, Ho HK, Avalos E, Herrera R, et al. Differential expression of nitric oxide by dermal microvascular endothelial cells from patients with scleroderma. Vasc Med. 2000;5:147-58.
19. Zhu H, Zhu C, Mi W, Chen T, Zhao H, Zuo X, et al. Integration of genome-wide DNA methylation and transcription uncovered aberrant methylation-regulated genes and pathways in the peripheral blood mononuclear cells of systemic sclerosis. Int J Rheumatol. 2018;2018:7342472-.
20. Ramos PS, Zimmerman KD, Haddad S, Langefeld CD, Medsger TA, Jr., Feghali-Bostwick CA. Integrative analysis of DNA methylation in discordant twins unveils distinct architectures of systemic sclerosis subsets. Clin Epigenetics. 2019;11(1):58-.
21. Sawalha AH, Jeffries M, Webb R, Lu Q, Gorelik G, Ray D, et al. Defective T-cell ERK signaling induces interferon-regulated gene expression and overexpression of methylation-sensitive genes similar to lupus patients. Genes & Immun. 2008;9(4):368-78.
22. Hellman A, Chess A. Gene body-specific methylation on the active X chromosome. Science. 2007;315:1141-3.
23. Lian X, Xiao R, Hu X, Kanekura T, Jiang H, Li Y, et al. DNA demethylation of CD40L in CD4+ T cells from women with systemic sclerosis: A possible explanation for female susceptibility. Arthritis Rheum. 2012;64(7):2338-45.
24. Fukasawa C, Kawaguchi Y, Harigai M, Sugiura T, Takagi K, Kawamoto M, et al. Increased CD40 expression in skin fibroblasts from patients with systemic sclerosis (SSc): role of CD40-CD154 in the phenotype of SSc fibroblasts. Eur J Immunol. 2003;33(10):2792-800.
25. Lu Q, Kaplan M, Ray D, Ray D, Zacharek S, Gutsch D, et al. Demethylation of ITGAL (CD11a) regulatory sequences in systemic lupus erythematosus. Arthritis Rheum. 2002;46(5):1282-91.
26. Jiang H, Xiao R, Lian X, Kanekura T, Luo Y, Yin Y, et al. Demethylation of TNFSF7 contributes to CD70 overexpression in CD4+ T cells from patients with systemic sclerosis. Clin Immunol. 2012;143(1):39-44.
27. Yin Y, Liu W, Dai Y. SOCS3 and its role in associated diseases. Human Immunology. 2015;76(10):775-80.
28. Hill GR, Kuns RD, Raffelt NC, Don ALJ, Olver SD, Markey KA, et al. SOCS3 regulates graft-versus-host disease. Blood. 2010;116(2):287-96.
29. Kondo Y, Shen L, Cheng AS, Ahmed S, Boumber Y, Charo C, et al. Gene silencing in cancer by histone H3 lysine 27 trimethylation independent of promoter DNA methylation. Nat Genet. 2008;40(6):741-50.
30. Hemmatazad H, Rodrigues HM, Maurer B, Brentano F, Pileckyte M, Distler JHW, et al. Histone deacetylase 7, a potential target for the antifibrotic treatment of systemic sclerosis. Arthritis Rheum. 2009;60(5):1519-29.
31. Huber LC, Distler JHW, Moritz F, Hemmatazad H, Hauser T, Michel BA, et al. Trichostatin A prevents the accumulation of extracellular matrix in a mouse model of bleomycin-induced skin fibrosis. Arthritis Rheum. 2007;56(8):2755-64.
32. Matouk CC, Marsden PA. Epigenetic regulation of vascular endothelial gene expression. Circ Res. 2008;102(8):873-87.
33. Ciechomska M, O'Reilly S, Przyborski S, Oakley F, Bogunia-Kubik K, van Laar JM. Histone demethylation and Toll-like receptor 8-dependent cross-talk in monocytes promotes transdifferentiation of fibroblasts in systemic sclerosis via Fra-2.

Arthritis Rheum. 2016;68(6):1493-504.
34. Maurer B, Distler JHW, Distler O. The Fra-2 transgenic mouse model of systemic sclerosis. Vascul Pharmacol. 2013;58(3):194-201.
35. Krämer M, Dees C, Huang J, Schlottmann I, Palumbo-Zerr K, Zerr P, et al. Inhibition of H3K27 histone trimethylation activates fibroblasts and induces fibrosis. Ann Rheum Dis. 2013;72:614-20.
36. Hong S, Cho Y-W, Yu L-R, Yu H, Veenstra TD, Ge K. Identification of JmjC domain-containing UTX and JMJD3 as histone H3 lysine 27 demethylases. Proc Natl Acad Sci USA. 2007;104(47):18439-44.
37. Agger K, Cloos PAC, Christensen J, Pasini D, Rose S, Rappsilber J, et al. UTX and JMJD3 are histone H3K27 demethylases involved in HOX gene regulation and development. Nature. 2007;449(7163):731-4.
38. Wang Y, Yang Y, Luo Y, Yin Y, Wang Q, Li Y, et al. Aberrant histone modification in peripheral blood B cells from patients with systemic sclerosis. Clin Immunol. 2013;149(1):46-54.
39. Wang Q, Xiao Y, Shi Y, Luo Y, Li Y, Zhao M, et al. Overexpression of JMJD3 may contribute to demethylation of H3K27me3 in CD4+ T cells from patients with systemic sclerosis. Clin Immunol. 2015;161(2):396-9.
40. Ambros V. The functions of animal microRNAs. Nature. 2004;431(7006):350-5.
41. Bartel DP. Metazoan MicroRNAs. Cell. 2018;173(1):20-51.
42. Bartel DP. MicroRNAs: Genomics, Biogenesis, Mechanism, and Function. Cell. 2004;116(2):281-97.
43. Maurer B, Stanczyk J, Jüngel A, Akhmetshina A, Trenkmann M, Brock M, et al. MicroRNA-29, a key regulator of collagen expression in systemic sclerosis. Arthritis Rheum. 2010;62(6):1733-43.
44. Zhu H, Li Y, Qu S, Luo H, Zhou Y, Wang Y, et al. MicroRNA expression abnormalities in limited cutaneous scleroderma and diffuse cutaneous scleroderma. J Clin Immunol. 2012;32(3):514-22.
45. Zhu H, Luo H, Li Y, Zhou Y, Jiang Y, Chai J, et al. MicroRNA-21 in scleroderma fibrosis and its function in TGF-β-regulated fibrosis-related genes expression. J Clin Immunol. 2013;33(6):1100-9.
46. Wermuth PJ, Piera-Velazquez S, Jimenez SA. Exosomes isolated from serum of systemic sclerosis patients display alterations in their content of profibrotic and antifibrotic microRNA and induce a profibrotic phenotype in cultured normal dermal fibroblasts. Clin Exp Rheumatol. 2017;35 Suppl 106(4):21-30.
47. Sing T, Jinnin M, Yamane K, Honda N, Makino K, Kajihara I, et al. microRNA-92a expression in the sera and dermal fibroblasts increases in patients with scleroderma. Rheumatology. 2012;51(9):1550-6.
48. Honda N, Jinnin M, Kajihara I, Makino T, Makino K, Masuguchi S, et al. TGF-β–mediated downregulation of microRNA-196a contributes to the constitutive upregulated type I collagen expression in scleroderma dermal fibroblasts. J Immunol. 2012;188:3323-31.
49. Honda N, Jinnin M, Kira-Etoh T, Makino K, Kajihara I, Makino T, et al. miR-150 down-regulation contributes to the constitutive type I collagen overexpression in scleroderma dermal fibroblasts via the induction of integrin β3. Am J Pathol. 2013;182(1):206-16.
50. Jiang X, Tsitsiou E, Herrick SE, Lindsay MA. MicroRNAs and the regulation of fibrosis. FEBS J. 2010;277(9):2015-21.
51. Makino K, Jinnin M, Kajihara I, Honda N, Sakai K, Masuguchi S, et al. Circulating miR-142-3p levels in patients with systemic sclerosis. Clin Exp Dermatol. 2012;37(1):34-9.
52. Christmann RB, Wooten A, Sampaio-Barros P, Borges CL, Carvalho CRR, Kairalla RA, et al. miR-155 in the progression of lung fibrosis in systemic sclerosis. Arthritis Res Ther. 2016;18(1):155-.
53. Wermuth PJ, Piera-Velazquez S, Rosenbloom J, Jimenez SA. Existing and novel biomarkers for precision medicine in systemic sclerosis. Nat Rev Rheumatol. 2018;14(7):421-32.
54. Vrba L, Garbe JC, Stampfer MR, Futscher BW. Epigenetic regulation of normal human mammary cell type-specific miRNAs. Genome Res. 2011;21(12):2026-37.
55. Messemaker TC, Chadli L, Cai G, Goelela VS, Boonstra M, Dorjée AL, et al. Antisense long non-coding RNAs are deregulated in skin tissue of patients with systemic sclerosis. J Invest Dermatol. 2018;138(4):826-35.
56. Wang Z, Jinnin M, Nakamura K, Harada M, Kudo H, Nakayama W, et al. Long non-coding RNA TSIX is upregulated in scleroderma dermal fibroblasts and controls collagen mRNA stabilization. Exp Dermatol. 2016;25(2):131-6.
57. Xu F, Jin L, Jin Y, Nie Z, Zheng H. Long noncoding RNAs in autoimmune diseases. J Biomed Mater Res A. 2019;107(2):468-75.
58. Wu G-C, Pan H-F, Leng R-X, Wang D-G, Li X-P, Li X-M, et al. Emerging role of long noncoding RNAs in autoimmune diseases. Autoimmun Rev. 2015;14(9):798-805.
59. Colletti M, Galardi A, De Santis M, Guidelli GM, Di Giannatale A, Di Luigi L, et al. Exosomes in systemic sclerosis: messengers between immune, vascular and fibrotic components? Int J Mol Sci. 2019;20(18):4337.

REVIEW ARTICLE

Structure and function of subcortical periodic cytoskeleton throughout the nervous system

Cenfeng CHU, Guisheng ZHONG, Hui LI *

iHuman Institute, ShanghaiTech University, Shanghai, P.R. China

*Correspondence: lihui@shanghaitech.edu.cn
https://doi.org/10.37175/stemedicine.v1i1.9

ABSTRACT

The cytoskeleton plays an essential role in various functions of different cell types and is involved in the pathogenesis of several neural diseases. With the development of super-resolution fluorescence imaging technologies, which combine the molecular specificity and simple sample preparation of fluorescence microscopy with a spatial resolution comparable to that of electron microscopy, numerous new features have been revealed in the organization of the subcortical cytoskeleton. A novel periodic lattice cytoskeleton is prevalent in different cell types throughout the nervous system. Here, we review the current studies of the molecular distribution, developmental mechanisms, and functional properties of this periodic cytoskeleton structure.

Keywords: Cytoskeleton · Super-resolution microscopy · Nervous system · Spectrin · Actin

Introduction

The formation of complex nervous systems depends on cytoskeleton-based structural organizations and their dynamic remodeling, which plays a crucial role in the development, migration, and differentiation of neurons. Typical neurons possess axons and dendrites, two types of neurites (processes extending from one neuron to another) with different structures and functions. Axons are typically single long and thin neurites that transmit signals to other neurons. Dendrites are relatively short and thick, and are composed of multiple processes and spines that receive electrical and chemical signals from other neurons' axons. The formation and maturation of these distinct cellular compartments are crucial for the morphology and function of the nervous system. In neurons, tight regulation of cytoskeleton organization and remodeling has emerged as a key element in polarization, axon growth, maturation and degeneration (1).

Recently, using super-resolution imaging techniques, a novel periodic distribution of cytoskeletal elements has been observed in neurons. Actin and associated proteins form a lattice structure with a periodicity of ~180 to 190 nm in axons (2-5). This lattice structure has been observed throughout the nervous system and in many types of cells, including both neurons and oligodendrocytes (4-7). The periodic cytoskeletal structure is disrupted at presynaptic sites, and interestingly, the periodic pattern is observed in some dendrite spine necks (7, 8). These new findings provide us a better understanding of the structure and function of cytoskeleton in neurons and other types of cells. In this review, we aim to provide an overall insight into the current understanding on the structure and function of the subcortical periodic cytoskeleton organization.

I. Periodic cytoskeleton structures of neurons

The cortical cytoskeleton was first described in red blood cells using electron microscopy (EM) technique. A lattice of repeating hexagons and pentagons, arranged in a two-dimensional plane, has been observed in the cytoskeleton underneath the cell membranes (9-11). This cytoskeleton structure is composed of spectrin dimers that are formed by α- and β-spectrin subunits. Spectrin heterodimers are associated head-to-head to form tetramers, and are linked by short actin filaments of 40 nm to generate a hexagonal shaped cytoskeleton (12, 13). Several proteins, including ankyrins, adducin and tropomyosin, participate in the assembly and maintenance of the actin-spectrin cytoskeleton in red blood cells (14-16).

Like red blood cells, neurons maintain their basic structure with the help of an internal cytoskeleton. Since EM can obtain structural information with nanometer resolution, it is a key tool in discovering cytoskeleton

organization, especially the structure of polymorphic actin in neurons. Recently, using platinum replica electron microscopy, more details of delicately organized actin structures at dendrite spines and axon initial segment (AIS) have been revealed (17, 18). However, harsh conditions like detergent extraction during the labor-intensive sample preparation procedures may disrupt the fragile actin network.

With the development of super-resolution fluorescent microscopy, many novel features of subcortical cytoskeleton structures have been revealed. Xu and his colleagues recently used stochastic optical reconstruction microscopy (STORM) and discovered that actin, and its related molecules, form a periodic structure in axons (3). In addition, a similar structure with a similar period was also observed in some dendrites (2). Along neuronal axon shafts, short actin filaments, spectrin, and adducin form a highly regular lattice with a periodicity of 180 nm to 190 nm (**Figure 1A-B**). Furthermore, using stimulated emission depletion (STED) nanoscopy, these periodic cytoskeleton structures have been confirmed in the axons and dendrites of living neurons (4, 5, 8). The periodic spectrin distribution in *Drosophila* and *C. elegans* neurons was also found by another super-resolution fluorescence imaging technology, termed structured-illumination microscopy (SIM) (7). Indeed, the very first study of periodic subcortical cytoskeleton structure in the nervous system was suggested by the observation of ankyrin2 in presynaptic nerve terminal at the neuromuscular junction of *Drosophila*, observed with SIM (19). These periodic structures in the subcortical cytoskeleton, observed by various super-resolution imaging techniques, indicate that they truly exist and are unlikely to be artifacts of one particular method.

Initial studies show that the periodic pattern of cytoskeleton predominantly exists in hippocampal or

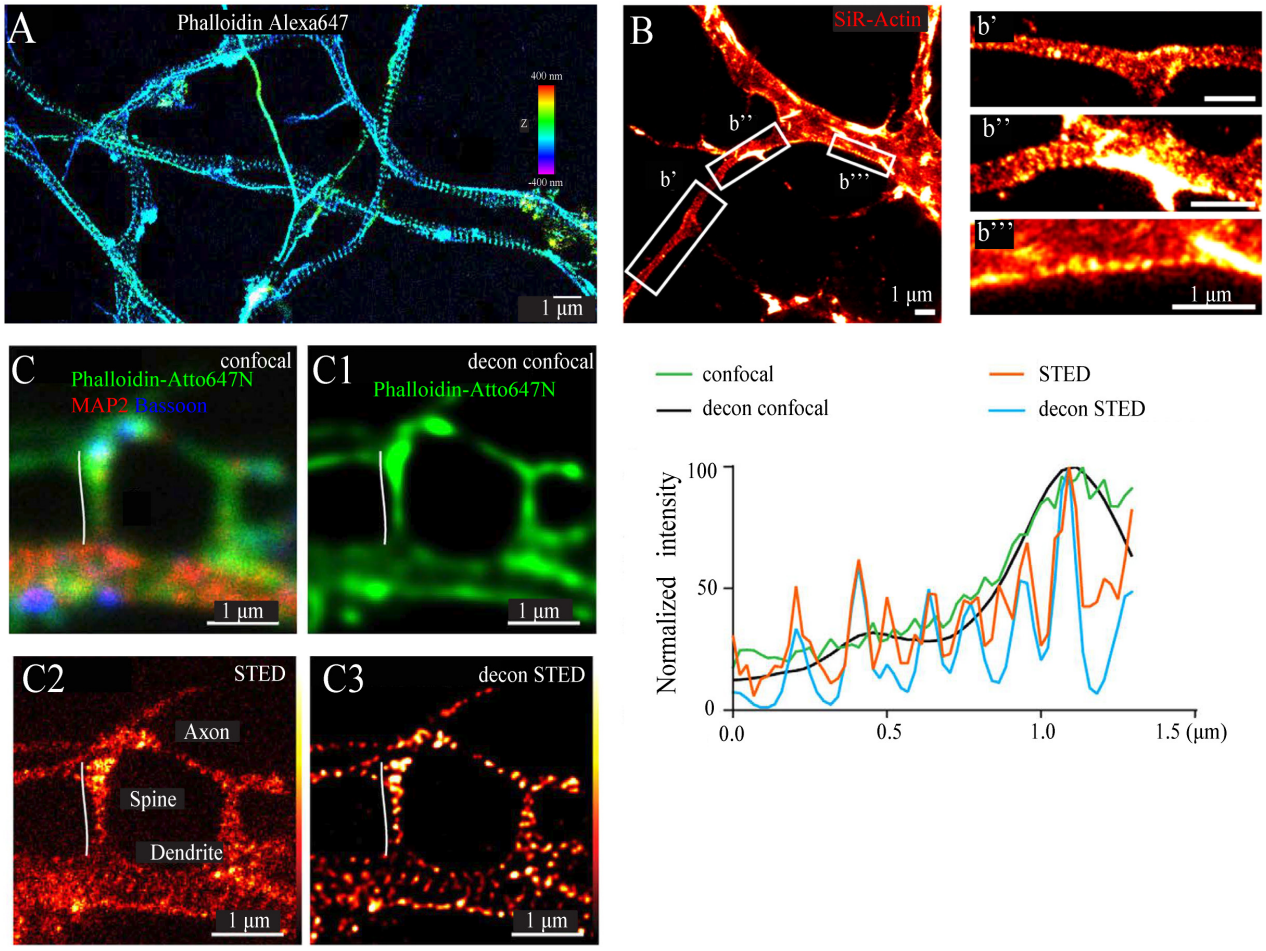

Figure 1. Cytoskeleton structures in the nervous system. (A) 3D STORM image showing periodic organization of actin filaments stained with Phalloidin-Alexa 647 in neurons. A is adapted from Zhong et al., 2014 (2). (B) STED image shows actin pattern in a living oligodendrocyte stained with SiR-Actin. c', c''and c''' are the enlarged figures indicated in C showing the periodic actin structures in dendritic-like processes. B is adapted from D'Este et al., 2016 (6). (C and C1) Conventional images show a dendrite with spines, stained with Phalloidin-Atto647N (green), dendritic marker MAP2 (red), and pre-synaptic marker Bassoon (blue). (C2) STED and (C3) deconvolution STED image shows periodic distribution of actin filaments in dendrite shafts as well as in dendrite spines. C is adapted from Bär et al., 2016 (56). In right panel, normalized line profiles of phalloidin-Atto647N intensity along the spine necks indicated in (C-C3) for raw and deconvolved confocal and STED images.

tcortical neurons (2-5). For a comprehensive understanding of this periodic cytoskeleton, it is important to address whether this periodic structure is a common feature in the nervous system. Here, four related questions should be asked carefully: 1) Do the inhibitory neurons form such a similar periodic lattice structure? 2) Do neurons in the peripheral nervous system develop a periodic actin-spectrin structure? 3) Do structurally and functionally specialized compartments in neurons form the periodic cytoskeleton structure? 4) Do glial cells have the ability to develop the periodic cytoskeleton structure? Multiple lines of evidences show that this periodic lattice cytoskeleton structure is formed in different types of cells throughout the central nervous system and peripheral nervous system, including excitatory and inhibitory neurons from various brain regions, as well as striatal neurons, granule cells, dopaminergic neurons, olfactory neurons, bipolar cells of the retina, peripheral motor neurons and dorsal root ganglia neurons (6, 7). In addition, the periodic cytoskeleton pattern is formed in different locations of neuronal axons, like the actin ring at the internodes of sciatic nerve fiber underneath of the myelin sheath, and the periodicity of ankyrin-G at AIS or the nodes of Ranvier (3, 5, 6). **Table 1** shows a summary of periodic cytoskeleton structures in different neuron cell types at different developmental stages (Table 1).

The expression of spectrin in glial cells raises the question whether the periodic lattice cytoskeleton structure is present in these cells. Studies show that the periodic structure is rarely observed in the majority of glia cells, including astrocytes and microglia (6, 7). In differentiating oligodendrocytes, the ring-like structure of actin, and, intriguingly, actin filaments, develop a periodic feature with a length of approximately 190 nm. Further, the βII spectrin is periodic and alternates with the actin ring structure. This observation was similar to the findings

Table 1: the summary of periodic cytoskeleton structure in the different neuron cell types.

Species	Neuron cell type	Region	Cytoskeleton proteins	Ref.
mouse or rat	hippocampal neuron	axon		Xu et al., 2013, Zhong et al., 2014
		dendrites		
		AIS		
	cortical neurons		actin	D'Este et al., 2016b, He et al., 2016
	HPN dendrites		actin	
	HPN axons Phall		actin	
	HPN axons		actin	
	striatal neurons		actin	
	granule cells		actin, betaII spectrin	
	bipolar cells of retina	axon	actin, betaII spectrin	
		dendrites	actin, betaII spectrin	
	DRG neurons		actin (DIV2), betaII spectrin (DIV6)	
	sciatic nerves	axon	actin	
	sciatic nerve	node of Ranvier	actin, ankyrinG	
	oligodendrocytes		actin (DIV5), betaII spectrin (DIV6)	
	dopaminergic neurons		betaII spectrin	
	olfactory neurons		betaII spectrin	
	peripheral motor neurons			
	parvalbumin neuron	cortex	betaII spectrin	
		midbrain		
		hippocampus		
	golgi cell		betaII spectrin	
	purkinje cell		betaII spectrin	
	mES motor neuron	axon	betaII spectrin	
chicken	neuron		betaII spectrin	
C. elegans	neuron		beta spectrin	
Drosophila	neuron		beta spectrin	

in neurons, though the periodicity in neurons is much less regular (6). Thus, the periodic lattice cytoskeleton structure is likely prevalent in the nervous system (**Figure 1**). How a periodic structure formed in development is an interesting question worthy of further study.

II. Developmental mechanism of the periodic cytoskeleton structure in neurons

The 180 - 190 nm spaced actin ring structures expand along the neurites. The existence of this periodic structure raises two interesting questions. First, why are actin filaments spaced so regularly, with a periodicity of approximately 190 nm? One straightforward possibility is that these short actin filaments are physically connected by a ladder-like protein, which should be stably formed and have a length around 190 nm. Second, why are the actin filaments so short, and why do they wrap around neurites? To study this, we need to find molecules which can cap the actin filaments and regulate their length, and also find the mechanism responsible for these actin filaments wrapping around axons.

Spectrin molecules are the most likely candidate to connect the actin filaments in neurons, because βII spectrin molecules are periodic with the same length as actin filaments in neurons, and also alternate with the actin rings. After using the shRNA strategy to knock down spectrin expression, the periodic pattern of actin is disrupted, implying the periodicity of actin filaments relies on the normal expression of spectrin (3). Adducin might be the candidate to control the length of actin filaments since it forms periodic, ladder-like structures in axons with a similar periodic pattern compared to the actin and spectrin structures (2), and knocking out adducin in mice can lead to enlarged neuronal actin rings and axon diameters (20).

How does the periodic cytoskeleton structure develop in neurons? At earlier developmental stages, the periodic pattern of βII spectrin could first be detected in the proximal region of axon near the cell body in neurons at 2 days *in vitro* (DIV), when normally one neurite fast outgrows other processes and becomes an axon (2). As neurons continue to mature, the periodic distributed βII spectrin extends to more distal regions of axons and eventually fills the entire axon (2). With STED imaging and SiR-actin labeling, the actin filaments are also found as early as DIV2 and throughout the whole developmental stages, forming the same periodic structure as spectrin (5). Interestingly, the periodic adducin structure begins to appear in axons at around DIV6 (2). If the adducin forms a periodic structure at a relatively late stage, such a lack of adducin in capping actin filaments during early development might explain why actin filaments exist in a less stable form in the earlier developmental stages of neurons (2). These findings indicate that the periodic structure starts to form early during axon development and originates in the starting region of axons near the cell body. After the initiation of the lattice cytoskeleton structure's formation, it continues to mature with the actin filaments becoming more stable, capped by adducin. Once matured, the supercomplex of the periodic cytoskeleton structure possesses a relatively fixed molecular organization, becomes stable and rarely moves (2). While most signaling proteins in axon differentiation and development are highly expressed at the growing tip of axons (21), the subcortical periodic cytoskeleton structures instead originates at the proximal axon region. This indicates that the formation of this actin-spectrin-adducin lattice structure may be independent of the mechanisms for establishing or maintaining the polarity of neurons. Earlier studies show that the periodic cytoskeleton structure is predominantly observed in axons (3), only small, isolated patches of dendritic shafts exhibit periodic pattern of βII spectrin, and the periodicity of βII spectrin in dendrites appears less regular (2, 7). Ankyrin-B highly expresses in axons, and specifically targets βII spectrin (11). In wild type neurons, βII spectrin concentration in axons is about 2 times higher than in dendrites (2, 22, 23). Coincidentally, the spectrin mainly forms an obvious periodic structure in axons of wild type neurons (2, 7). A concentration-driven hypothesis can be formed based on these studies by inferring that higher concentrations of spectrin lead to a capability to form the periodic structure in neurons. Studies indicate that ankyrin-B knockout can cause substantial redistribution of βII spectrin in neurons (2, 24). Interestingly, the expression level of βII spectrin increases in dendrites and becomes indistinguishable from axons in ankyrin-B knockout neurons (2). Overexpression of βII spectrin substantially increases the chance of dendrites with the periodic distribution of βII spectrin (2). However, several studies report that the periodic structure of actin ring can be observed in a small fraction (~10-30%) of dendrites in living neurons labeled by SiR-actin using STED nanoscopy (5). Recently, Sidensteinet et al. found that βII spectrin showed a sharp periodic organization along all the dendrites decorated with spines, especially in the spine necks (8). These studies showed that, in dendrites, the periodic structure appeared more frequently than reported by earlier reports (2, 3).

The contradicting results, in terms of presence or absence of the periodic structure, could be due to many possible reasons. First, different actin populations may exist in cells, and different sub-populations of actin protein may have unequal affinity to labeling tools (25, 26). It is possible that phalloidin has a higher binding affinity to long actin filaments in cytosol versus subcortical actin rings, while SiR-actin, which labels endogenous actin in living cells with high specificity to subcortical actin, prefers binding to the actin rings. Since there are usually much higher concentrations of long actin filaments in dendrite shafts, this may explain the reason why with phalloidin labeling, researchers always visualize long F-actin signals in dendrites and only occasionally observe periodic actin ring structures, differing from results gained by SiR-actin labeling. Also, in dendrites, a dense layer of long filament mesh net structure of F-actin exists (3). If the periodic actin network is evident in dendrites, it would be very challenging to separate this periodic form

of cytoskeleton from the dense long F-actin filaments. In addition, the contradicting presence or absence of observed periodic structures in dendrites may also be caused by observations at different developmental stages and/or at different sizes of dendritic processes. Currently, it is generally believed that the periodic structure of cytoskeleton exists in dendrites, though with less regularity.

How this periodic structure develops in dendrites remains unknown. From the perspective of axons we know that βII spectrin may regulate the assembly of the periodic actin cytoskeleton (2, 4). But in dendrites additional investigations are needed to reveal the molecular mechanism. βIII spectrin, which is enriched in dendrites but not in axons (27-29), has been reported periodically distributed in dendrites (3), and may contribute to the assembly of periodic structures in dendrites.

The regulation of the periodic membrane skeleton seems to be more complex than previous thought, because other molecular factors may participate in this regulation. For example, intact microtubules are required for the formation of the periodic structure. A microtubule depolymerizing drug disrupts the periodic structure in axons, whereas stabilizing the microtubule by using drugs like taxtol or SB216763 promotes the formation of the periodic structure (2). The periodic structure is destroyed and not observed in STORM (2) or EM (18) images after membrane detergent extraction. Other unknown factors might also regulate such a precise periodic cytoskeleton structure. To systematically study these components related to the periodic structure, it is necessary for us to understand the regulatory mechanism. Proteomics techniques, like mass spectrometry, can help identify these unknown components and better understand the mechanism of the formation of the periodic cytoskeleton in neurons.

III. Function of the periodic cytoskeleton structures

What is the function of the periodic cytoskeleton in neurons and in other types of cells in the nervous system? Actin filaments form ring-like structures and are evenly spaced by spectrin tetramers in neurons. The first function of such a periodic actin-spectrin might be to physically support the cell membrane in neurons. Neurons possess multiple thin processes which are often needed to survey the surrounding environments and respond to multiple stimuli. In some cases, these thin processes may have to squeeze around the brain tissue and might need a relaxed and robust cytoskeleton to support such an action. Indeed, one spectrin subunit is comprised of many elastic repeats, permitting the flexible feature of submembranous cytoskeleton (23, 30), and thus the spectrin-based cytoskeleton might provide a robust and flexible mechanical support to the thin processes in neurons (2, 3). Disruption of the periodic structure by spectrin depletion in *C. elegans* not only led to axon collapse and breakage when animal was moving (31), but also impaired its sensitivity to external touch (32), supporting that the periodic skeleton might play a critical role in maintaining mechanical stability of axons.

Besides mechanical support, this highly periodic submembrane skeleton could organize important membrane molecules, such as voltage-gated sodium channels and cell adhesion molecules, into a periodic distribution along the axon (3). Anchoring proteins with varying biochemical and mechanical properties on the axonal plasma membrane might not only affect the generation and propagation of action potentials, but also influence other signaling pathways (33). The periodic subcortical actin-spectrin-adducin cytoskeleton may tightly connect with a variety of membrane molecules in dendrites. It is interesting to speculate whether the specialized organization of certain membrane molecules in dendrites may play essential roles in controlling the dendrite branches, regulating dendrite size, or instructing the morphogenesis of dendrite spines. How the periodic subcortical cytoskeleton establishes and carries out all of these fundamental biological functions remains to be answered and deserves further investigation. Investigating the generation of extended polymeric filaments *in vitro* by self-assembling may provide a possible strategy to illustrate the detailed mechanisms for the organization, interaction and remodeling of cytoskeletal elements. A recent study of ankyrin-G in the somatodendritic plasma membranes of hippocampal neurons showed its function in promoting GABAergic synapse stability through the inhibition of endocytosis (34). Moreover, ankyrin/spectrin networks have also been reported moving along the membrane and preventing lateral membrane endocytosis (35). It is likely that the subcortical periodic structures may be involved in the regulation of endocytosis.

The molecular components of the periodic skeletal structure are not evenly distributed. Specific isoforms of ankyrin and spectrin molecules, as well as other proteins, are found at discrete sites along the axon (3, 24, 33). With the different components and organization at discrete locations, do the heterogeneous structures have specific functions accordingly?

AIS, an essential subcellular compartment, assembles at the proximal axonal region during early developmental stages while neurons further mature (33, 36, 37). AIS is characterized by high expression of ankyrin-G and βIV spectrin, which replaces the βII spectrin isoform during development (23). Notably, both isoforms of spectrin have the same periodic pattern. βII spectrin's periodic pattern appears first while βIV spectrin's periodic pattern comes later during development. It is speculated that the periodic pattern forms first during an early developmental stage when a structural foundation is laid out. Later, other molecules add or replace existing molecules within this foundation. Other proteins, such as sodium channels and neurofascin (NF), are integrated in the lattice (3, 18, 33, 38, 39). These periodic molecules in AIS are not added randomly, instead they are added in a precisely controlled manner (2, 3, 33). AIS has been recognized as an essential functional compartment in neurons. It is critical for maintaining neuronal polarization, is generally considered to be the site of action potential generation, and is an important site for protein transportation. Whether the specific periodic cytoskeleton has any relation to the

above functions of AIS is unknown and deserves further investigation. Interestingly, the AIS structure is highly resistant to drugs that cause depolymerization of actins or microtubules, and is otherwise remarkably stable (2, 33), further supporting its critical function as the specific excitable domain of an axon.

Thus far, we have discussed the possible function of the periodic cytoskeleton structure in neurons without myelination. Most vertebrate axons in the central and peripheral nervous systems are myelinated, forming nodes of Ranvier which are electrically active domains of axon (40). Ankyrin-G is an essential scaffolding protein which could regulate sodium ion channel clustering at nodes of Ranvier (41). During early development neuron-glia interactions first cluster the cell adhesion molecule NF186, resulting in the recruitment of ankyrin-G (39). Sodium channels are subsequently recruited by ankyrin-G to the developing nodes (42). Then βIV spectrin can further stabilize the NF186-AnkG-sodium channel complex by interacting with ankyrin-G, resulting in a mature node of the cytoskeleton (43). The high density of sodium channels at nodes of Ranvier is a crucial feature in myelinated axons, and confers several important advantages, including decreased energy and space requirements, for the rapid propagation of action potentials (44). It is relevant to consider how the cytoskeleton is organized underneath the myelin coat, as well as at nodes of Ranvier. The most recent studies show that similar periodic cytoskeleton patterns exists under the myelin coat as compared to unmyelinated axons (6). The nodal cytoskeleton consists of ankyrin-G and βIV spectrin, with clear periodic organization just like the AIS (6). However, the actin concentration is very high at the nodes, and the fine subcortical actin structure requires future study. More glial and axonal proteins have been recently reported to exist at the nodes of Ranvier in sciatic nerve fibers with a periodic spatial arrangement (45). Nevertheless, the latest studies indicate that ankyrin-R/βI spectrin can compensate for loss of ankyrin-G/βIV spectrin, resulting in a secondary reserve method of sodium channel clustering in nodes of Ranvier (46). Whether the periodic cytoskeleton exists after this type of functional compensation is an interesting question to be studied. These multiple mechanisms to node of Ranvier formation ensure the stable molecular composition of the nodes and highlight their importance in efficient nervous system function.

Besides AIS and nodes of Ranvier, another highly specialized compartment of axons and dendrites is the synaptic site, including presynaptic and postsynaptic ends, which are essential for neuronal signal transmission. Actin is highly concentrated at synapses and involved in their assembly and development (18, 47). Spectrin is also found in synapses and plays crucial roles in the stabilization of synapses and formation of dendritic spines (48, 49). Does the actin-spectrin cytoskeleton exist at synapses? Interestingly, the axonal periodic cytoskeleton structure is disrupted at most presynaptic sites, but is observed in some dendrite spine necks from the dendritic shaft regions (7). Another study indicated that the periodic actin-spectrin lattice pattern was absent at presynaptic and postsynaptic sites (8). As previously proposed, the periodic cytoskeleton structures provide robust mechanical support in processes. Synapses are adaptable structures, which are built, pruned, and modified throughout the organism's whole life (50). These structural re-arrangements are believed to require the disassembly of the subcortical lattice structure. Furthermore, the presence of a tight periodic lattice might disrupt the fusion of synaptic vesicles and thus influence synaptic transmission (7, 8, 51). Thus, the absence of periodic cytoskeleton structure at synaptic sites might be due to the need for plasticity and rapid reorganizations which occur there (7).

Besides its functions in neurons, the periodic structure is sparsely observed in the processes of glial cells (6, 7), with functions which are still unclear and need further investigation. One possible reason for the sparse presence of periodic structures in glial cells may be due to the dynamic and transient nature of these cells. Furthermore, the degree of periodicity for spectrin distributions is positively correlated with the expression level of βII spectrin. βII spectrin levels in glial cells are similar to those in neuronal dendrites, but much lower than those in axons (52, 53). The high actin density in the cytosol of glial cells also hinders the ability to observe actin periodicity which may already be rarely present. Since *in vitro* glia cultures are quite different from their physiological conditions, further *in vivo* studies are important for illuminating the possible functions of periodic lattice in the development of glial cells.

Conclusions and perspectives

The ubiquity of the cytoskeleton periodicity throughout the nervous system underscores its fundamental importance to the development of various types of neurons (and likely some glial cells as well). Besides mechanically supporting and maintaining the membrane structure, the precisely organized periodic lattice may also affect many other cellular structures and functions, such as protein transport, cellular polarity, and excitability. Recently, Zhou et al. used super-resolution imaging to visualize colocalization of the cannabinoid type 1 receptor (CB1) and other related signaling proteins on the membrane-associated periodic skeleton (54). CB1 is one of the most abundant G protein-coupled receptors (GPCR) in the central nervous system and a therapeutic target for regulating appetite, pain, motor, mood and memory, as well as for treating neurodegenerative diseases (55). These new findings indicate that the periodic cytoskeleton structure play a role in GPCR's intracellular signaling and may be important for specific behavior and disease mediated by GPCRs.

However, more questions have been raised and many aspects need further investigation. What is the function of the periodic structures in dendrites and what factors determine its location in dendrites? Furthermore, why are the periodic structures disrupted in most presynapticboutons, yet formed in a significant fraction of dendritic spine necks? What is the relationship of periodic structures

and neuronal synapses? Beyond neurons, even more is unclear about how the periodic structure is formed or functions in glial cells. Thus, further studies on glial cells are essential for a more comprehensive understanding of the periodic cytoskeleton.

To study the formation, regulation and function of periodic cytoskeleton structure remain challenging. To meet these challenges, powerful labeling tools and novel imaging strategies to improve the spatio-temporal resolution, as well as enhancing the imaging sensitivity in thick samples, will be necessary. As novel methods are being developed today at a rapid pace, it will be exciting to see the elucidation of mechanisms of how cytoskeletal proteins control and regulate cellular development, function, and plasticity. Future studies could provide critical insights into future therapeutic interventions for human diseases of the nervous system related to the dysfunction of the cytoskeleton.

Acknowledgements

We would like to thank Dr. Garth J. Thompson for very helpful comments on proofreading the manuscript. This work was supported by the National Key Research and Development Program of China (2016YFC0905900 (G.Z.), 2017YFC 1001300 (G.Z.)), the National Natural Science Foundation of China (31771130 (G.Z.), the 2015 Thousand Youth Talents Plan of China (G.Z.).

Conflict of interest

The authors declare that they have no conflict of interest.

References

1. Kevenaar JT, Hoogenraad CC. The axonal cytoskeleton: from organization to function. Front Mol Neurosci. 2015;8:44.
2. Zhong G, He J, Zhou R, Lorenzo D, Babcock HP, Bennett V, et al. Developmental mechanism of the periodic membrane skeleton in axons. Elife. 2014;3.
3. Xu K, Zhong G, Zhuang X. Actin, spectrin, and associated proteins form a periodic cytoskeletal structure in axons. Science. 2013;339(6118):452-6.
4. Lukinavicius G, Reymond L, D'Este E, Masharina A, Gottfert F, Ta H, et al. Fluorogenic probes for live-cell imaging of the cytoskeleton. Nat Methods. 2014;11(7):731-3.
5. D'Este E, Kamin D, Gottfert F, El-Hady A, Hell SW. STED nanoscopy reveals the ubiquity of subcortical cytoskeleton periodicity in living neurons. Cell Rep. 2015;10(8):1246-51.
6. D'Este E, Kamin D, Velte C, Gottfert F, Simons M, Hell SW. Subcortical cytoskeleton periodicity throughout the nervous system. Sci Rep. 2016;6:22741.
7. He J, Zhou R, Wu Z, Carrasco MA, Kurshan PT, Farley JE, et al. Prevalent presence of periodic actin-spectrin-based membrane skeleton in a broad range of neuronal cell types and animal species. Proc Natl Acad Sci USA. 2016;113(21):6029-34.
8. Sidenstein SC, D'Este E, Bohm MJ, Danzl JG, Belov VN, Hell SW. Multicolour multilevel STED nanoscopy of actin/spectrin organization at synapses. Sci Rep. 2016;6:26725.
9. Byers TJ, Branton D. Visualization of the protein associations in the erythrocyte membrane skeleton. Proc Natl Acad Sci USA. 1985;82(18):6153-7.
10. Liu SC, Derick LH, Palek J. Visualization of the hexagonal lattice in the erythrocyte membrane skeleton. J Cell Biol. 1987;104(3):527-36.
11. Bennett V, Lorenzo DN. Spectrin- and ankyrin-based membrane domains and the evolution of vertebrates. Curr Top Membr. 2013;72:1-37.
12. Bennett V, Baines AJ. Spectrin and ankyrin-based pathways: metazoan inventions for integrating cells into tissues. Physiol Rev. 2001;81(3):1353-92.
13. An X, Lecomte MC, Chasis JA, Mohandas N, Gratzer W. Shear-response of the spectrin dimer-tetramer equilibrium in the red blood cell membrane. J Biol Chem. 2002;277(35):31796-800.
14. Fowler VM. The human erythrocyte plasma membrane: a Rosetta Stone for decoding membrane-cytoskeleton structure. Curr Top Membr. 2013;72:39-88.
15. Fischer RS, Fowler VM. Tropomodulins: life at the slow end. Trends Cell Biol. 2003;13(11):593-601.
16. An X, Salomao M, Guo X, Gratzer W, Mohandas N. Tropomyosin modulates erythrocyte membrane stability. Blood. 2007;109(3):1284-8.
17. Korobova F, Svitkina T. Molecular architecture of synaptic actin cytoskeleton in hippocampal neurons reveals a mechanism of dendritic spine morphogenesis. Mol Biol Cell. 2010;21(1):165-76.
18. Jones SL, Korobova F, Svitkina T. Axon initial segment cytoskeleton comprises a multiprotein submembranous coat containing sparse actin filaments. J Cell Biol. 2014;205(1):67-81.
19. Pielage J, Cheng L, Fetter RD, Carlton PM, Sedat JW, Davis GW. A presynaptic giant ankyrin stabilizes the NMJ through regulation of presynaptic microtubules and transsynaptic cell adhesion. Neuron. 2008;58(2):195-209.
20. Leite SC, Sampaio P, Sousa VF, Nogueira-Rodrigues J, Pinto-Costa R, Peters LL, et al. The Actin-Binding Protein alpha-Adducin Is Required for Maintaining Axon Diameter. Cell Rep. 2016;15(3):490-8.
21. Bradke F, Dotti CG. The role of local actin instability in axon formation. Science. 1999;283(5409):1931-4.
22. Riederer BM, Zagon IS, Goodman SR. Brain spectrin(240/235) and brain spectrin(240/235E): two distinct spectrin subtypes with different locations within mammalian neural cells. J Cell Biol. 1986;102(6):2088-97.
23. Galiano MR, Jha S, Ho TS, Zhang C, Ogawa Y, Chang KJ, et al. A distal axonal cytoskeleton forms an intra-axonal boundary that controls axon initial segment assembly. Cell. 2012;149(5):1125-39.
24. Lorenzo DN, Badea A, Davis J, Hostettler J, He J, Zhong G, et al. A PIK3C3-ankyrin-B-dynactin pathway promotes axonal growth and multiorganelle transport. J Cell Biol. 2014;207(6):735-52.
25. McGough A, Pope B, Chiu W, Weeds A. Cofilin changes the twist of F-actin: implications for actin filament dynamics and cellular function. J Cell Biol. 1997;138(4):771-81.
26. Munsie LN, Caron N, Desmond CR, Truant R. Lifeact cannot visualize some forms of stress-induced twisted F-actin. Nat Methods. 2009;6(5):317.
27. Sakaguchi G, Orita S, Naito A, Maeda M, Igarashi H, Sasaki T, et al. A novel brain-specific isoform of beta spectrin: isolation and its interaction with Munc13. Biochem Biophys Res Commun. 1998;248(3):846-51.
28. Stankewich MC, Tse WT, Peters LL, Ch'ng Y, John KM, Stabach PR, et al. A widely expressed betaIII spectrin associated with Golgi and cytoplasmic vesicles. Proc Natl Acad Sci USA. 1998;95(24):14158-63.
29. Gao Y, Perkins EM, Clarkson YL, Tobia S, Lyndon AR, Jackson M, et al. beta-III spectrin is critical for development of purkinje cell dendritic tree and spine morphogenesis. J Neurosci. 2011;31(46):16581-90.
30. Paramore S, Ayton GS, Mirijanian DT, Voth GA. Extending a spectrin repeat unit. I: linear force-extension response. Biophys J. 2006;90(1):92-100.
31. Hammarlund M, Jorgensen EM, Bastiani MJ. Axons break in animals lacking beta-spectrin. J Cell Biol. 2007;176(3):269-75.
32. Krieg M, Dunn AR, Goodman MB. Mechanical control of the sense of touch by beta-spectrin. Nat Cell Biol. 2014;16(3):224-33.

33. Leterrier C, Potier J, Caillol G, Debarnot C, Rueda Boroni F, Dargent B. Nanoscale architecture of the axon initial segment reveals an organized and robust scaffold. Cell Rep. 2015;13(12):2781-93.
34. Tseng WC, Jenkins PM, Tanaka M, Mooney R, Bennett V. Giant ankyrin-G stabilizes somatodendritic GABAergic synapses through opposing endocytosis of GABAA receptors. Proc Natl Acad Sci USA. 2015;112(4):1214-9.
35. Jenkins PM, He M, Bennett V. Dynamic spectrin/ankyrin-G microdomains promote lateral membrane assembly by opposing endocytosis. Sci Adv. 2015;1(8):e1500301.
36. Grubb MS, Shu Y, Kuba H, Rasband MN, Wimmer VC, Bender KJ. Short- and long-term plasticity at the axon initial segment. J Neurosci. 2011;31(45):16049-55.
37. Zhang C, Rasband MN. Cytoskeletal control of axon domain assembly and function. Curr Opin Neurobiol. 2016;39:116-21.
38. Kole MH, Ilschner SU, Kampa BM, Williams SR, Ruben PC, Stuart GJ. Action potential generation requires a high sodium channel density in the axon initial segment. Nat Neurosci. 2008;11(2):178-86.
39. Sherman DL, Tait S, Melrose S, Johnson R, Zonta B, Court FA, et al. Neurofascins are required to establish axonal domains for saltatory conduction. Neuron. 2005;48(5):737-42.
40. Susuki K, Rasband MN. Spectrin and ankyrin-based cytoskeletons at polarized domains in myelinated axons. Exp Biol Med (Maywood). 2008;233(4):394-400.
41. Dzhashiashvili Y, Zhang Y, Galinska J, Lam I, Grumet M, Salzer JL. Nodes of Ranvier and axon initial segments are ankyrin G-dependent domains that assemble by distinct mechanisms. J Cell Biol. 2007;177(5):857-70.
42. Gasser A, Ho TS, Cheng X, Chang KJ, Waxman SG, Rasband MN, et al. An ankyrinG-binding motif is necessary and sufficient for targeting Nav1.6 sodium channels to axon initial segments and nodes of Ranvier. J Neurosci. 2012;32(21):7232-43.
43. Yang Y, Ogawa Y, Hedstrom KL, Rasband MN. betaIV spectrin is recruited to axon initial segments and nodes of Ranvier by ankyrinG. J Cell Biol. 2007;176(4):509-19.
44. Susuki K, Chang KJ, Zollinger DR, Liu Y, Ogawa Y, Eshed-Eisenbach Y, et al. Three mechanisms assemble central nervous system nodes of Ranvier. Neuron. 2013;78(3):469-82.
45. D'Este E, Kamin D, Balzarotti F, Hell SW. Ultrastructural anatomy of nodes of Ranvier in the peripheral nervous system as revealed by STED microscopy. Proc Natl Acad Sci USA. 2016.
46. Ho TS, Zollinger DR, Chang KJ, Xu M, Cooper EC, Stankewich MC, et al. A hierarchy of ankyrin-spectrin complexes clusters sodium channels at nodes of Ranvier. Nat Neurosci. 2014;17(12):1664-72.
47. Jones SL, Svitkina TM. Axon initial segment cytoskeleton: architecture, development, and role in neuron polarity. Neural Plast. 2016;2016:6808293.
48. Honigmann A, Mueller V, Ta H, Schoenle A, Sezgin E, Hell SW, et al. Scanning STED-FCS reveals spatiotemporal heterogeneity of lipid interaction in the plasma membrane of living cells. Nat Commun. 2014;5.
49. Bates M, Huang B, Dempsey GT, Zhuang X. Multicolor super-resolution imaging with photo-switchable fluorescent probes. Science. 2007;317(5845):1749-53.
50. Goellner B, Aberle H. The synaptic cytoskeleton in development and disease. Dev Neurobiol. 2012;72(1):111-25.
51. Ruiz-Canada C, Budnik V. Synaptic cytoskeleton at the neuromuscular junction. Int Rev Neurobiol. 2006;75:217-36.
52. Susuki K, Raphael AR, Ogawa Y, Stankewich MC, Peles E, Talbot WS, et al. Schwann cell spectrins modulate peripheral nerve myelination. Proc Natl Acad Sci USA. 2011;108(19):8009-14.
53. Goodman SR, Lopresti LL, Riederer BM, Sikorski A, Zagon IS. Brain spectrin(240/235A): a novel astrocyte specific spectrin isoform. Brain Res Bull. 1989;23(4-5):311-6.
54. Zhou RB, Han BR, Xia CL, Zhuang XW. Membrane-associated periodic skeleton is a signaling platform for RTK transactivation in neurons. Science. 2019;365(6456):929-+.
55. Howlett AC, Barth F, Bonner TI, Cabral G, Casellas P, Devane WA, et al. International Union of Pharmacology. XXVII. Classification of cannabinoid receptors. Pharmacol Rev. 2002;54(2):161-202.
56. Bar J, Kobler O, van Bommel B, Mikhaylova M. Periodic F-actin structures shape the neck of dendritic spines. Sci Rep. 2016;6:37136.

RESEARCH ARTICLE

The Role of Network Architecture in the Onset of Spontaneous Activity

Diletta POZZI[a,b*], Nicolò MENEGHETTI[c], Anjan ROY[d], Beatrice PASTORE[a], Alberto MAZZONI[c], Matteo MARSILI[d] and Vincent TORRE[a,e,f]

[a] *Neurobiology Sector, International School for Advanced Studies (SISSA), via Bonomea 265, 34136 Trieste, Italy.*
[b] *Department of Otolaryngology, Head and Neck Surgery, Stanford University School of Medicine, 300 Pasteur Drive, 94305 Stanford, California.*
[c] *Computational Neuroengineering Lab, The Biorobotics Institute, Scuola Superiore Sant'Anna, Viale Rinaldo Piaggio 34, 56125, Pontedera (PI), Italy.*
[d] *Abdus Salam International Center for Theoretical Physics (ICTP), Strada Costiera 11, 34014 Trieste, Italy.*
[e] *Cixi Institute of Biomedical Engineering (CNITECH), Ningbo Institute of Materials Technology and Engineering, Chinese Academy of Sciences, Zhejiang, 315201, P. R. China.*
[f] *Center of Systems Medicine, Chinese Academy of Medical Sciences, Suzhou Institute of Systems Medicine (ISM), Suzhou Industrial Park, Suzhou, Jiangsu, 215123 P.R. China.*

*Correspondence: dpozzi@stanford.edu
https://doi.org/10.37175/stemedicine.v1i1.1

ABSTRACT

Background: The spontaneous activity of neuronal networks has been studied in *in vitro* models such as brain slices and dissociated cultures. However, a comparison between their dynamical properties in these two types of biological samples is still missing and it would clarify the role of architecture in shaping networks' operation.

Methods: We used calcium imaging to identify clusters of neurons co-activated in hippocampal and cortical slices, as well as in dissociated neuronal cultures, from GAD67-GFP mice. We used statistical tests, power law fitting and neural modelling to characterize the spontaneous events observed.

Results: In slices, we observed intermittency between silent periods, the appearance of Confined Optical Transients (COTs) and of Diffused Optical Transients (DOTs). DOTs in the cortex were preferentially triggered by the activity of neurons located in layer III-IV, poorly coincident with GABAergic neurons. DOTs had a duration of 10.2 ± 0.3 and 8.2 ± 0.4 seconds in cortical and hippocampal slices, respectively, and were blocked by tetrodotoxin, indicating their neuronal origin. The amplitude and duration of DOTs were controlled by NMDA and GABA-A receptors. In dissociated cultures, we observed an increased synchrony in GABAergic neurons and the presence of global synchronous events similar to DOTs, but with a duration shorter than that seen in the native tissues.

Conclusion: We conclude that DOTs are shaped by the network architecture and by the balance between inhibition and excitation, and that they can be reproduced by network models with a minimal number of parameters.

Keywords: Neuronal network · Calcium imaging · GABAergic neuron · Power law · Neural model

Introduction

A spontaneous electrical activity represents the noise in the nervous system that underlies its operation (1). As opposite, artificial computing elements such as electronic devices have a very low intrinsic noise and are almost noise-free. How the brain copes with its background noise is a major issue of computational neuroscience.

The spontaneous activity of several brain regions - and in particular of the cortex - shows rapid transitions between periods of intense and synchronous firing (Up states) and of reduced or almost absent electrical activity (Down states) (2-4). These transitions have been observed in rodents performing a variety of tasks (2, 5-7), in monkeys (8) and also *in vitro* in cortical slices (9-11), even when afferent cortical inputs were destroyed. These observations show that an intermittent behavior is intrinsic to the neuronal network and is not caused by the modulation of external inputs (12). These transitions occur at different frequency

ranges depending on the brain region: in the cerebral cortex, they occur in the range of slow oscillations (0.5 - 1 Hz) (3) whereas in the hippocampus mainly in the theta frequency range (4 - 8 Hz) (13). Moreover, some slow oscillations are observed in the presence of a coordinated firing between the hippocampus and the cortex (14). In order to explain these transitions, several models of interacting excitatory and inhibitory neurons have been proposed (15) in which intermittency is explained as originating primarily from synaptic noise (16). In alternative models, based on simple sets of differential equations, intermittency has a more deterministic origin (17, 18) in a way reminiscent of what observed in chaotic systems. However, it is still to be addressed if this intermittency arises because of the mere biophysical properties of randomly interconnected neurons, or if the network cyto-architecture plays important roles instead. A functional characterization of the same neuronal population preserving the original cyto-architecture and after dissociation allows evaluating the role of the network architecture in shaping its spontaneous activity.

In this manuscript, we characterized the spontaneous electrical activity of cortical and hippocampal slices from GAD67-GFP mice (19) using conventional calcium imaging (5,20). In this transgenic mouse line, inhibitory GABAergic (GABA+) neurons are labeled with the green fluorescent protein (GFP) so it is possible to identify these neurons and to characterize their role. Here we aim to recover global dynamical properties of cortical and hippocampal networks and a single neuron resolution is not necessary. Therefore, we used calcium imaging with conventional wide-field fluorescence microscopy and not two-photon imaging (21). In our experimental conditions, we obtained an optical trace averaged along the z-axis from which we could identify the onset of Diffuse Optical Transients (DOTs, characterized by a synchronous activation extending in all directions) and Confined Optical Transients (COTs), which were limited to sparse and uncorrelated events.

In addition to the spontaneous activity of slices preserving their original connectivity, we analyzed calcium transients from neuronal cultures obtained after dissociation of the cortex and hippocampus. In these experiments, given the single layer organization of the networks under investigation, calcium transients originating from individual neurons (either GABA+ or GABA-) were unequivocally identified. Modelling with simplified neural networks shows that the dynamical differences of the spontaneous activity between slices and dissociated cultures are due to the multilayer organization of the native tissue.

Materials and Methods

Ethical approval

All procedures were in accordance with the guidelines of the Italian Animal Welfare Act, and their use was approved by the Local Veterinary Service, the SISSA Ethics Committee board and the National Ministry of Health (Permit Number: 2848 - III/15) in accordance with the European Union guidelines for animal care (d.1.116/92; 86/609/C.E.). The animals were anaesthetized with CO_2 and sacrificed by decapitation, and all efforts were made to minimize suffering.

Slice preparation

Slices formed by organotypic cultures were prepared from hippocampal and cortical region of GAD67-GFP mice brain, according to the Gähwiler method (22). Hippocampus together with entorhinal cortex was isolated from 4-6-day-old (P4-P6) postnatal animals. The isolated tissue was cut into 350 µm thick transverse slices by means of a tissue chopper (McIlwain, UK). The slices were placed in GBSS solution (g/l: $CaCl_2 \cdot 2H_2O$ 0.22; KCl 0.37; KH_2PO_4 0.03; $MgCl_2 \cdot 6H_2O$ 0.21; $MgSO_4 \cdot 7H_2O$ 0.07; NaCl 8; $NaHCO_3$ 0.227; Na_2HPO_4 0.12) added with Kynurenic acid (final concentration 1 mM) and D-glucose (final concentration 28 mM), and kept at 4 degrees for 1 hour. Slices were then attached on a glass coverslip 12·24 mm (OrsaTec) with reconstituted chicken plasma (Sigma) coagulated by thrombin (200 U/ml - Merck). After coagulation the coverslips were inserted into plastic-one side flat tubes (Nunc) with 0.75 ml of medium containing 25% horse serum (Gibco), 50% basal medium Eagle (Gibco) added with L-glutamine, and 25% Hanks balanced salt solution (Gibco), enriched with glucose to a concentration of 28 mM. The tubes were kept in a roller drum rotating (10 revolutions per h), in incubator at 37 °C.

In a separate set of experiments, organotypic cultures were prepared according to the Stoppini method (23). The procedure was identical to the Gähwiler method until the cutting and incubation in GBSS solution at 4 degrees. Slices were then placed on sterile, transparent semiporous membranes in six well multiwell (Falcon), with 1 ml of Neurobasal medium added of B27 supplement (ThermoFisher), the same medium that was used for dissociated cell cultures. The multiwell were kept in an incubator at 37 °C, with 5% of CO_2. In both protocols, the culture medium was changed every five days.

Dissociated cell cultures preparation

Cortical and hippocampal dissociated cell cultures were prepared from GAD67-GFP mice (P0-P1). Glass coverslips (15 mm diameter) were coated with 50 µg/ml poly-L-ornithine (Sigma-Aldrich, St. Louis, MO, USA) overnight, and just before cells' seeding, a thin layer of Matrigel (diluted 1:50 with culture medium; Corning, Tewksbury MA, USA) was applied. The cortex and hippocampus were isolated and dissected separately. In both cases, the cultures were prepared at two different cell's concentrations. After enzymatic and mechanical dissociation, cells were resuspended at a concentration of $1(2) \cdot 10^6$ cells/ml in minimum essential medium (MEM) with GlutaMAXTM supplemented with 10% dialyzed fetal bovine serum (FBS, all from Thermo Fisher Scientific, Waltham, MA, USA), 0.6% D-glucose, 15 mM Hepes, 0.1 mg/ml apo-transferrin, 30 µg/ml insulin, 0.1 µg/ml D-biotin, 1 µM vitamin B12 and 2.5 µg/ml gentamycin (all from Sigma-Aldrich). Cells

were then plated at a density of 500 (1000) cells/mm^2 on glass coverslips. After incubation for 30 min at 37 °C, the growing medium was added consisting of Neurobasal medium supplemented with B27, GlutaMAXTM and 2.5 µg/ml gentamycin (all from ThermoFisher). Half of the medium was changed after 48 h adding 2 µM cytosine-β-D-arabinofuranoside (Ara-C; Sigma-Aldrich). The neuronal cultures were maintained in an incubator at 37 °C, 5% CO_2 and 95% relative humidity. Half of the medium was again changed once per week.

Calcium imaging

Calcium imaging experiments on organotypic slices were performed using the Rhod-3 Calcium Imaging Kit (Thermo Fisher) for non-ratiometric analysis. According to the manufacturer's instructions, the samples were incubated for 45' at room temperature in Ringer solution (145 mM NaCl, 3 mM KCl, 1.5 mM $CaCl_2$, 1 mM $MgCl_2$, 10 mM glucose and 10 mM Hepes, pH 7.4) containing the red-fluorescent dye at a concentration of 10 µM.

Calcium imaging experiments on dissociated cell cultures were performed using the non-ratiometric calcium-binding dye Fura Red, AM (Thermo Fisher), since we observed frequent cells' toxicity when incubating dissociated neurons with Rhod-3. The samples were incubated for 45' at room temperature in Ringer solution (145 mM NaCl, 3 mM KCl, 1.5 mM $CaCl_2$, 1 mM $MgCl_2$, 10 mM glucose and 10 mM Hepes, pH 7.4) containing the red-fluorescent dye at a concentration of 5 µM. Pluronic F-127 20% solution in dimethyl-sulfoxide (Thermo Fisher Scientific) was added at a ratio 1:1 with the dye for increasing cells' permeability.

After incubation, both type of samples were transferred to a glass-bottom Petri dish in order to allow visualization in a Nikon Eclipse Ti-U inverted microscope equipped with an HBO 103 W/2 mercury short arc lamp (Osram, Munich, Germany), a mirror unit (exciter filter BP 465-495 nm, dichroic 505 nm, emission filter BP 515-555) and an Electron Multiplier CCD Camera C9100-13 (Hamamatsu Photonics, Japan). Images were acquired using the NIS Element software (Nikon, Japan) with an S-Fluor 20X/0.75 NA objective and 512·512 spatial resolution. To avoid saturation of the signals, excitation light intensity was attenuated by ND4 and ND8 neutral density filters (Nikon). The recordings were performed at room temperature.

Cortex and hippocampus of a same slice were imaged subsequently. Given the slow time course of measured calcium transients, an acquisition rate of 3 - 10 Hz was found to be adequate. In some control experiments, we reached an acquisition rate of 50 Hz by increasing the intensity of the illuminating light and the binning of pixels; in this case, the total recording time was 5 minutes. During our optical recordings some dye bleaching occurred and the exponential decline of the basal fluorescence was corrected with our custom-made software.

Data Analysis

Preprocessing of image sequences

The pre-processing of the acquired videos consisted of two steps. First, we removed the bleaching – driven drift in the z-profile's baseline via linear de-trending. The drift has been corrected by interpolating the points belonging to the baseline in in order to get a function $z_{(t)}$: then every i-th frame has been multiplied by $z_{(0)}/z_{(i)}$. This operation was performed image-wise (i.e., the videos' z-profile has been computed as the mean intensity value of each frame) for control recordings and pixel-wise (i.e., the bleaching has been corrected considering the intensity profile of each pixel separately) for TTX-APV recordings. Second, we measured the changes in fluorescence intensity over time ($\Delta F/F_{(0)}$) using the open source ImageJ plugin dFoFmovie-CatFullAutoSave.ijm (https://gist.github.com/ackman678/11155761).

Image sequence analysis

We identified the activity events as follows. The first step was to binarize each image with a thresholding procedure defining the active pixels in each image. Thresholds were manually set by the experimenter. Then we defined as event a region of contiguous active pixels larger than 16 µm^2.

Two events sharing pixels in consecutives frames are considered to be the same event propagating through time. We define event-splitting when in the *n+1* frame there are two (or more) "descendants" events whose areas overlap with the area of a single event in the *n* frame. We define events-merging when, in the when in the *n+1* frame, there is one event whose area has an overlap with the area of two (or more) "ancestors" events in the *n* frame.

Once the events were identified, we computed and analyzed two features: the events duration and the maximal area reached by the event during its lifetime. The event duration is the time from the birth and the death of the event, i.e., the first and last frame in which its area was above threshold. In case of splitting, death is defined as the frame in which the last sub-event dies, and in case of merging birth is the frame in which the first of the two originating events was born. The maximal of the area is the maximum value (as number of µm^2 occupied) reached by an event, considering all ancestor and descendants. We define at this stage "Diffused Optical Transients" the events whose maximal area exceeds half of the area of the slice under investigation, and all the other events as "Confined Optical Transients". Probability distribution of duration and area of Confined Optical Transients are defined with an exponential binning and fit with a power law distribution. We used n_bins = 12 for the events duration distribution, and n_bins = 42 for the events area distribution, but the number of bins has a minimal effect on duration power law and no effect on area power law (see **Supplementary Figure 2**).

The TTX-related image sequences have undergone an additional frequency analysis step, in order to test whether their activity time scales slowed down compared to controls. Using a binary grid of Regions Of Interest, the intensity profile of every region across frames was extracted, and we computed the fast Fourier transform of

each profile. After averaging over the FFT-transforms of the profiles of different ROIs, the result has been filtered with a Moving Average Filter of order n = 5 using the Matlab built-in function *filtfilt*.

Computation of correlation coefficient of optical signals

The correlation coefficient $\rho(t)_{Peak}$ between peaks of calcium transients was computed as follows. The times, t_i, at which transient peaks occurred are presented in a conventional raster plot. The raster plot for neuron i and neuron j ($\rho(t_{ij})_{Peak}$) was computed by dividing the total recording time into intervals of 1 or 10 s. Thus, if f_{in} and f_{jn} are the number of calcium transients of neuron i and neuron j in the time interval Δt_n, $\rho(t_{ij})_{Peak}$ is computed as follows:

$$\rho\,(tij)\ \text{Peak} \;=\; \frac{\Sigma_n f_{in} f_{jn}}{\sqrt{\left(\Sigma_n f_{in}^2\right)\left(\Sigma_n f_{jn}^2\right)}}$$

Statistical analysis

Data are shown as the mean ± standard error of the mean from the number of samples indicated in each experiment (see **Results** and figures captions). Distributions of data from two different data series were compared using the nonparametric test Kruskal-Wallis. The distance between experimental distributions and the corresponding theoretical binomial distributions was calculated using the nonparametric Kolmogorov-Smirnov test. The mean values from two or three data series were compared with One-Way ANOVA and Wilcoxon rank-sum tests. All statistical tests were performed using Matlab software.

Power law fitting

We followed the methods described in Clauset et al. 2009 (24) to assess the quality of our fit with power law distributions and determine the optimal power law parameters. The maximum likelihood estimator alpha (see Eq. 3.1 in Clauset et al. 2009) and the lower bound of the power law behavior x_{min} were estimated simultaneously according to the goodness-of-fit based method. We have a sufficiently large dataset to use the continuous approximation for alpha. For each possible choice of x_{min}, alpha is estimated via the method of maximum likelihood, and we calculated the Kolmogorov-Smirnov goodness-of-fit statistic D (see Eq. 3.9 in Clauset et al 2009). We then select as our estimate of x_{min}, the value that gives the minimum value of D.

Once we defined the optimal parameters for the power law fit we performed a goodness of fit test of the power law hypothesis (see section 4 of Clauset et al 2009). We generated 1000 power-law distributed synthetic data sets with scaling parameter alpha and lower bound x_{min} equal to those of the distribution that best fits the observed data. We have fit each synthetic data set individually to its own power-law model and calculated the KS statistic for each one relative to its own model. The fraction of the time that the resulting statistic is larger than the value for the empirical data defines our p-value. Following the indication of Clauset et al 2009 (section 4.1) we ruled out the power law hypothesis for $p \leq 0.1$, otherwise we concluded that the distribution was compatible with a power law.

Neural modelling

We have developed highly simplified models of neural networks interacting in a single layer. From these models, we extended the modelling to multilayer networks. One key ingredient of these models is the presence of long-tailed distributions - more precisely, distributions with a power law behaviour. The technicalities of these models are described in the next paragraphs.

Single Layer models

We model the system as a network of N neurons, where each neuron is connected to NC randomly chosen neurons (Fig. 7A). At each simulation time step, one unit of charge is added to a randomly selected neuron. A threshold potential V_{th} is assigned to each neuron, drawn from a probability distribution $\rho(V_{th})$. As long as the total charge in the neuron is less than its threshold, the neuron remains silent. When the threshold is reached, the neuron "fires". We have studied two classes of models, characterized by the way the firing neuron perturbs its neighbours. In Model 1, the firing neuron distributes all its charge randomly among its NC neighbours, while in Model 2 the firing neuron gives the same fraction of its charge φ to its NC neighbours, and resets its own charge to zero. Upon firing, its threshold is reset by drawing it at random from $\rho(V_{th})$. Its NC neighbours list is randomly reset as well. If some of the NC neighbours reach their threshold V_{th} from the input of the firing neuron, they fire as well and randomly reset their parameters. This continues till no neuron with charge above V_{th} remains. Thus, a single neuron firing may start an avalanche propagating throughout the network. All these relaxations happen instantaneously in the simulation time frame. At the subsequent simulation time step, a new charge is injected to a randomly chosen neuron and the process goes on. In order to have a stationary state, we introduced the parameter λ, representing dissipation as the probability in which the charge of the firing neuron is removed from the network (instead of being distributed to its neighbours). Since dissipation reduces the amount of excitation, we can consider it as a simplified form of inhibition, caused either by the network inhibition or by an intrinsic adaptation/inactivation.

We define the size of an avalanche (s) as the number of firing events involved in an avalanche, and the volume of the avalanche (v) as the number of distinct neurons taking part in it. We find that if the threshold is constant or if $\rho(V_{th})$ is Gaussian, then the resulting distribution of size of avalanche follows a power law $s^{-\tau}$ with $\tau < 2$. In that case, avalanches of all sizes are possible in the network and the network can always distribute all its charge without requiring a global event involving the entire network. However, if $\rho(V_{th})$ has a long tailed distribution such as a power law ($\rho(V_{th}) \sim V_{th}^{-\alpha}$ with $\alpha < 2$), we again obtain a power law distribution for the size of avalanche, but now

with $\tau > 2$. In this case, an average avalanche size for the network exists and - if the dissipation λ is small enough - the network needs a global event to relax. **Fig. 7C** shows these results for a network with N = 10,000 neurons, NC = 10, $\alpha = 1.5$ and $\lambda = 0.01$ in Model 1. For Model 2, we selected $\varphi = 0.1$ and $\lambda = 0.01$. Some global events appear in these simulations as spikes at v = N. The global events occurring in these models correspond to the experimentally observed diffuse optical transients, here referred as DOTs (see **Results, Fig. 1-4**).

For both models, we have also studied variations where NC is power law distributed, or the number of neurons perturbed at each time step is random. These variations did not change the results as far as the power law and the resonance is concerned. However, as expected, adding charge to multiple neurons at each time step increases the frequency of the avalanches.

Multilayer models

In order to explore the reason for the broader width of the DOTs in the cortex, we extend the above model to a multilayer model. In the multilayer model, each layer has a similar structure as in the previous model, but now every neuron in each layer also has one connection to a neuron in the next layer (**Fig. 7E**). Following the same rules as for the single layer case, a neuron transfers its charge randomly among its NC neighbours in the same layer and one neighbour in the next layer. After the stability of all neurons in a layer is confirmed like in the single layer case, we check for unstable neurons in the next layer and continue this process. Note that all this sequence happens at the same simulation time step, before some charge is added to another random neuron. However, we assume that the relaxation in subsequent layers happen with a time delay $\Delta\tau$ and we used it while plotting the time series. In **Fig. 8F** and **8I** we show that indeed a broad DOT, reminiscent of the structure observed in experiments, can appear in such a simple cyclic multi-layer model. This happens because of multiple simultaneous DOTs appearing in the different layers but with a time delay $\Delta\tau$. These DOTs appear in a cyclic fashion; a DOT appearing in any of the layer triggers a DOT in the next layer and it continues through the consecutive layers till all the unstable neurons relax, either by transferring their charge or by dissipating them. The quantity $\Delta\tau$ is ad-hoc in the current analysis and indicates the existence of functional layers interacting with each other with a time delay. In simulations, its exact value can be adjusted, along with the number of neurons perturbed at each time step, in order to obtain a time series reminiscent of the one observed in experiments.

Results

The mouse cortex is composed of 6 layers (LI-VI) and is approximately 500 - 1000 μm thick (**Figure 1A**) depending on the region (25). The most superficial layer (LI) is 50 - 80 μm thick and is primarily composed of GABA+ neurons, while excitatory neurons are located in layers II-VI (see for a review (26)). The hippocampal system consists of the dentate gyrus (DG), the four regions of the cornu ammonis (CA1-3) fields and the subiculum (Sub) (**Supplementary Figure 1A**). Our imaging experiments were performed with a 20X objective in areas corresponding to cortical layers I-IV and hippocampal CA1-3, all of them expressing GABA+ neurons.

The slices were prepared from the medial temporal lobe overlying the hippocampus, corresponding to the entorhinal cortex. The native connectivity between the two regions was maintained. In a separate set of experiments instead, the cortex and hippocampus from the same slice were mechanically separated. After 1 or 2 weeks in culture, a thickness of 50 - 70 μm was measured (see **Supplementary Figure 2**) corresponding to approximately 5 - 6 cellular layers. When imaging the slices with a conventional epi-fluorescence microscope, the identification of calcium transients at the single cell level was distorted - at some extent - by the light scattering from nearby focal planes. Nonetheless, we were able to identify the emergent collective properties of the cortical and hippocampal networks.

The spontaneous activity in cortical networks

Slices were stained with the fluorescent Calcium indicator Rhod 3 - AM (**Figure 1B**). The spontaneous activity was recorded by measuring optical transients using a high resolution and high sensitivity EM-CCD camera (**Supplementary Video 1**) acquiring images at 5 - 50 Hz. The total recording time for each session varied from 10 up to 40 minutes and, during this time, the emitted fluorescence $F_{(t)}$ could decrease by 10-30 %, because of dye bleaching. Following correction for the bleaching, the fractional optical signal $\Delta F/F_{(0)}$ was computed (**Supplementary Video 2**), assigning t = 0 at the beginning of the recording, from the entire imaged slice (blue trace in **Figure 1D**) and therefore referred as $\Delta F/F_{network}$. In addition, $\Delta F/F_{(0)}$ was computed from regions of interest (ROIs) corresponding to active cortical areas comprising both GABA+ and GABA- neurons (colored traces in **Figure 1D**). We observed confined optical transients (COTs) in areas ranging from few tens (corresponding to 1-5 cells) up to 11.000 μm^2 (see areas inside red circles in **Figure 1E**). Moreover, we observed diffused optical transients (DOTs) which invaded almost all layers of the visualized slice (**Figure 1F**) with a frequency varying from 0.2 to 4 per minutes. After computing the $\Delta F/F_{network}$, DOTs appear as large peaks with a fast rising time, which was in the order or below our recording time resolution (20 - 200 ms).

The distribution of the maximal area of observed optical transients (COTs and DOTs) was broad and exhibited a power law behavior over almost 3 log units (**Figure 1G**), with an average slope of 1.87 ± 0.42 (see **Table 1**). The duration of COTs did not follow a power law instead (**Figure 1H**). In 22 out of 27 slices analyzed, the distribution of maximal areas had an outlier point corresponding to the occurrence of DOTs (see the arrows in **Figure 1G**). The number of distinct COTs observed in the same frame fluctuated in time around a mean value of 30 (**Figure 1I**). During the appearance of a DOT, the

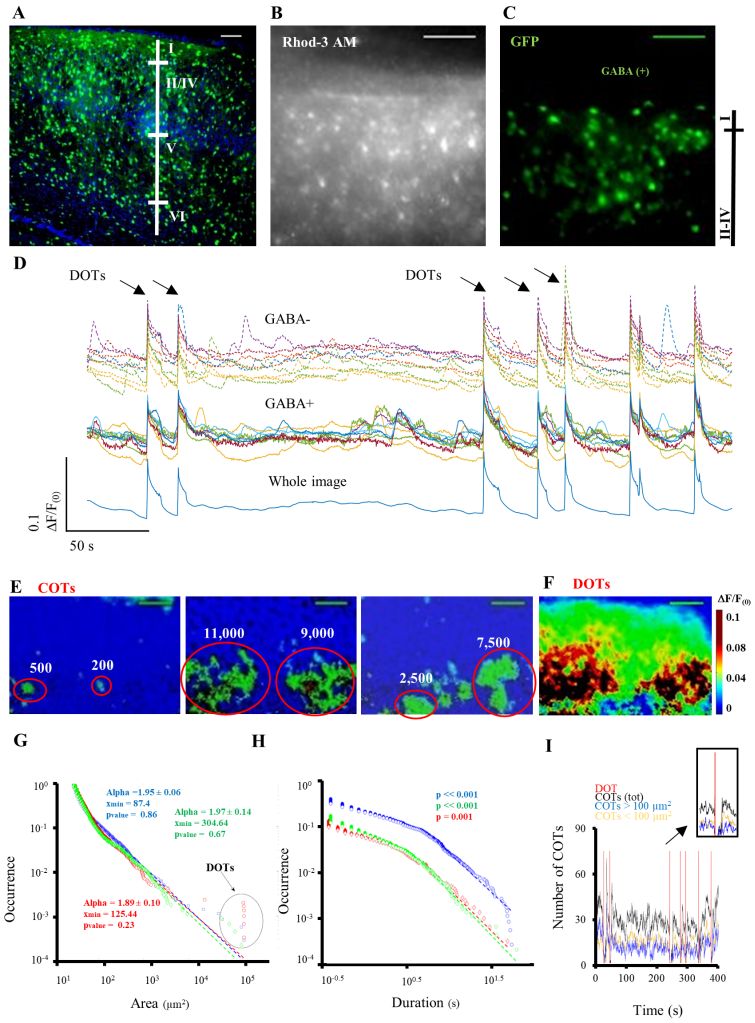

Figure 1: Spontaneous calcium transients in the cortex. (A) Fluorescent image of cerebral cortex from a GAD67-GFP mouse (P5) with DAPI nuclear staining; GABA+ neurons are labeled in green. The white vertical bar indicates the putative layers. **(B)** Organotypic slice from the same mouse line loaded with the fluorescent indicator Rhod-3 AM during calcium imaging, and corresponding GABA+ neurons **(C)** in the same field of view. The black vertical bar on the right indicates the approximate limits of cortical layers in this example. **(D)** $\Delta F/F_{(0)}$ traces from the whole image (blue trace at the bottom, defined as $\Delta F/F_{network}$) and from selected GABA+ (colored traces in the middle) and GABA- neurons (colored traces on top) from a calcium imaging recording. **(E)** Examples of Confined Optical Transients (COTs) from the pseudo-color $\Delta F/F_{(0)}$ movie of the recording, showing isolated regions of variable sizes (see red circles; the rounded numbers are expressed in μm^2). **(F)** Example of Diffuse Optical Transient (DOT), where the increase in $\Delta F/F_{network}$ involves more than 50% of the imaged slice. Color bar on the right. Scale bars: 80 μm in both fluorescence and pseudo-color images. **(G, H)** Probability distribution of area and duration of COTs in the cortex. Circles, rhombus and asterisks represent data from three representative experiments: the corresponding dotted lines in (H) show the linear fitting for each distribution. DOTs are visible as resonances outside the area's distributions (see black circles). Insets indicates test of power law hypothesis and, only if $p > 0.1$, power point slope (alpha) and onset. **(I)** Density of COTs over time for different area sizes (COTs < 100 μm^2 and COTs > 100 μm^2, yellow and blue line respectively) and for all sizes (black line) with reference to DOTs occurrence (red vertical lines). The inset shows the decrease in COTs density corresponding to DOTs' occurrence.

number of COTs drastically decreased and increased again at the DOT termination, when the diffuse activation - invading almost the entire slice - broke in several smaller active regions (**Figure 1I**, inset). The intermittency between COTs and DOTs, as well as the power law distributions of maximal area and duration, were similar in hippocampal slices (see **Supplementary Figure S1**).

Origin of COTs and DOTs

Recorded optical transients (both COTs and DOTs) could originate from neurons and/or glial cells. In order to evaluate the contribution of glial cells, we compared optical transients before and after the addition of 1 μM tetrodotoxin (TTX), a well-known blocker of neuronal activity (27, 28). The application of TTX completely abolished DOTs in cortical slices (**Figure 2A**), but residual optical transients could be still detected. However, these transients had a slower rising phase and time course, as demonstrated by the computation of the power spectrum density PSD: in the presence of TTX, the PSD decreased in an almost continuous trend, while in control conditions the signals exhibited an increase between 0.015 and 0.03 Hz (**Figure 2B**). Moreover, when the distribution of maximal areas of events in TTX was subtracted to

that observed in control (Con) conditions, the resulting distribution was very similar to that seen prior to subtraction, as well as the number of events detected (**Figure 2C**). For these reasons, we concluded that the large portion of calcium transients observed in control conditions originates primarily from firing neurons and only at a minor extend from glial cells. We cannot exclude, however, the contamination from slow calcium waves driven by metabotropic glutamate receptors present both in neurons and glial cells (29).

After application of the GABA-A receptors antagonist bicuculline 50 µM in cortical slices, the size and duration of DOTs visibly increased (**Figure 2D**). As opposite, the amplitude and duration of DOTs were significantly reduced by the application of 50 µM APV (**Figure 2E, F**), suggesting that DOTs originate primarily from the activation of NMDA receptors (30, 31). The distribution of maximal areas of events (**Figure 2G**) were similar in control conditions and in the presence of APV. Therefore, the activation of NMDA receptors is not the main mechanism causing COTs and that the activation of kainate and AMPA glutamate receptors, together with persistent sodium currents plays an important role (32 - 34). All these experimental observations show that DOTs exhibit a pharmacology very similar to that of usual Up states (10, 35).

Optical recordings of DOTs have a sharp rising phase, reminiscent of the rising phase of an action potential in a single neuron. An action potential in a neuron occurs when the summation of synaptic inputs reaches a threshold and a regenerative mechanism is activated. It is conceivable, therefore, that DOTs occur when the overall neuronal activity reaches a given threshold and a regenerative mechanism - operating at the network level - causes a collective excitation to occur (36). There is also a possible alternative possibility: the appearance of DOTs is favored or triggered when specific clusters or sets of neurons are activated. In order to test this possibility, we investigated whether DOTs are initiated by the activation of *privileged/specific* regions - which we refer as starters - or instead their appearance depends on the activation of enough neurons *randomly* distributed in the slice. In the first case, a statistical analysis could reveal the existence of "starters", i.e. of cortical regions whose activation is more likely to trigger or precede a DOT, in the latter case the appearance of a DOT is caused by the concomitant occurrence of a sufficient number of random events. In order to obtain an adequate statistical verification, we prolonged our imaging experiments to 30 - 40 minutes and occasionally up to 1 hour, so to observe several tens of DOTs. In our long recordings, some bleaching occurred which was compensated and the stained slice exhibited optical transients with the same frequency and amplitude during the total observation time (**Figure 3A**). All the frames before the occurrence of the DOT were analyzed, and each pixel was binarized with a threshold corresponding to the 30% of the maximal $\Delta F/F_0$ from the whole image, so to obtain a map of the seeds of the DOTs (**Figure 3B**). If these seeds do not have any significant spatial correlation, then the origin of DOTs is random, but if these seeds exhibit some correlation than the existence of starters of DOTs finds some support.

We calculated the spatial overlap between these seeds and we colored the pixels according to their frequency of appearance in the seeds, with red and dark red indicating a high appearance (**Figure 3C**). If a pixel participated to a seed in a random way, its statistics is expected to follow a binomial distribution $P(\pi, x, N)$ (37): in this case if π is probability of pixel to be active, the probability P of x occurrence in series of N trials is:

$$P(x) = \frac{N!}{x!\,(N-x)!}\pi^x(1-\pi)^{N-x}$$

If the frequency of occurrence of pixels in the seeds follows the binomial distribution, than DOTs have a random origin, but if a given pixel occurs in the seeds more often than expected from the binomial distribution, then we can consider it as a starter. We found that red pixels in **Figure 3C** occurred in seeds more often than expected by the binomial distribution in 6 out of 7 experiments (**Figure 3D**, **E**; $p < 0.001$ two-sample Kolmogorov-Smirnof test) and therefore are candidates to be starters of the DOTs. In order to identify the neuronal types composing these starter regions, we localized the GABAergic neurons in slices after binarizing the images in the green channel. After comparison with the location of starters in the same slice, we observed a minimal spatial overlap (**Figure 3F**), suggesting that starters might be composed by clusters of non-GABAergic, probably excitatory neurons. Moreover, a preferential localization of starters at 200 - 300 µm in depth from the outer most layer was observed, which corresponds approximately to layer III (**Figure 3G**).

COTs and DOTs in hippocampal networks: origin and comparison with the cortex

We analyzed the probability of existence of DOTs starters in hippocampal slices. In contrast with what seen in cortical slices, the frequency of pixel activation was similar to a theoretical Binomial Distribution in 3 out of 5 experiments (**Supplementary Figure 3**, $p > 0.05$ two-sample Kolmogorov-Smirnof test). The existence of

Table 1: Power law slopes of area distributions in the cortex and hippocampus.

	Connected Area	Detached Area
Cortex	2.24 ± 0.27	2.41 ± 0.56
Hippocampus	2.28 ± 0.26	2.47 ± 0.34

Values are expressed as absolute values, mean ± standard deviation. n = 16/8 cortical/hippocampal recordings in connected tissues; n = 6/6 cortical/hippocampal recordings in detached condition. The binning used for these calculations was 42.

starters in hippocampal slices is therefore less probable than in cortical ones. While the same clusters of neurons seem to be involved in the generation of a DOT in the cortex, in hippocampal networks DOTs are more likely to originate when a sufficient number of neurons - randomly distributed - are activated.

Comparing the distributions of area and duration of COTs in the cortex and hippocampus (**Figure 4A, B**) and the area distribution power law's slopes (**Figure 4C**), we did not observe significant differences. In addition, very similar distributions and power law slopes of optical signals were obtained after mechanical truncation of the connections between hippocampus and cortex (see **Table 1**). We next analyzed the duration and frequency of DOTs separately, in 7 representative brain slices that showed a sufficient number of DOTs, and that we were able to record in the cortical and the hippocampal region for the same time (i.e. 10 min) without incurring into dye - and phototoxicity-driven tissue damage. The distribution of the duration of DOTs shows that they last longer in the cortex (**Figure 4D**: 10.21 ± 0.32 s for cortex, 8.19 ± 0.43 s for hippocampus). On the other hand, the distribution of the Inter Event Intervals (IEIs) shows that hippocampal DOTs are more frequent (**Figure 4E**: 67.72 ± 4.88 s for cortex, 48.77 ± 6.23 s for hippocampus). These differences were statistically significant. Both distributions were fitted with appropriate exponential equations (see blue and red lines in **Figure 4D, E**).

Dissociated neuronal cultures

In order to understand if the native cyto - architecture of networks plays a role in determining the frequency, duration and synchronization of spontaneous events, we analyzed the spontaneous activity in dissociated cultures form the cortex and hippocampus of GAD67-GFP mice and compared it to the one observed in slices from the same tissues.

In dissociated cultures, formed by a single layer of cells, neuronal calcium transients have a typical sharp rising phase which is distinguished from those originating from glia cells (38). Dissociated cell cultures are known to exhibit a degree of synchronization depending on the density of the culture (39). In our experiments, we considered two culture densities: 500/800 cells/mm^2 (medium density, MD; **Figure 5A, B, E**) and 1000 cells/mm^2

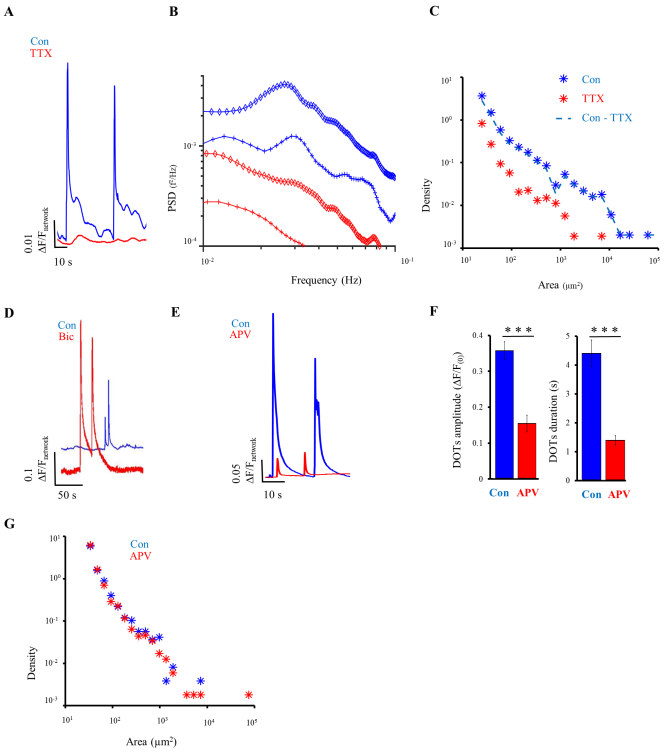

Figure 2: Blockade of voltage – gated sodium channels (by TTX) and glutamate NMDA receptors (by APV) on cortical slices. (A) DOTs observed in control conditions (blue trace) are abolished in the presence of 10 μM TTX (red trace), as shown by the computation of $\Delta F/F_{network}$. **(B)** Power Spectrum Density (PSD) computed as the average PSD of optical recordings from small regions corresponding to GABA+ neurons in control (blue traces) and in TTX (red traces) from two representative experiments (rhombus, 41 GABA+ neurons; crosses, 37 GABA+ neurons). **(C)** Density vs area of events in control (blue marks), in TTX (red marks) and in control-TTX (blue dotted line) in one experiment. From three representative experiments: n = 16714 events detected in Con, n = 14007 in Con-TTX; n = 68948 in Con, n = 53566 in Con-TTX; n=32312 in Con, n=21586 in Con-TTX ($p>0.05$ in all three cases, Kruskal-Wallis test). **(D)** $\Delta F/F_{network}$ in control conditions (blue trace) and after application of Bicuculline 50 μM (red trace). **(E)** $\Delta F/F_{network}$ in control conditions (blue trace) and after application of APV 50 μM (red trace). **(F)** Average amplitudes and duration of DOTs in control (blue bars) and in APV (red bars): 0.34 ± 0.03 $\Delta F/F_{(0)}$ and 4.33 ± 0.49 s for control, 0.15 ± 0.02 $\Delta F/F_{(0)}$ and 1.32 ± 0.16 s for APV. These average values were obtained from 3 experiments in control and APV conditions, subsequently: n = 32 (3) DOTs (slices) for control, n = 45 (3) DOTs (slices) for APV. *** $p < 0.001$ Kruskal Wallis test. **(G)** Density vs area of events in control (blue marks) and in APV (red marks) in a representative experiment.

or more (high density, HD; **Figure 5C, D, F**). **Figure 5** shows the results obtained from cortical cultures of GAD67-GFP mice, in which we could distinguish between GABA- and GABA+ neurons by comparing GFP-positive cells (**Figure 5B, D**) to those stained with the calcium sensitive dye only (**Figure 5A, C**), and separating the corresponding optical traces (**Figure 5E, F**). GABA- and GABA+ neurons are representative, with a good approximation, of the excitatory and the inhibitory population respectively.

We found different degrees of synchrony among the peaks of calcium transients in MD and HD cultures. We computed the mean cross-correlation among pairs of neurons $\rho(t)_{Peak}$ in a time window of 1 sec and we found that $\rho(t)_{Peak}$ was higher in HD than in MD cultures (0.604 ± 0.002 vs 0.337 ± 0.002, **Figure 5**G). However, in both cases the number of simultaneously active neurons over time showed periods of almost complete synchrony interspersed with epochs of very low coherent electrical activity (**Figure 5H**). The probability distribution of active neurons showed a power law behavior with slope-2 when the number of neurons were less than some tens: this distribution exhibited also outliers corresponding to the total number of neurons recorded, very similar to DOTs in slices (**Figure 5I**). We obtained similar results from dissociated hippocampal cultures (see **Supplementary Figure 4**). The average duration and IEI of these highly synchronous events - merging data from MD and HD cultures - were 3.31 ± 0.18 s and 24.99 ± 1.24 s, significantly decreased comparing to the DOTs observed in slices (**Figure 5L, M**). For this comparison, we used slices cultured in the same medium (Neurobasal/B27) used for dissociated cells, in order to avoid changes in neuronal synchronization due to the effect of different chemicals in the growing media (40).

These results suggest that DOTs are present both in native and in dissociated networks, and synchrony arises independently from the network architecture.

We aimed to investigate more in detail the spontaneous activity arising from GABAergic, inhibitory neurons. We found that an unequivocal distinction between GABA+ and GABA- neurons was possible only in dissociated MD cultures, in which neurons are not totally confluent. Thus, we compared calcium transients between GABA+ and GABA- neurons plated at a medium density and we found that the value of $\rho(t)_{Peak}$ - in a time window of 1 s - was higher in GABA+ than in GABA- neurons (**Figure 6A**). We asked whether large calcium transients were more correlated than smaller transients (41) and indeed calcium transients larger than 30% of the maximal amplitude observed in each trace were more correlated than the smaller ones (**Figure 6B**). After blockage of GABA-A receptors with 1 µM bicuculline, the amplitude of calcium

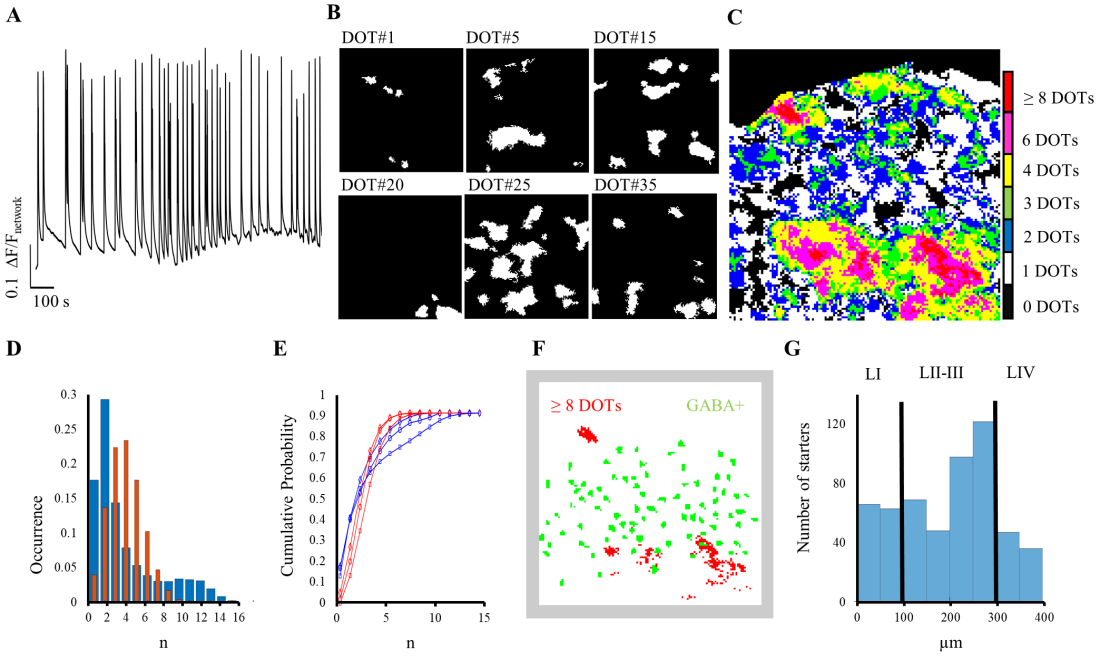

Figure 3: Regions initiating DOTs in cortical slices. (A) $\Delta F/F_{network}$ of a representative 20 min recording. **(B)** Binary images of some representative seeds regions identified 200 ms before 6 randomly selected DOTs (out of a total of 35). **(C)** Sum of all binary images corresponding to seeds; different colors indicate regions activated before multiple DOTs (see color bar on the right: red regions are activated before the onset of 8-11 DOTs). **(D)** Probability of activation of a pixel from experimental data (red bars) compared to a binomial distribution (blue bars) in the experiment shown in A - C. The x-axis represents the number of trials (frames) considered. **(E)** Cumulative probability of pixel activation from experimental data (blue lines) compared to the corresponding binomial distributions (red lines) in three representative experiments. The two distributions were significantly different ($p < 0.001$ two-sample Kolmogorov-Smirnof test). **(F)** Regions activated before the occurrence of 8 - 11 DOTs (red pixels) in the example shown in A - C, with reference to the location of GABA+ neurons (green pixels). **(G)** Distribution of starters location among cortical layers. n = 7 slices. The density is higher between LII and LIII.

transients became uniform in both populations (**Figure 6C**), however both the rising and falling phase of these transients were slower. Therefore we compared $\rho(t)_{Peak}$ in a time window of 10 s, which was consistently higher in GABA+ neurons even after the application of bicuculline (**Figure 6D**). The average IEI between peaks was significantly lower in the GABA+ population (**Figure 6E**), whereas the amplitude of $\Delta F/F_{(0)}$ was similar in GABA+ and GABA- neurons (**Figure 6F**). In order to identify possible delays in the transmission of excitatory and inhibitory signals, we repeated our imagingexperiments using an acquisition rate of 50 Hz but we did not detect any consistent delay between GABA+ and GABA- neurons at the available temporal resolution of 20 msec. Our results suggest that inhibitory GABA+ neurons have more synchronized and frequent spontaneous activity, in agreement with some previous *in vivo* observations (42).

Simplified models of neuronal networks

In order to understand the underlying mechanisms of the emergent dynamical properties, we explored highly simplified neural networks (**Figure 7A**), which have just 3-4 free parameters.This approach is complementary to those developed in current large projects such as the Blue Brain Project, Human Brain Project and Allen Brain Initiative where modeling involves an extremely large number of parameters, in the order 103 - 104 times more than in our simplified models. Our models are based on two major assumptions: firstly, dissociated neuronal cultures have a single layer organization, while cortical and hippocampal slices are multilayers; secondly some key factors, such as the threshold V_{th} and the number of connections per neurons NC, have a long-tailed distribution with a power law behavior. **Figure 7B** illustrates two representative models, while a detailed description is provided in the Methods section. The charges injected in the network at each time step mimic

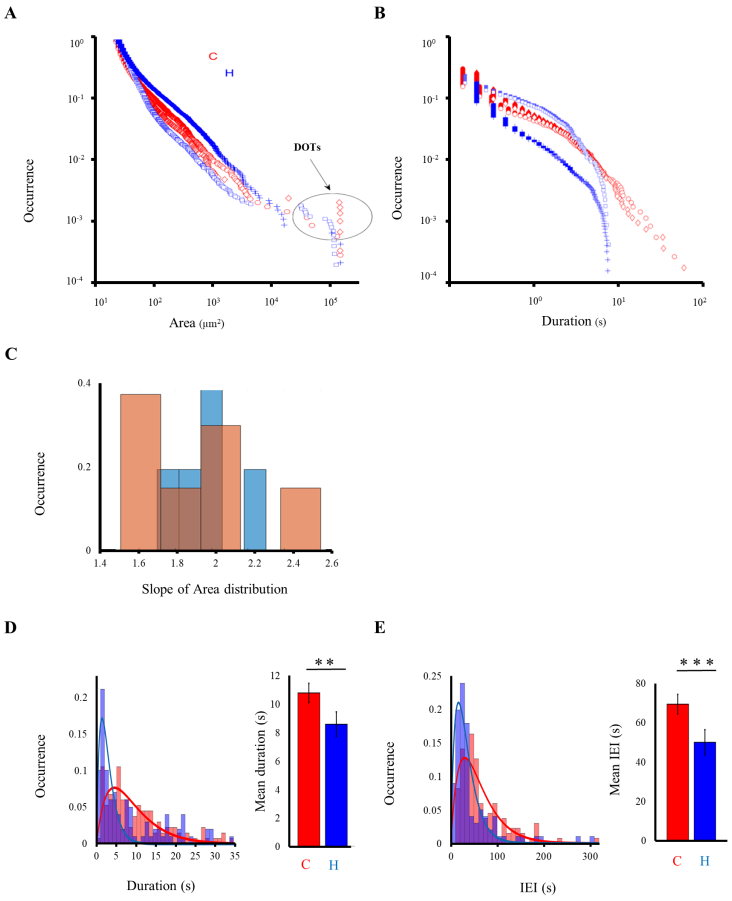

Fig. 4. Dynamics of cortical and hippocampal events compared. (A, B) Power law distributions of area and duration of COTs from four representative experiments with cortical events (C) marked in red, and hippocampal events (H) marked in blue. DOTs are represented as outliers outside the area's distributions (see black circle in A). The area distributions are power laws (power law hypothesis test p > 0.1) and display a slope close to 2. **(C)** Distribution of power law slopes for area in the cortex (red bars) and hippocampus (blue bars); n = 16 cortical recordings, n = 8 hippocampal recordings. **(D)** Distribution (left panel) and average values (right panel) of cortical (red bars) and hippocampal (blue bars) DOTs durations. The corresponding exponential fitting is f(x) = 0.05*x*exp(-x/4.54) for the cortex, f(x) = 0.33*x*exp(-x/1.39) for the hippocampus. **(E)** Distribution (left panel) and average values (right panel) of Inter Event Intervals (IEIs) in cortical (red bars) and hippocampal (blue bars) slices. The corresponding exponential fitting is f(x) = 0.011*x*exp(-x/33) for the cortex, f(x)=0.034*x*exp(-x/17)+0.58 for the hippocampus. n = 102/7 cortical DOTs/slices, n = 137/7 hippocampal DOTs/slices analyzed. $^{**}p < 0.01$, $^{***}p < 0.001$ Kruskal-Wallis test.

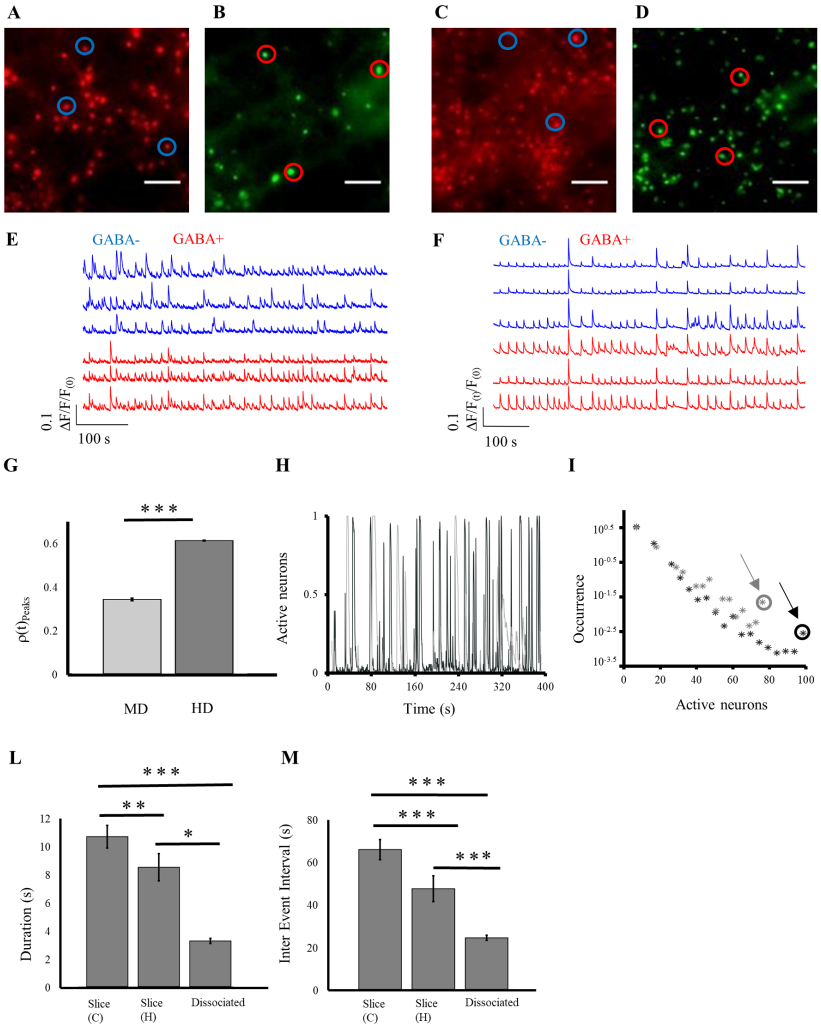

Fig. 5. Dissociated cortical cultures plated at high (HD) and medium (MD) density. (A, C) MD and HD cultures stained with Fura-Red calcium-sensitive dye. **(B, D)** Corresponding GABA+ neurons in the same field of view. From the neurons in the blue and red circles, the corresponding optical traces $\Delta F/F_{(0)}$ are shown in **(E, F)**: blue and red traces represent GABA- and GABA+ neurons respectively. Scale bars, 80 μm, in all fluorescence images. **(G)** Average $\rho(t)_{Peak}$ in MD (light gray) and HD (dark gray) cultures; n = 9354(3) pairs of neurons(sample) for HD, n = 1211(3) pairs of neurons(sample) for MD. **(H)** Activation of neurons over time in MD (gray) and HD (black) cultures, normalized to the total number of neurons (105 and 34 for HD and MD cultures, in this representative experiment). **(I)** Probability distribution of the number of neurons simultaneously active in MD (gray marks) and HD (black marks) cultures, with corresponding outliers (see circles). (**L, M**) Average duration and IEI (s) of DOTs in cortical (C) and hippocampal (H) slices (same data as in G, H, I) vs dissociated cultures. n = 78(4) DOTs(samples) for dissociated cultures. $^{*}p < 0.51$, $^{***}p < 0.001$ two-sided Wilcoxon rank-sum test.

random synaptic inputs received by the neurons. Model 1 and Model 2 of a single layer network have just 3 and 4 free parameters, respectively: the threshold V_{th}, the degree of connectivity NC, the strength of connectivity φ (only in Model 2) and the rate of dissipation λ. The dissipation λ represents all the biophysical processes reducing the excitation, such as the inhibitory inputs and all mechanisms associated to adaptation and desensitization. We found that when V_{th} is a random variable with a long tailed distribution, such as a power law of $\rho(V_{th}) = V_{th}^{-\alpha}$ ($\alpha < 2$), both Model 1 and Model 2 reproduce several of our experimental data. In fact, as experimentally observed, they reproduce a power law distribution of the number of simultaneously active neurons with a slope of about -2 (**Figure 7C**). These models reproduce also the system wide excitations corresponding to the experimentally observed DOTs. As we have a very limited number of parameters, we obtained state diagrams: in both models, DOTs appear when NC increases and λ decreases (**Figure 7D**). In order to explore the possibility that some of the emergent dynamical properties of slices are due to their multilayer functional/anatomical organization, we constructed models of multilayer networks in which, in addition to intra-layer connections, every neuron *i* has one connection to a neuron in the next layer (**Figure 7E**). Increasing the number of layers, the duration and Inter DOT Intervals of the simulated DOTs increased (**Figure 7F**).

We next compared the experimentally observed

dynamical properties of native and dissociated networks with the corresponding simulated networks. The results are recapitulated in **Figure 8** from the computation of optical traces $\Delta F/F_{network}$, and from the time series obtained with simulations. In both HD and MD cultures, $\Delta F/F_{network}$ has clear peaks but with a variable amplitude independently from the density of neurons (**Figure 8A**). A similar variability was obtained simulating a single layer network with Model 1 (**Figure 8D**). Experimentally, in the presence of Bicuculline, the peaks of $\Delta F/F_{network}$ have a more similar amplitude (**Figure 8B**), in line with the theoretical finding that decreasing the dissipation λ enhances the probability of DOTs appearance (**Figure 8E**). In slices, $\Delta F/F_{network}$ has less frequent peaks with a uniform amplitude and longer duration comparing to dissociated cultures (**Figure 8C**) - a pattern that is reproduced by our multilayer network as shown in **Figure 8F**. The DOTs experimentally observed in the cortex are longer than in the hippocampus (compare **Figure 8G and H**) and have a specific time course during which the initial peak is followed by a longer plateau, with some oscillations not seen in dissociated cultures from the same tissue. Our multilayer models reproduce the occurrence of DOTs with a time course reminiscent of that seen in cortical slices (**Figure 8I**). Moreover, networks with an increased number of layers exhibit longer but less frequent DOTs. This is true even if they have the same number of neurons.

Discussion

Our results show that the spontaneous activity in cortical and hippocampal slices is dominated by the intermittency between a regime where optical signals are confined in several small regions and a regime where there is a global activation invading almost the entire visualized network, referred to as DOTs. This type of synchronized calcium transients were previously demonstrated to correspond to the depolarizing envelopes of spontaneous oscillations known as Up states, as shown by the correlation between individual neuronal spikes and network-wide bursting events (20). We therefore suggest that the DOTs observed in our experiments correspond to the spontaneous Up states that were previously described as events propagating throughout the cortex (10, 12).

DOTs appear as strong and fast increase of $\Delta F/F_{network}$, in a way reminiscent of spike generation in a single neuron - that is triggered by a positive feedback due to the voltage-gated conductance. Thus, at the network level, DOTs represent a positive feed-back which has been historically proposed to be a fundamental mechanism of information processing in the brain and to be at the basis of learning, memory and recognition (43, 44).

DOTs were observed in all examined neuronal networks, in those preserving the original cyto-architecture and after dissociation of the native tissue as well. Our results, however, demonstrate for the first time that the duration and intensity of DOTs depend on the original cyto-architecture of the cortex and of the hippocampus and on the overall balance between excitation and inhibition, as indicated by the action of APV (blocking NMDA glutamate receptors) and Bicuculine (blocking GABAergic receptors). In all types of networks analyzed, we found that the area of spontaneous events follows a power law distribution, in agreement with previous studies (45, 46). The power law behavior seen in the distribution of maximal areas of spontaneous events

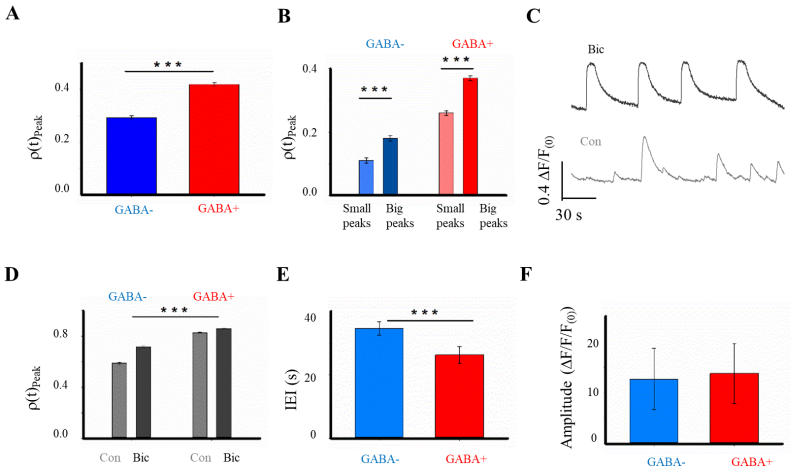

Fig. 6. Calcium transients from dissociated GABA+ and GABA- neurons. (A) Average $\rho(t)_{Peak}$, computed in 1 s time window, among pairs of GABA+ vs pairs of GABA- neurons in the network (0.420 ± 0.007 vs 0.294 ± 0.007, respectively). **(B)** Same as (A) distinguishing between small and big peaks (defined by a threshold equal to the 30% of the maximal amplitude observed in each trace: 0.370 ± 0.007 vs 0.181 ± 0.009 for GABA+ neurons; 0.263 ± 0.007 vs 0.110 ± 0.008 for GABA- neurons). n = 605(3) pairs of neurons(sample) for GABA+, n = 870(3) pairs of neurons(sample) for GABA-. **(C)** Representative $\Delta F/F_{(0)}$ traces in control and after application of bicuculline 1 μM. **(D)** Average $\rho(t)_{Peak}$ in control and after bicuculline application, in GABA+ and GABA- neurons, computed in a time window of 10 s (0.728 ± 0.006 and 0.865 ± 0.003 for GABA+ neurons in control and bicuculline conditions; 0.590 ± 0.007 and 0.828 ± 0.005 for GABA- neurons in control and bicuculline conditions). **(E)** Average IEI (s) between peaks of calcium transients in GABA+ and GABA- neurons (26.07 ± 2.13 vs 34.62 ± 2.62). **(F)** Average amplitude ($\Delta F/F_{(0)}$) in the two neuronal populations (0.14 ± 0.06 vs 0.13 ± 0.06). n = 73(3) neurons(sample) for GABA+, n = 105(3) neurons(sample) for GABA-). $^{***}p < 0.001$ One-Way ANOVA.

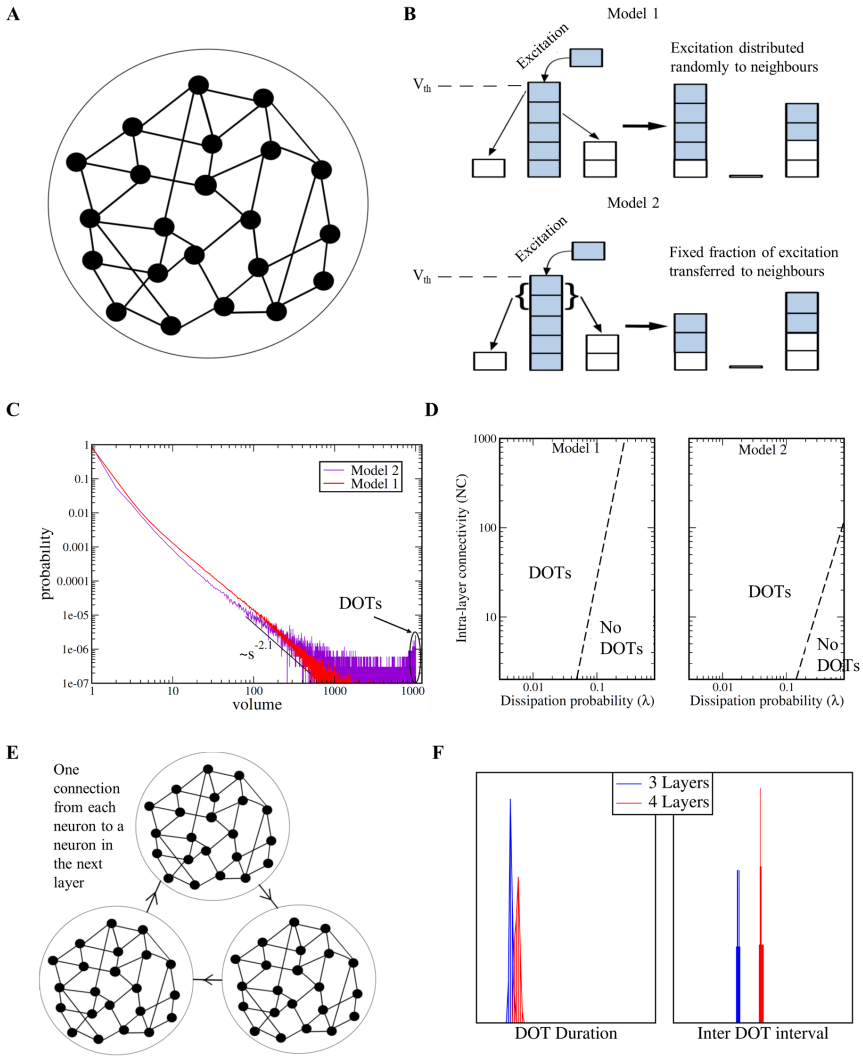

Fig. 7. Simulation setup and results. (A) Schematic diagram of the Single layer model of a network of N neurons with NC connections. **(B)** Schematic diagram of the mechanism of charge transfer in the two Models. **(C)** Distribution of avalanche volume for a network of N = 10,000 neurons in the two Models. **(D)** Phase diagram for the production of DOTs in terms of the dissipation and number of connections NC, for the two Models. The dashed line is indicative of the regime where DOTs disappear as one moves along either of the axis. **(E)** Schematic diagram of the multi-layer model. Each layer consists of N neurons with NC connections as before. However, now every neuron has one additional projection to the neurons in the next layer. **(F)** Distribution of DOT duration (defined in units of number of simultaneous DOTs in successive layers, which maps to number of DOTs times Δτ) and inter-DOT interval (defined in units of number of perturbations, i.e., simulation time steps) in a multilayer model with 3 layers (blue bars) as compared to one with 4 layers (red bars).

is in agreement with the predictions of the theory of Self Organized Criticality (47). This theory, however, assumes that the events under consideration are diluted in time and that only occasionally they occur simultaneously. Therefore, this central assumption of SOC does not hold for the optical transients observed in cortical and hippocampal slices, where we observed the simultaneous presence of tens of events at the same time.

In order to explain the experimental differences observed between the examined networks, we produced simplified models of neuronal networks with just 3/4 parameters. The proposed modeling with simplified neural networks is based on the analysis of the interplay between different mechanisms at the basis of the dynamics of neural networks, such as the threshold V_{th} for spike initiation, the degree of connectivity NC and the dissipation λ. Neurons in cortical and hippocampal networks experience a large amount of synaptic inputs leading to a fluctuation of their membrane potential (48). Therefore, in order to take these mechanisms into account, Vth is not fixed and follows a power law distribution. Both fixed and power law distribution of NC, instead, produce similar results in our model. However, experimental results support long-tailed and lognormal distributions of NC and synaptic strength at the level of local circuits (see for review (49)). Our modeling introduces a rate of dissipation λ of the charge accumulated in each neuron which has been inspired by statistical mechanics approaches (47, 50). This parameter is expected to describe in a lumped way some well-known mechanisms responsible for a time

dependent decrease of the excitation, such as synaptic negative feedback, receptor desensitization and ionic channels inactivation. The few parameters used in our models suffice to reproduce the observed intermittency and collective excitation at the single layer level. In particular, collective (DOT – like) excitations take place when a neuron with a very high charge fires, distributing all of its charge to the neighbours and triggering a global avalanche. These neurons present thresholds in the tail of the power law distribution of V_{th}. Another important component required to observe DOT - like events is a sufficiently low value of dissipation λ. Finally, in order to obtain DOTs with broad peaks like those seen in cortical/hippocampal slices, we need to introduce a multilayer architecture. The number of layers seems to determine the width and frequency of DOT - like events. In particular, networks with the highest number of layers exhibited longer but less frequent DOTs, in a way similar to what observed comparing cortical and hippocampal DOTs. This effect is not due to an increased number of total neurons in the network with more layers. We confirmed this result by simulating two networks with different numbers of layers, but the same number of neurons N. Multilayered networks might rather have a lower probability of relaxation - since two layers close to their critical state, i.e. the DOT, are more likely to be separated by bridging layers. In fact, we found that the network with more layers load a higher value of total charge before firing, not only creating broader but also less frequent DOTs.

Taken together, our findings provide new insights on the probability of neuronal avalanches that could be useful for the understanding of complex network disorders such as epilepsy. Large-scale models of hyperexcitable circuits, in fact, have been produced in order to predict the role of neuronal hubs in epileptic seizures (51). Our simplified models of networks represent an additional tool for simulating network disorders in brain regions with different functional and anatomical layers.

Conclusion

We assume that the experimentally observed differences in the frequency and duration of DOTs can be accounted for the presence of more anatomical/functional layers in cortical slices as compared to hippocampal slices, and in both type of slices as compared to dissociated cultures. We conclude that the network architecture and multilayer organization, together with the biophysical properties of neurons such as firing thresholds, connectivity, and degree of inhibition/desensitization, determine the emergent dynamical properties of the cortex and the hippocampus.

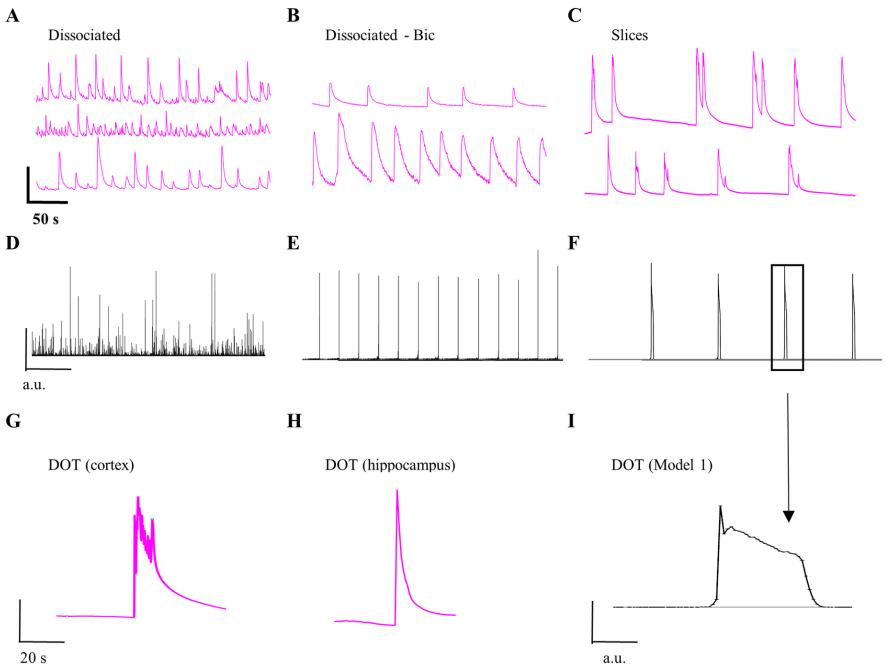

Fig. 8. Intermittency in dissociated and native networks and corresponding simulations. Experimental results are shown in purple, while time series obtained from the simulations are shown in black. **(A)** $\Delta F/F_{network}$ in dissociated MD/HD cultures. **(B)** $\Delta F/F_{network}$ in dissociated MD/HD cultures after application of Bicuculline 1 μM. **(C)** $\Delta F/F_{network}$ in some representative cortical slices. Scale bar, 0.1 $\Delta F/F_{network}$. **(D)** Time series of a single-layer network from Model1. **(E)** Time series from the same simulated network after decreasing λ. **(F)** Time series from a multilayer network from Model1. In these plots, the x-axis are in units of number of perturbations, i.e., simulation time steps Δτ (arbitrary units, a.u.). In the multilayer model, a Δτ of 50,000 perturbation steps have been used. **(G, H)** Enlarged DOTs from $\Delta F/F_{network}$ of experimental recordings in cortical and hippocampal slices, respectively. Scale bar, 0.1 $\Delta F/F_{network}$. (I) Enlarged DOT from the simulation of the multilayer network.

Acknowledgements
The authors would like to thank Michele Giugliano and Paolo Bonifazi for their useful comments on the early version of the manuscript.

Conflict of interest
Authors declare that there are no conflicts of interest.

Funding body
This work was supported by the 3315 project of Ningbo Institute of Materials Technology and Engineering, Chinese Academy of Sciences, Zhejiang province (China).

Supplementary Information
The supplemental material can be downloaded online at:
https://stemedicine.org/index.php/stem/article/view/1

References

1. Faisal AA, Selen LPJ, Wolpert DM. Noise in the nervous system. Nat Rev Neurosci. 2008 Apr;9(4):292-303.
2. Luczak A, Barthó P, Marguet SL, Buzsáki G, Harris KD. Sequential structure of neocortical spontaneous activity in vivo. Proc Natl Acad Sci USA. 2007 Jan 2;104(1):347-52.
3. Steriade M, Nuñez A, Amzica F. A novel slow (< 1 Hz) oscillation of neocortical neurons in vivo: depolarizing and hyperpolarizing components. J Neurosci. 1993 Aug;13(8):3252-65.
4. Timofeev I, Grenier F, Steriade M. Disfacilitation and active inhibition in the neocortex during the naturalsleep-wake cycle: an intracellular study. Proc Natl Acad Sci USA. 2001 Feb 13;98(4):1924-9.
5. Petersen CCH, Grinvald A, Sakmann B. Spatiotemporal dynamics of sensory responses in layer 2/3 of rat barrel cortex measured in vivo by voltage-sensitive dye imaging combined with whole-cell voltage recordings and neuron reconstructions. J Neurosci. 2003 Feb 15;23(4):1298-309.
6. Sachidhanandam S, Sreenivasan V, Kyriakatos A, Kremer Y, Petersen CCH. Membrane potential correlates of sensory perception in mouse barrel cortex. Nat Neurosci. 2013 Nov;16(11):1671-7.
7. Vyazovskiy VV, Olcese U, Hanlon EC, Nir Y, Cirelli C, Tononi G. Local sleep in awake rats. Nature. 2011 Apr;472(7344):443-7.
8. Engel TA, Steinmetz NA, Gieselmann MA, Thiele A, Moore T, Boahen K. Selective modulation of cortical state during spatial attention. Science. 2016 02;354(6316):1140-4.
9. Timofeev I, Grenier F, Bazhenov M, Sejnowski TJ, Steriade M. Origin of slow cortical oscillations in deafferented cortical slabs. Cereb Cortex N Y N 1991. 2000 Dec;10(12):1185-99.
10. Sanchez-Vives MV, McCormick DA. Cellular and network mechanisms of rhythmic recurrent activity in neocortex. Nat Neurosci. 2000 Oct;3(10):1027-34.
11. Fanselow EE, Connors BW. The roles of somatostatin-expressing (GIN) and fast-spiking inhibitory interneurons in UP-DOWN states of mouse neocortex. J Neurophysiol. 2010Aug;104(2):596-606.
12. Compte A, Reig R, Descalzo VF, Harvey MA, Puccini GD, Sanchez-Vives MV. Spontaneous high-frequency (10-80 Hz) oscillations during up states in the cerebral cortex in vitro. J Neurosci. 2008 Dec 17;28(51):13828-44.
13. Buzsáki G. Theta oscillations in the hippocampus. Neuron. 2002 Jan;33(3):325-40.
14. Sirota A, Buzsáki G. Interaction between neocortical and hippocampal networks via slow oscillations. Thalamus Relat Syst. 2005 Dec;3(04):245.
15. Markram H, Muller E, Ramaswamy S, Reimann MW, Abdellah M, Sanchez CA, et al. Reconstruction and simulation of neocortical microcircuitry. Cell. 2015 Oct;163(2):456-92.
16. Scarpetta S, de Candia A. Alternation of up and down states at a dynamical phase-transition of a neural network with spatiotemporal attractors. Front Syst Neurosci [Internet]. 2014 May 19;8:88.
17. Curto C, Sakata S, Marguet S, Itskov V, Harris KD. A simple model of cortical dynamics explains variability and state dependence of sensory responses in urethane-anesthetized auditory cortex. J Neurosci. 2009 Aug 26;29(34):10600-12.
18. Goodfellow M, Glendinning P. Mechanisms of intermittent state transitions in a coupled heterogeneous oscillator model of epilepsy. J Math Neurosci. 2013 Aug 14;3:17.
19. Tamamaki N, Yanagawa Y, Tomioka R, Miyazaki J-I, Obata K, Kaneko T. Green fluorescent protein expression and colocalization with calretinin, parvalbumin, and somatostatin in the GAD67-GFP knock-in mouse. J Comp Neurol. 2003 Dec 1;467(1):60-79.
20. Cossart R, Ikegaya Y, Yuste R. Calcium imaging of cortical networks dynamics. Cell Calcium. 2005 May;37(5):451-7.
21. Yang W, Yuste R. In vivo imaging of neural activity. Nat Methods. 2017 Mar 31;14(4):349-59.
22. Gähwiler BH, Capogna M, Debanne D, McKinney RA, Thompson SM. Organotypic slice cultures: a technique has come of age. Trends Neurosci. 1997 Oct;20(10):471-7.
23. Stoppini L, Buchs PA, Muller D. A simple method for organotypic cultures of nervous tissue. J Neurosci Methods. 1991 Apr;37(2):173-82.
24. Clauset A, Shalizi C, Newman M. Power-Law Distributions in Empirical Data. SIAM Rev. 2009 Nov 4;51(4):661-703.
25. Regad T, Bellodi C, Nicotera P, Salomoni P. The tumor suppressor Pml regulates cell fate in the developing neocortex. Nat Neurosci. 2009 Feb;12(2):132-40.
26. Douglas RJ, Martin KAC. Neuronal circuits of the neocortex. Annu Rev Neurosci. 2004;27:419-51.
27. Narahashi T, Moore JW, Scott WR. Tetrodotoxin Blockage of Sodium Conductance Increase in Lobster Giant Axons. J Gen Physiol. 1964 May 1;47(5):965-74.
28. Gilbride CJ. The hyperexcitability of dentate granule neurons in organotypic hippocampal slice cultures is due to reorganization of synaptic inputs in vitro. Physiol Rep. 2016 Oct 1;4(19):n/a-n/a.
29. Tamura A, Yamada N, Yaguchi Y, Machida Y, Mori I, Osanai M. Both neurons and astrocytes exhibited tetrodotoxin-resistant metabotropic glutamate receptor-dependent spontaneous slow Ca2+ oscillations in striatum. PLOS ONE. 2014 Jan 15;9(1):e85351.
30. Mazzoni A, Broccard FD, Garcia-Perez E, Bonifazi P, Ruaro ME, Torre V. On the dynamics of the spontaneous activity in neuronal networks. PLoS ONE. 2007 May 9;2(5):e439.
31. Cossart R, Aronov D, Yuste R. Attractor dynamics of network UP states in the neocortex. Nature. 2003 May 15;423(6937):283-8.
32. Mao B-Q, Hamzei-Sichani F, Aronov D, Froemke RC, Yuste R. Dynamics of spontaneous activity in neocortical slices. Neuron. 2001 Dec;32(5):883-98.
33. Piet R, Jahr CE. Glutamatergic and purinergic receptor-mediated calcium transients in Bergmann glial cells. J Neurosci. 2007 Apr 11;27(15):4027-35.
34. Rojas A, Wetherington J, Shaw R, Serrano G, Swanger S, Dingledine R. Activation of group I metabotropic glutamate receptors potentiates heteromeric kainate receptors. Mol Pharmacol. 2013 Jan;83(1):106-21.
35. Sengupta M, Thirumalai V. AMPA receptor mediated synaptic excitation drives state-dependent bursting in Purkinje neurons of zebrafish larvae. eLife. 2015 Sep 29;4:e09158.
36. Parga N, Abbott LF. Network model of spontaneous activity exhibiting synchronous transitions between up and down states. Front Neurosci. 2007 Oct 15;1(1):57-66.
37. Wadsworth GP, Bryan JG. Introduction to probability and random variables. McGraw-Hill; 1960. 312 p.
38. Charles AC, Merrill JE, Dirksen ER, Sanderson MJ. Intercellular signaling in glial cells: calcium waves and oscillations in response to mechanical stimulation and glutamate. Neuron. 1991 Jun;6(6):983-92.

39. Ito D, Tamate H, Nagayama M, Uchida T, Kudoh SN, Gohara K. Minimum neuron density for synchronized bursts in a rat cortical culture on multi-electrode arrays. Neuroscience. 2010 Nov 24;171(1):50-61.
40. Pozzi D, Ban J, Iseppon F, Torre V. An improved method for growing neurons: Comparison with standard protocols. J Neurosci Methods. 2017 Mar;280:1-10.
41. Ulloa Severino FP, Ban J, Song Q, Tang M, Bianconi G, Cheng G, et al. The role of dimensionality in neuronal network dynamics. Sci Rep. 2016 Jul 11;6:29640.
42. Gentet LJ, Avermann M, Matyas F, Staiger JF, Petersen CCH. Membrane potential dynamics of GABAergic neurons in the barrel cortex of behaving mice. Neuron. 2010 Feb;65(3):422-35.
43. Fukushima K. A hierarchical neural network model for associative memory. Biol Cybern. 1984 Apr 1;50(2):105-13.
44. Rolls ET. Cerebral cortex: principles of operation. First edition. Oxford New York, NY: Oxford University Press; 2016. 958 p.
45. Beggs JM, Plenz D. Neuronal avalanches in neocortical circuits. J Neurosci. 2003 Dec 3;23(35):11167-77.
46. Klaus A, Yu S, Plenz D. Statistical analyses support power law distributions found in neuronal avalanches. PLoS ONE. 2011 May 26;6(5):e19779.
47. Bak P, Tang C, Wiesenfeld K. Self-organized criticality: an explanation of the 1/f noise. Phys Rev Lett. 1987 Jul 27;59(4):381-4.
48. Hu W, Bean BP. Differential control of axonal and somatic resting potential by voltage-dependent conductances in cortical layer 5 pyramidal neurons. Neuron. 2018 Mar 21;97(6):1315-1326.e3.
49. Schröter M, Paulsen O, Bullmore ET. Micro-connectomics: probing the organization of neuronal networks at the cellular scale. Nat Rev Neurosci. 2017;18(3):131-46.
50. Marsili M, Valleriani A. Self Organization of Interacting Polya Urns. Eur Phys J B. 1998 Jul;3(4):417–20.
51. Morgan RJ, Soltesz I. Nonrandom connectivity of the epileptic dentate gyrus predicts a major role for neuronal hubs in seizures. Proc Natl Acad Sci USA. 2008 Apr 22;105(16):6179-84.

RESEARCH ARTICLE

ML-SA1, a TRPML1 agonist, induces gastric secretion and gastrointestinal tract inflammation *in vivo*

Dan GONG[#], Jing HAI[#], Jun MA, Chen-Xi WANG, Xin-Dan ZHANG, Ya-Nan XIANG, Tao TAN, Ya-Nan LIU, Wei Kevin ZHANG[*]

Institute of Pharmacology, College of Pharmaceutical Sciences, South-Central University for Nationalities, Wuhan, China
[#] These authors contributed equally to this work.

*Correspondence: wkzhang81@139.com
https://doi.org/10.37175/stemedicine.v1i1.3

ABSTRACT

Background: The effect of ML-SA1, a potent and specific TRPML1 channel agonist, on gastric secretion and subsequent impact to the gastrointestinal (GI) tract of mice was investigated.

Methods: Twenty mice were divided into two groups, and were treated with ML-SA1 and dimethyl sulfoxide (as negative control), respectively. The intestinal propulsion rate of the mice was monitored. Stomach and intestinal tissues were sectioned for periodic acid Schiff (PAS), histopathological and immunohistochemical (IHC) analysis. TRPML1 expression level in AGS cells was assayed via Western blot, and calcium imaging was performed in AGS cells upon performing GCaMP5G transfection.

Results: Application of 150 μg/kg ML-SA1 could result in significant decrease in intestinal propulsion rate and structural changes of the parietal cells in stomach and goblet cells in intestine of mice. Moreover, it induced inflammation to the duodenum section of intestine in mice. IHC staining also revealed that ML-SA1 could induce up-regulation of TRPML1 expression in both the parietal cells of stomach pits and the columnar epithelial cells of duodenum villi. Further analysis of AGS cells, a type of stomach cell line, demonstrated that ML-SA1 could enhance the expression of TRPML1 and induce the protrusion of micro-vesicles.

Conclusion: Our results suggested that ML-SA1 was capable of activating TRPML1 in stomach cells and therefore, leading to increased secretion of gastric acid. This provided a convincing attempt of applying ML-SA1 in animals and pointed out a new possible research direction, that TRPML1 channel could be a potential new therapeutic target on hypochlorhydria or even in the field of gastrointestinal cancer research.

Keywords: Mucolipin-1 · Hypochlordria · Gastric cells · Goblet cells · Calcium · COX-2

Introduction

Gastric acid, which is secreted by the stomach, is mainly composed of hydrochloric acid and divalent ions including potassium and sodium. Current understanding has shown that it is primarily produced by the parietal cells that line the stomach, and plays an initiative role in food digestion and pathogen protection in the gastrointestinal (GI) tract (1). Hence the lack of gastric acid production, or sometimes referred to as hypochlorhydria (achlorhydria or low stomach acid as well), would lead to malnutrition. In addition, hypochlorhydria has been implicated to be correlated with various disorders in the GI tract including pernicious anemia, *Helicobacter pylori* (*H. pylori*) infection, vipomas, hypothyroidism, and gastric cancer. The deficiency is also present in patients who have anti-secretory medications, gastric bypass, and radiation to the stomach (1-3). Currently, there is no specific treatment that targets hypochlorhydria. Instead, multiple case-dependent treatments have been used to reduce the complications of hypochlorhydria. For instance, *H. pylori* eradication has been instructed to patients after the infection. Increased uptake of calcium, iron, and/or vitamin D have also been suggested to hypochlorhydria patients (4).

A recent research has demonstrated that TRPML1 (also named mucolipin-1), a protein that is mutated in type-VI mucolipidosis (ML-IV), could be essential for

tubulovesicles (TV) exocytosis and acid secretion in parietal cells (5). TRPML1 is a non-selective cation channel primarily localized in the late endo-lysosome compartment (6). It belongs to the TRP channel superfamily and is an inwardly rectified channel capable of transporting ordinary cations such as Na^+, K^+ and Ca^{2+} (7), as well as some heavy metal ions such as Fe^{2+} and Zn^{2+} (8), from the extracellular space or the lumen of the lysosome to the cytosol (9). Many investigations have suggested that the abnormality (loss or down-regulation) of TRPML1 function could result in an accumulation of heterogeneous materials within lysosomes (10) and affect the regulation of lysosome motility, positioning and tubulation (11). Such changes in turn are hypothesized to affect many intracellular processes including membrane trafficking, phagocytosis and vesicular fusion and fission (12).

In this study, we aimed to investigate whether ML-SA1, a specific TRPML1 agonist (13), could induce acid production and secretion to the stomach in a mouse model. Moreover, we also wanted to evaluate the potency of ML-SA1 and the direct consequence of its application in the GI tract *in vivo*.

Materials and Methods

Reagents

Dimethyl sulfoxide (DMSO, #D5879) of analytical reagent grade was obtained from Sigma-Aldrich (St Louis, MO, USA). ML-SA1 was provided by Abcam (#ab144622, UK).

Animal care

The experimental protocols and animal care and utilization were implemented on the basis of the Guide for Nationalities and the Committee of Research Facilities for Laboratory Animal Sciences, South-Central University for Nationalities, China. The Committee on the Ethics of Animal Experiments of the South-Central University for Nationalities, China (permit number: 2018-SCUEC-AEC-011) developed related protocols. A great effort in minimizing suffering contained anesthesia by CO2 before sacrifice.

Cell culture and transfection

AGS cells (#CRL-1739, ATCC) were purchased and maintained as described by the instructions. F-12K medium (30-2004, ATCC) was used for maintenance of normal culture, with fetal bovine serum (FBS, Gibco, Thermo Fisher Scientific) being added to a final concentration of 10%. Hieff Trans liposomal transfection reagent (#40802ES02, Yeasen Inc. China) was used for transfection. pCMV-GCaMP5G plasmid (#31788) was obtained from Addgene.

Intestinal propulsion rate testing

Prior to experiment, twenty female Kunming mice (8 weeks old, 20-22 g) were acclimatized for 4 days in pathogen-free conditions. Experimental animals were maintained with basal diet. They were also kept in temperature-controlled animal room (22-25℃) with at least 4 rounds of 12 h light-dark cycle before experiments. During acute experiments, the animals were divided into two groups of 10 mice each at random. The treatment group received 150 μg/kg ML-SA1 while the control group received 150 μg/kg DMSO. Both groups received their respective drug every 12 h for 3 times by gavage. Mice were fasted overnight, and then received an oral administration of 200 μl/animal carbonic ink. Fifteen min later, animals were euthanized by cervical dislocation. The stomach and the complete intestinal tract from the pylorus to the terminal rectum were removed. The length of the whole intestinal tract and the distance of ink propulsion were measured. The percentage of blackened intestinal tracts was calculated using the following equation: intestinal propulsion rate (%) = pushing length/ total length × 100%.

Histopathological analysis of tissues

Fresh stomach and intestines tissue samples were fixed in 4% polyformaldehyde, embedded in paraffin, cut into 2 μm slices. Standard techniques were used for staining with hematoxylin and eosin (H&E) or hematoxylin alone. Histopathologic examination of the sections was conducted using a Nikon 50i light microscope (Nikon Inc.).

Immunohistochemical (IHC) analysis of tissues

The tissue sections were deparaffinized and hydrated. The sections were then immersed in 0.01 M boiling citrate buffer and were heated using a microwave oven for 5 min for antigen retrieval. Incubation with 3% hydrogen peroxide in methanol for 10 min was performed to block endogenous peroxidase activity. After blocking with 5% serum (AR1009, AR1010; Boster, China) for 1 h, the sections were incubated overnight at 4°C with primary antibodies against TRPML1 (1:200, ab28508; Abcam, UK) or COX-2 (1:100, ab23672; Abcam, UK). After incubation with IgG secondary antibodies (414341C, 414351C, Nichirei, Japan) at 37°C for 1 h, the presence of TRPML1 was detected using the DAB detection kit (425314F, Nichirei, Japan). Sections were counterstained with hematoxylin and coverslips were used for mounting.

Periodic Acid Schiff (PAS) Staining

The samples were sectioned and placed on slides, which were then deparaffinized, rehydrated, oxidized (1% periodic acid for 15 min), washed by distilled water and stained with Schiff's reagent for 30 min. Then the sections were washed with hydrochloric acid and H_2O for 2 min and three times, followed by immersing in tap water for 5 min. Finally, the sections were counterstained with hematoxylin for 20 seconds and dehydrated.

Western blotting

After treatment, cells were lysed with RIPA protein lysis buffer (Beyotime, China) containing phosphatase inhibitor

cocktail (100x) (Cwbio, China), protease inhibitor cocktail (100x) (Cwbio, China) and phenylmethylsulfonyl fluorid (Beyotime, China). The concentration of total protein was detected by the Lowry method. Equal amounts of protein were fractionated by 12.5% sodium dodecyl sulfate polyacrylamide gels and transferred to polyvinylidene difluoride membranes (Millipore Corporation, USA). After blocked with 5% nonfat dry milk, the membranes were incubated with anti-TRPML1 antibody at 4°C overnight. To remove unbound primary antibodies, the membranes were washed 3 times for 5 mins by TBST (Tris-Buffered Saline, 0.1% Tween-20) solution and followed by exposure to secondary antibodies (1:3000, goat anti-rabbit, Abbkine, USA) for 1 h at room temperature. Finally, after wash, bands on the membranes were visualized by developer and fixing solution. The protein bands were quantified using the ImageJ software.

Fluorescent microscopy

Fluorescent signals from GCaMP5G protein were excited with a FITC filter (Ex 465-495, Dm 505, RA 512-558, Nikon) and were collected using an inverted microscope (Eclipse Ti, Nikon) with a color camera (DS-Ri2, Nikon). ImageJ (NIH) software was used to quantify and analyze the obtained signal.

Statistical analysis

All results were presented as mean ± SEM. Prism 7 were used for the storage and analysis of data. Student's t-test was performed to compare the difference of groups and the p value was indicated in the graph. Statistical differences of $p < 0.05$ were considered to be significant.

Results

Application of ML-SA1 reduced intestinal propulsion rate in mice.

Gavage application of TRPML1 agonist, ML-SA1 (**Figure 1A**, 150 μg/kg, thrice prior to the intestinal propulsion rate test) resulted in a significant decrease in the propulsion rate in mice (**Figure 1C** and **D**), from 55.0 ± 9.0 cm in vehicle-treated group to 41.6 ± 7.5 cm in ML-SA1-treated group. This hold-back effect of ML-SA1 could normally even be greater, taking into consideration that there was only a 15-min gap between the gavage application and sacrifice of mice.

Application of ML-SA1 altered the structure in stomach and duodenum of mice.

After the above experiment, we sacrificed the animal and took the stomach and duodenum out to further characterize the changes caused by ML-SA1 to the mice. H&E staining revealed that application of 150 μg/kg ML-SA1 altered the structure of stomach pits and duodenum villi. As shown in **Figure 2A**, the integrity and order of the pits remained in the stomach of mice. However, more parietal cells were observed in the upper edge of pits in stomach of ML-SA1 treated mice. More importantly, the shape of parietal cells became smaller and more vacant in ML-SA1-treated mice comparing with that of vehicle-treated ones, suggesting that ML-SA1 might stimulate the exocytosis process of parietal cells, resulting in increased hydrogen chloride secretion in the stomach. In addition, less goblet cells were present in the villi of duodenum after the treatment of ML-SA1 (**Figure 2B**), further strengthening the notion that more protons were present in the gastric juice, since one of the functions of goblet cells is to secrete enough water and mucous to counteract the damage of low pH gastric juice to the intestine. To further confirm the observed phenomena, PAS staining was performed as shown in **Figure 3A** and **B**. We can see from the graph that the amount of goblet cells was not significantly decreased in the duodenum sections of ML-SA1-treated mice. However, the stained sizes of goblet cells were drastically reduced, suggesting that majority of intracellular contents had been secreted. This is in accordance with the former observations that the acidity of gastric juice was increased.

Application of ML-SA1 induced inflammation in the duodenum of mice.

A common consequence of gastric juice acidification is increased inflammation of duodenum. To verify whether ML-SA1 induced gastric acid secretion, COX-2, an inflammation marker and inducer, was stained and quantified in the duodenum section of mice. As demonstrated in **Figure 3C** and **D**, a heavier staining of COX-2 were observed in the duodenum sections of ML-SA1 treated mice. In addition, COX-2 expression was mostly seen in the upmost region pointing towards the lumen of duodenum, which advised that the elevation of inflammation was restricted to the inner surface intestine.

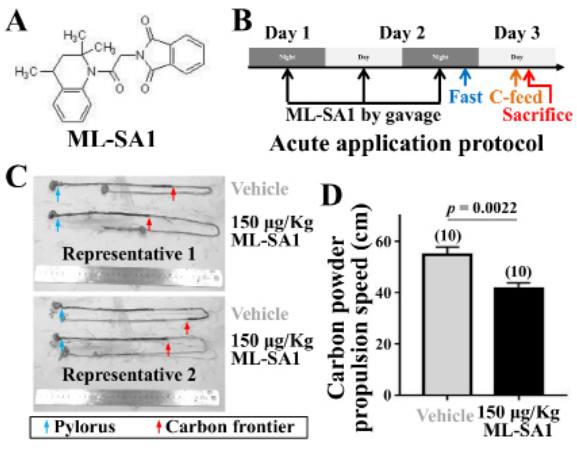

Figure 1. ML-SA1 treatment slowed Intestinal propulsion rate in mice. (A) The chemical structure of ML-SA1. (B) The detailed protocol of applying ML-SA1 (150 μg/kg, dissolved in DMSO as 10 mM stock) to mice. (C) Representatives of the intestinal propulsion rate test. Blue arrow, the beginning of length measurement; Red arrow, the end of length measurement. (D) Summary of (C). Numbers in the brackets indicated the number of mice used. Data were presented as mean ± SEM.

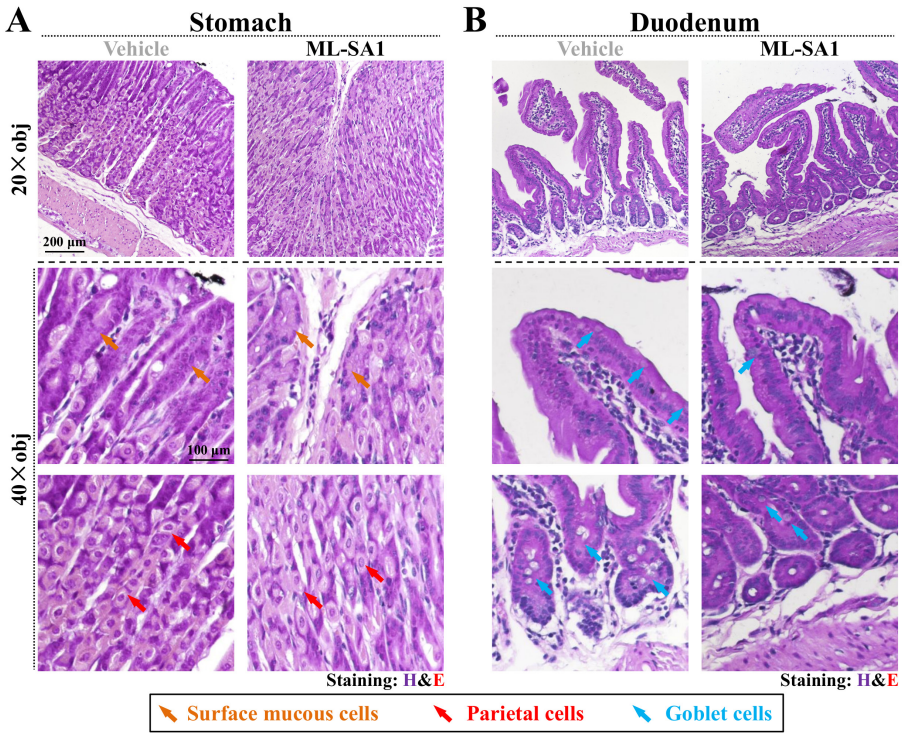

Figure 2. ML-SA1 treatment altered the morphology of stomach and duodenum of mice. (A) The H&E staining of stomach sections from the vehicle-treated or ML-SA1-treated mice. Orange arrow, surface mucous cells lining the up-edge of the pits; Red arrow, parietal cells lining the medium parts of the pits. Scale bar, 200 μm for the 20× objective lens and 100 μm for the 40× objective lens. (B) The H&E staining of duodenum sections from the vehicle-treated or ML-SA1-treated mice. Blue arrow, goblet cells in the villi of intestine.

Application of ML-SA1 increased the expression of TRPML1 in the GI tract of mice.

ML-SA1 has been used as a specific TRPML1 channel agonist. Therefore, TRPML1 levels were assayed and monitored in both the stomach and duodenum sections of the mice. We can see that the expression of TRPML1 was specific, with TRPML1 mainly being observed in the parietal cells of stomach pits and in the columnar epithelial cells of duodenum villi (**Figure 4A** and **B**). The expression of TRPML1 was largely elevated in ML-SA1-treated mice. It is also interesting to note that the pattern of TRPML1 expression was restricted as round circles inside cells, consistent with the previous observations that TRPML1 was mostly located in lysosomes and endosomes, but not on the plasma membrane of cells (10). This piece of evidence also pointed out the specificity of TRPML1 antibody since no staining was observed in other regions of the samples. Another meaningful finding was that TRPML1 was only observed in shrunken goblet cells in the duodenum but not in goblet cells possessing a round bubble, suggesting that the elevation of TRPML1 function would indeed increase the secretion of goblet cells in the intestine. Staining of the esophagus sections was used as a demonstration of efficacy of ML-SA1 on TRPML1 channel expression (**Figure 4C**).

Application of ML-SA1 promoted TRPML1 expression and cytosolic calcium concentration in AGS cells.

AGS cells, a stomach cell line, were used to demonstrate the aforementioned effect of ML-SA1 on the stomach. Various concentrations of ML-SA1 could induce a gradient rise of TRPML1 expression, as shown in **Figure 5A**. GCaMP5G, an exogenously expressed calcium sensor, was transfected into AGS cells. 20 μM ML-SA1 successfully triggered an elevation of intracellular calcium concentration in AGS cells. More importantly, micro-vesicles could be seen in **Figure 5B**, suggesting that ML-SA1 treatment might increase the exocytosis of AGS cells. Therefore, it would not be surprising to see an increased secretion of gastric juice in the stomach of mice after the application of ML-SA1.

Discussions

In this study, we demonstrated that gavage application of ML-SA1, a specific potent agonist of TRPML1 channel, could result in the enhancement of gastric acid secretion in the stomach of mice. As mentioned, a specific treatment of hypochlorhydria is lacking currently. Our research has highlighted a potential therapeutic agent that could be used for the treatment of hypochlorhydria. However, the following points are needed to be clarified first. We focused on the effect of ML-SA1 on GI tract in this study.

As shown in **Figure 4**, the expression of TRPML1 channel was also elevated in the epithelia layer by the application of ML-SA1. The exact function of TRPML1 in the epithelia layer has not been established, and more investigations are needed to evaluate the safety of ML-SA1 in respect to other organs and tissues. In regards to the appropriate dosage of ML-SA1 to administer to hypochlorhydria patients, we hypothesize that 16.5 μg/kg would be a suitable dose based on the dosage given to mice. We observed that decreased pH in gastric juice caused an inflammation in the duodenum section of mice. This could be explained by the fact that normal mice were used instead of mice suffering from hypochlorhydria during the whole experiment. Therefore, efficacy and safety should be paid special attention to when ML-SA1 is introduced to mouse model of hypochlorhydria and subsequently human patients, since whether TRPML1 is still presented in the parietal cells during hypochlorhydria condition remains to be elucidated.

TRPML1 channel was believed to be a widely expressed protein in all tissues and cells. However, in our experiment, we found that this is not the case. In **Figure 4**, TRPML1 protein is only presented in parietal cells and columnar epithelial cells, but not in the surface mucous cells in the stomach or connective tissues in the duodenum. It could be possible that normal expression of TRPML1 is relatively low in many cell types, and therefore, IHC staining is not sensitive enough to detect it. However, it might be precisely regulated during physiological and pathological conditions, therefore application of ML-SA1 could result in an increased TRPML1 expression. Moreover, the specificity of a certain cell type towards ML-SA1 could be a sign of importance of TRPML1 function in that particular cell type. For example, the fact that ML-SA1 induced increased TRPML1 expression in parietal cells and epithelium suggests that, normal function of TRPML1 might play a role in these cells. Taken into account the fact that the application of ML-SA1 led to a loss of intracellular content rather than a loss in the number of goblet cells, we speculate that TRPML1 could be a regulator of cellular exocytosis. As shown in **Figure 5**, ML-SA1 could indeed increase the expression level of TRPML1 channel, and upon its application increase cellular calcium concentration drastically.

Considerably, activation of TRPML1 via ML-SA1 initiated the formation of micro-vesicles in AGS cells, a stomach cell type, which further strengthened the notion that TRPML1 could regulate the exocytosis process of cells. This change happened relatively fast, since vesicles could be visualized only a couple of minutes upon the application of ML-SA1. Calcium has been closely correlated with cellular trafficking including endocytosis and

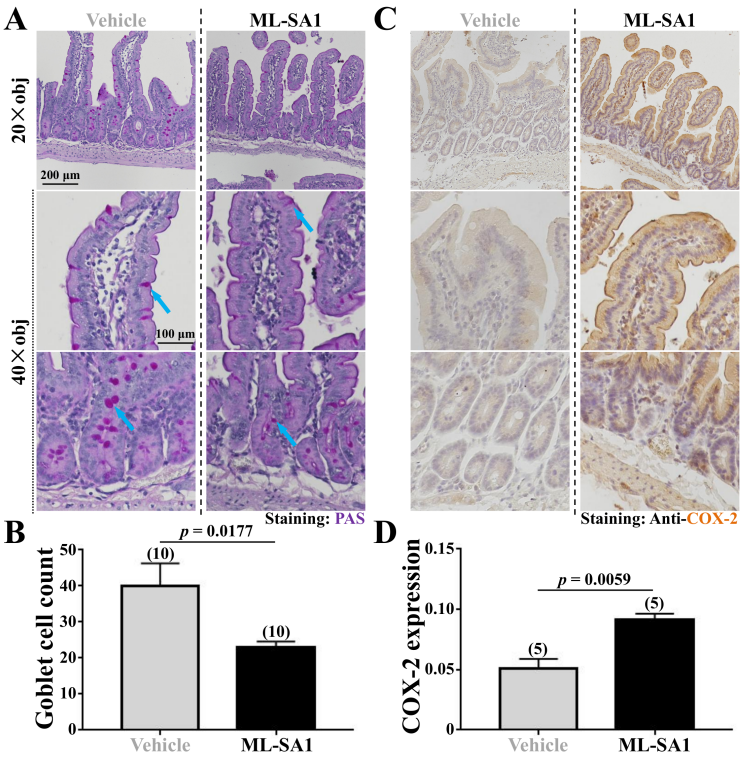

Figure 3. ML-SA1 treatment decreased the amount of goblet cells and induced inflammation in duodenum of mice. (A) PAS staining of duodenum sections from the vehicle-treated or ML-SA1-treated mice. Blue arrow, goblet cells that stained heavier. Scale bar, 200 μm for the 20× objective lens and 100 μm for the 40× objective lens. (B) Summary of (A). Numbers in the brackets indicated the number of sections from mice used. Data were presented as mean ± SEM. (C) Immuno-histochemical staining of duodenum sections from the vehicle-treated or ML-SA1-treated mice. Scale bar, the same as (A). (D) Summary of (C). Numbers in the brackets indicated the number of sections from mice used. Data were presented as mean ± SEM.

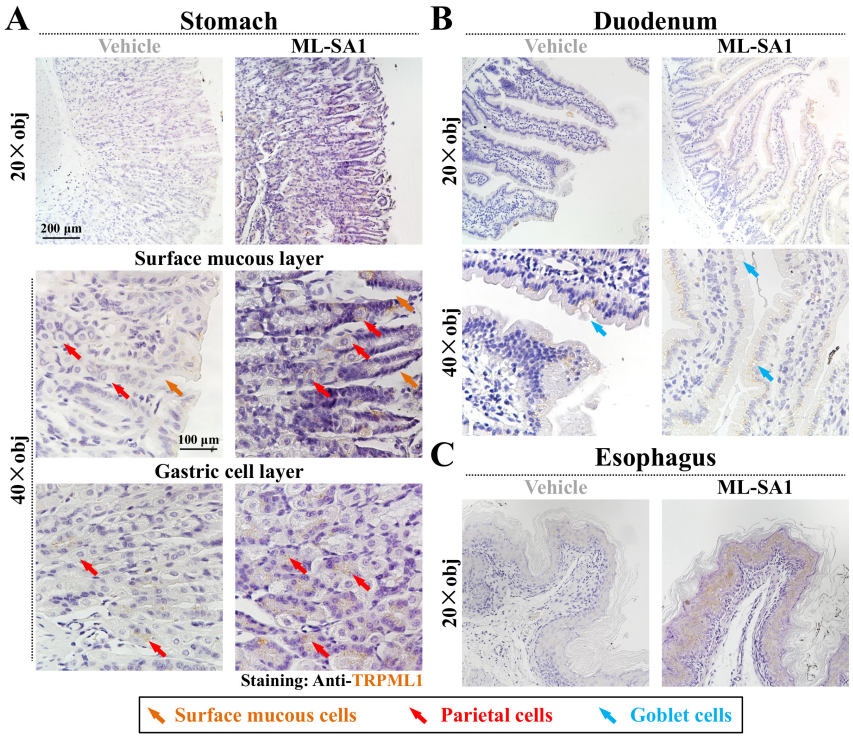

Figure 4. ML-SA1 treatment induced the expression of TRPML1 in vivo. (A) Immuno-histochemical staining of stomach sections from the vehicle-treated or ML-SA1-treated mice. Orange arrow, surface mucous cells lining the up-edge of the pits; Red arrow, parietal cells lining the medium parts of the pits. Scale bar, 200 μm for the 20× objective lens and 100 μm for the 40× objective lens. (B) Immuno-histochemical staining of duodenum sections from the vehicle-treated or ML-SA1-treated mice. Blue arrow, goblet cells. Scale bar, the same as (A). (C) Immuno-histochemical staining of esophagus sections from the vehicle-treated or ML-SA1-treated mice. Scale bar, 200 μm for the 20× objective lens.

exocytosis (14). As a non-selective cation channel, TRPML1 is capable of transporting calcium from intracellular organelles into the cytosol (15). Therefore, it would not be too surprising to see an increased rate of exocytosis after the activation of TRPML1 by ML-SA1. While we only observed such phenomena in the gastric cell lines, it would also be interesting to test whether activation of TRPML1 could induce secretion in other cell types, especially in cells that intrinsically reside in endocrine tissues. Meanwhile, more investigations might be helpful to understand the detailed roles of TRPML1 during the secretion of cells.

Hypochlorhydria has been closely associated with, and has been suggested to be a hallmark symptom of gastric cancer. Currently, little is known about the causality between the two due to the lack of a specific activator of gastric juice production. Moreover, considering the recent discoveries that TRPML1 had been correlated with cancerous conditions (16-18), and that the activation of TRPML1 could be important for eliminating H. pylori (19), it would be plausible to further study the effect of ML-SA1 in various pathological conditions of stomach or even the GI tract. Doing so might allow us to further establish the correlations between TRPML1 and gastric cancer. In conclusion, our study provided a convincing attempt of applying ML-SA1 in animals, and pointed out a new possible research direction that TRPML1 channel could be a potential new therapeutic target in hypochlorhydria or even in the field of gastrointestinal cancer research.

Conflict of interest
The authors declare that they have no competing interests.

Availability of data and material
The datasets used and/or analyzed during the current study are available from the corresponding author on reasonable request.

Consent for publication
All authors have agreed to publish this article.

Funding
This work was supported by the National Natural Science Foundation of China (31400705) and Fundamental Research Funds for the Central Universities (CZY19027).

References
1. Fatima R, Aziz M. Achlorhydria. StatPearls. Treasure Island (FL)2019.

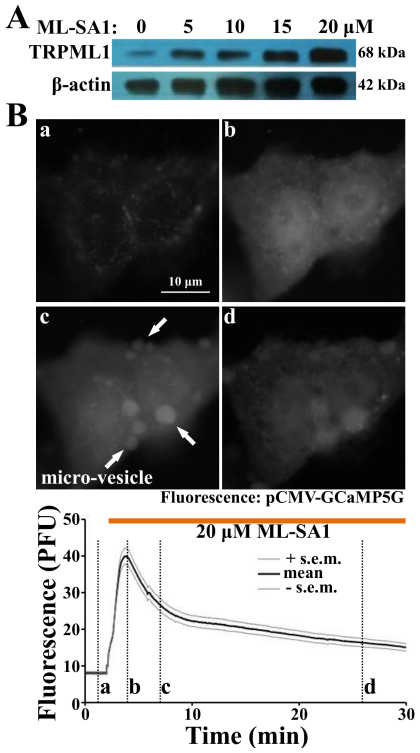

Figure 5. ML-SA1 activated TRPML1 in AGS cells. (A) Western blot of the TRPML1 expression in AGS cells after the application of various concentrations of ML-SA1. (B) The cytosolic calcium concentration change in calcium sensor transfected AGS cells after the treatment of 20 μM ML-SA1. White arrow, micro-vesicles formed after the application of ML-SA1. Scale bar, 10 μm.

2. Belei OA, Heredea ER, Boeriu E, Marcovici TM, Cerbu S, Marginean O, et al. Verner-Morrison syndrome. Literature review. Rom J Morphol Embryol. 2017;58(2):371-6.
3. Giusti F, Marini F, Brandi ML. Multiple Endocrine Neoplasia Type 1. In: Adam MP, Ardinger HH, Pagon RA, Wallace SE, Bean LJH, Stephens K, et al., editors. GeneReviews((R)). Seattle (WA)1993.
4. Lechner K, Fodinger M, Grisold W, Puspok A, Sillaber C. [Vitamin B12 deficiency. New data on an old theme]. Wien Klin Wochenschr. 2005;117(17):579-91.
5. Sahoo N, Gu M, Zhang X, Raval N, Yang J, Bekier M, et al. Gastric acid secretion from parietal cells is mediated by a Ca(2+) efflux channel in the tubulovesicle. Dev Cell. 2017;41(3):262-73 e6.
6. Di Paola S, Scotto-Rosato A, Medina DL. TRPML1: The Ca((2+))retaker of the lysosome. Cell Calcium. 2018;69:112-21.
7. LaPlante JM, Falardeau J, Sun M, Kanazirska M, Brown EM, Slaugenhaupt SA, et al. Identification and characterization of the single channel function of human mucolipin-1 implicated in mucolipidosis type IV, a disorder affecting the lysosomal pathway. FEBS Lett. 2002;532(1-2):183-7.
8. Dong XP, Cheng X, Mills E, Delling M, Wang F, Kurz T, et al. The type IV mucolipidosis-associated protein TRPML1 is an endolysosomal iron release channel. Nature. 2008;455(7215):992-6.
9. Xu H, Delling M, Li L, Dong X, Clapham DE. Activating mutation in a mucolipin transient receptor potential channel leads to melanocyte loss in varitint-waddler mice. Proc Natl Acad Sci USA. 2007;104(46):18321-6.
10. Medina DL, Fraldi A, Bouche V, Annunziata F, Mansueto G, Spampanato C, et al. Transcriptional activation of lysosomal exocytosis promotes cellular clearance. Dev Cell. 2011;21(3):421-30.
11. Li X, Rydzewski N, Hider A, Zhang X, Yang J, Wang W, et al. A molecular mechanism to regulate lysosome motility for lysosome positioning and tubulation. Nat Cell Biol. 2016;18(4):404-17.
12. Clark R, Griffiths GM. Lytic granules, secretory lysosomes and disease. Curr Opin Immunol. 2003;15(5):516-21.
13. Shen D, Wang X, Li X, Zhang X, Yao Z, Dibble S, et al. Lipid storage disorders block lysosomal trafficking by inhibiting a TRP channel and lysosomal calcium release. Nat Commun. 2012;3:731.
14. Wu LG, Hamid E, Shin W, Chiang HC. Exocytosis and endocytosis: modes, functions, and coupling mechanisms. Annu Rev Physiol. 2014;76:301-31.
15. Gomez NM, Lu W, Lim JC, Kiselyov K, Campagno KE, Grishchuk Y, et al. Robust lysosomal calcium signaling through channel TRPML1 is impaired by lysosomal lipid accumulation. FASEB J. 2018;32(2):782-94.
16. Grimm C, Bartel K, Vollmar AM, Biel M. Endolysosomal cation channels and cancer-a link with great potential. Pharmaceuticals. 2018;11(1).
17. Jung J, Cho KJ, Naji AK, Clemons KN, Wong CO, Villanueva M, et al. HRAS-driven cancer cells are vulnerable to TRPML1 inhibition. EMBO Rep. 2019;20(4).
18. Xu M, Almasi S, Yang Y, Yan C, Sterea AM, Rizvi Syeda AK, et al. The lysosomal TRPML1 channel regulates triple negative breast cancer development by promoting mTORC1 and purinergic signaling pathways. Cell Calcium. 2019;79:80-8.
19. Capurro MI, Greenfield LK, Prashar A, Xia S, Abdullah M, Wong H, et al. VacA generates a protective intracellular reservoir for *Helicobacter pylori* that is eliminated by activation of the lysosomal calcium channel TRPML1. Nat Microbiol. 2019;4(8):1411-23.